UNIVERSIDAD MICHOACANA DE
SAN NICOLÁS DE HIDALGO

"MODELING OF WIND GENERATORS FOR POWER FLOWS AND DYNAMIC SIMULATIONS"

by

LUIS MIGUEL CASTRO GONZÁLEZ

THESIS

REQUIREMENT FOR THE DEGREE OF

DOCTOR OF SCIENCE IN ELECTRICAL ENGINEERING

División de Estudios de Posgrado
Facultad de Ingeniería Eléctrica

ADVISOR:
CLAUDIO RUBÉN FUERTE ESQUIVEL, PhD.

CO-ADVISOR:
ENRIQUE ACHA, PhD.

MORELIA, MICHOACÁN DICIEMBRE 2013

MODELING OF WIND GENERATORS FOR POWER FLOWS AND DYNAMIC SIMULATIONS

Los Miembros del Jurado de Examen de Grado aprueban
la **Tesis de Doctorado en Ciencias en Ingeniería Eléctrica Opción en Sistemas Eléctricos**
de ***Luis Miguel Castro González***

Dra. Elisa Espinosa Juárez
Presidenta del Jurado

Dr. Claudio Rubén Fuerte Esquivel
Director de Tesis

Dr. Enrique Acha Daza
Co- Director de Tesis

Dr. Norberto García Barriga
Vocal

Dr. Ricardo Mota Palominos
Revisor Externo

Dr. J. Aurelio Medina Rios
Jefe de la División de Estudios de Posgrado
de la Facultad de Ingeniería Eléctrica. UMSNH
(Por reconocimiento de firmas)

UNIVERSIDAD MICHOACANA DE SAN NICOLÁS DE HIDALGO
Diciembre 2013

Abstract

The research reported in this thesis develops in the realm of wind power generation, addressing the timely research question of the impact that the installation of wind parks will bring upon the electrical power grid. This is of paramount importance because worldwide installed wind capacity has surpassed this year the 280 Giga-watt mark, out of which, China, USA and Germany together have more than 160 GW; it is quite clear that the global wind generation growth rate will continue to rise in the coming years.

It is against this background of rapid growth of wind farm installations that the quest for developing versatile and efficient models of wind generators has been carried out. The two most popular types of generators have received research attention, namely, the fixed-speed and variable-speed wind generators. Their main operational characteristics have been captured in positive-sequence mathematical models, leading to comprehensive and reliable software tools for fundamental-frequency simulations. The electrical power grid is likely to experience frequency imbalances. Hence, the newly developed steady-state wind generator models are upgraded to include such an effect, with the improved models being capable of responding properly to the off-nominal frequency equilibrium point of the electrical network in the presence of power imbalances.

Today's wind parks employ the so-called doubly-fed induction generator (DFIG) technology owing to its higher energy throughputs and degree of controllability. A comprehensive model of DFIG is reported in this thesis for both steady-state and dynamic operating regimes. The associated back-to-back HVDC link using voltage source converters (VSC) is modeled by using a suitable assembly of electric circuit elements which encapsulates with a high degree of fidelity the steady-state and dynamics of the VSCs. The amplitude modulation ratio, as well as the switching and conduction losses, is included in the new VSC model. The VSC-HVDC model links on well with the variables of the stator and rotor terminals of the induction generator, thus incorporating all the key features of the DFIG-based wind turbine.

The resulting non-linear equations of the various wind generator models developed as part of this research are assembled together with the network's equations in a unified frame-of-reference for efficient solutions using the Newton-Raphson algorithm. They have been put through their paces with a number of standard test power systems of varying sizes where their modeling flexibility and numerical prowess has been shown.

Resumen

La investigación que se presenta en esta tesis se desarrolla en el ámbito de la generación de energía eólica, frente a la pregunta oportuna de los efectos que la instalación de parques eólicos traerá sobre la red eléctrica. Esto es de suma importancia, ya que la capacidad eólica instalada en todo el mundo ha superado este año la marca de los 280 GW, de los cuales, China, EE.UU. y Alemania juntos cuentan con más de 160 GW; es bastante claro que la tasa de crecimiento global de generación eólica continuará aumentando en los próximos años.

Es en este contexto de rápido crecimiento de las instalaciones de parques eólicos en que la investigación para desarrollar modelos de generadores eólicos versátiles y eficientes se ha llevado a cabo. Los dos tipos más populares de generadores han sido investigados, es decir, los aerogeneradores de velocidad fija y de velocidad variable. Sus principales características de funcionamiento han sido capturadas en los modelos matemáticos de secuencia positiva, dando lugar a herramientas de software fiables y completas para simulaciones a la frecuencia fundamental. La red de energía eléctrica es propensa a experimentar desviaciones de frecuencia. Por lo tanto, los modelos recientemente desarrollados de aerogeneradores para análisis de estado estacionario son mejorados para incluir tal efecto, siendo capaces de responder adecuadamente al punto de equilibrio fuera de la frecuencia nominal de la red eléctrica en presencia de desbalances de potencia.

Muchos parques eólicos actuales emplean generadores de inducción doblemente alimentado (GIDA), debido a sus altos rendimientos energéticos y grado de controlabilidad. Un modelo integral de GIDA se reporta en esta tesis para los regímenes de estado estacionario y dinámico. El enlace de alto voltaje en corriente directa (AVCD) que hace uso de convertidores de fuente de tensión (CFT) se modela utilizando un ensamble adecuado de elementos de circuitos eléctricos que encapsulan con un alto grado de fidelidad el estado estacionario y la dinámica de los CFTs. La amplitud del índice de modulación, así como las pérdidas de potencia por conmutación y conducción están incluidas en el nuevo modelo de CFT. El modelo CFT-AVCD se acopla apropiadamente con el estator y el rotor del GIDA, incorporando así todas las características principales de la turbina eólica.

Las ecuaciones no lineales que resultan de los diversos modelos de aerogeneradores, desarrollados como parte de esta investigación, se acoplan con las ecuaciones de la red en un marco de referencia unificado para obtener soluciones eficientes utilizando el algoritmo de Newton-Raphson. Ellos han sido puestos a prueba con una serie de sistemas de prueba de diferente tamaño, donde se ha demostrado su valor numérico y flexibilidad en el modelado.

Acknowledgements

Completion of this doctoral thesis was possible with the direct or indirect help and support of several people. I would like to express my sincere gratitude to all of them.

First of all, I am deeply grateful to my research advisor, PhD. Claudio Rubén Fuerte Esquivel for giving me the opportunity and confidence to work with him throughout this research. It's been four years of continuous learning and professional growth under his supervision. I thank him for encouraging me to improve every day and become a better professional. Equally thankful I am to my co-advisor, PhD. Enrique Acha for his valuable guidance and consistent encouragement I received during the course of the research work. I thank him for having facilitated my research internship in Finland. His unconditional support and research expertise has undoubtedly nurtured my professional career. I thank to my two advisors for giving me their friendship and I hope to keep learning from them.

I thank the faculty and teaching staff of the UMSNH who took part in the completion of my doctoral studies. Likewise, I express my gratitude to TUT for accepting me in my research internship which played a crucial role during this research work.

The National Council for Science and Technology (CONACYT) also deserves my recognition and acknowledgement for the financial support I received which facilitated the accomplishment of my doctoral degree.

I thank all my colleagues and friends from the UMSNH in Morelia and TUT in Tampere for their all-important encouraging words and friendship.

Last but not least, I express my most profound gratitude to my parents, Luis and Guadalupe, and my siblings, Lupita, Victor, Leonardo and Cesar for always being by my side when I’ve needed them the most.

Contents

List of tables

List of figures

List of publications

The research work contained in this thesis has given rise to the following refereed publications:

Journal papers:

1. **Luis M. Castro**, C. R. Fuerte-Esquivel, J. H. Tovar-Hernández, "A Unified Approach for the Solution of Power Flows in Electric Power Systems Including Wind Farms", *Electric Power Systems Research*, Vol. 81, No.10, pp. 1859-1865, October 2011.
2. **Luis M. Castro**, C. R. Fuerte-Esquivel, J. H. Tovar-Hernández, "Solution of Power Flow with Automatic Load-Frequency Control Devices Including Wind Farms", *IEEE Transactions on Power Systems*, Vol. 27, No. 4, pp. 2186-2195, November 2012.
3. **Luis M. Castro**, Enrique Acha, C. R. Fuerte-Esquivel, "A Novel STATCOM Model for Dynamic Power System Simulations", *IEEE Transactions on Power Systems*, Vol. 28, No. 3, pp. 3145-3154, August 2013.
4. Enrique Acha, Behzad Kazemtabrizi, **Luis M. Castro**, "A New VSC-HVDC Model for Power Flows Using the Newton-Raphson Method", *IEEE Transactions on Power Systems*, Vol. 28, No. 3, pp. 2602-2612, August 2013.

Conference papers:

1. **Luis M. Castro**, C. R. Fuerte-Esquivel, J. H. Tovar-Hernández, "Assessing the Steady-State Post-Disturbance Condition of Power systems Including Fixed-speed and Doubly-fed induction generators", *43rd North American Power System Symposium NAPS 2011*, pp. 1-7, Boston, MA, August 2011.
2. **Luis M. Castro**, C. R. Fuerte-Esquivel, E. Barrios, C. Angeles-Camacho, "An integrated power flow solution of Flexible AC Transmission systems containing wind energy conversion system", *IET Conference on Renewable Power Generation RPG 2011*, pp. 1-6, Edinburgh, Scotland, September 2011.

Chapters in books:

1. Esther Barrios, **Luis M. Castro**, Claudio Rubén Fuerte-Esquivel, César Angeles-Camacho, "An integrated power flow solution of flexible AC Transmission systems containing wind energy conversion system", in: *Modeling and control Aspects of wind Power Systems*, Intech, ISBN: 978-953-51-1042-2, pp. 117-132, March 2011.

Contributions to research

This thesis contributes to the area of wind power in electrical power systems. Specifically, it advances current thinking in the field of grid-connected wind generators' modeling and simulation. The main contributions to research are summarized as follows:

- This thesis presents a unified method of solution using the Newton-Raphson algorithm to determine the positive-sequence, steady-state equilibrium point for electrical power systems containing wind farms. To this end, mathematical models of fixed-speed, semi-variable-speed and variable-speed wind generators are developed taking due account of key design and operating features.
- The development of several wind generator models which are capable of responding to systems' frequency deviations is another important contribution of this research work. The formulation of the fix-speed wind generators is based on the equivalent circuit of the induction machine, thus facilitating inclusion of their system's frequency deviation-dependency. These developments also include the variable-speed wind generator models with frequency support capabilities. These models are formulated to fit a unified frame-of-reference for comprehensive iterative solutions, facilitating the estimation of the wind generators' responses following the action of the network's primary frequency regulation.
- An advanced fundamental-frequency, positive-sequence representation of power converters, of the Voltage Source Converter (VSC) type, are further developed in this thesis. The VSC is modeled using a new representation which encapsulates features such as the amplitude modulation ratio, switching and conduction losses, reactive power production and the explicit representation of its DC bus.
- In connection with the above contribution, a comprehensive model of the DFIG is developed. Its main advantages rely on the representation of the back-to-back connection of two VSC models. It enables the explicit representation of the DC bus and explicit voltage and current ports on both sides of the VSC-HVDC-link for direct connection with the stator and rotor terminals of the wound rotor induction machine, resulting in a brand new model of the DFIG with unrivalled modelling flexibility for the purpose of fundamental-frequency, positive-sequence simulation steadies. Bothe the steady-state and dynamic operating regimes received attention.

Nomenclature

θ:	Voltage angle
V:	Voltage magnitude
P_g:	Generated active power
Q_g:	Generated reactive power
P_d:	Active power drawn by the load
Q_d:	Reactive power drawn by the load
P_k^{cal}:	Active power injection at bus k
Q_k^{cal}:	Reactive power injection at bus k
P_m:	Mechanical power of the turbine
P_{nom}:	Nominal power of the wind turbine
P_{conv}:	Power converted from mechanical to electrical form
ρ:	air density
A:	Swept area of the blades
R_b:	Rotor blade radius of the turbine
V_w:	Wind speed
C_p:	Power coefficient
β:	Pitch angle
λ:	Tip speed ratio
$n_{qb:}$	Gearbox ratio
s:	Slip of the induction generator
ω_s:	Angular synchronous speed
ω_m:	Angular speed of the induction generator
ω_T:	Angular speed of the turbine
ω_b:	Base angular speed
R_1, R_2:	Stator and rotor resistance of the FSWG and SSWG
X_1, X_2, X_m:	Reactances of the FSWG and SSWG
Δf:	Frequency deviation
R:	Speed droop of the generator
η:	Level of deloading of the wind turbine
φ:	Power factor angle
v_{ds}, v_{qs}:	Stator direct and quadrature axis voltage of the DFIG
i_{ds}, i_{qs}:	Stator direct and quadrature axis current of the DFIG
v_{dr}, v_{qr}:	Rotor direct and quadrature axis voltage of the DFIG
i_{dr}, i_{qr}:	Rotor direct and quadrature axis current of the DFIG
R_s, R_r:	Stator and rotor resistance of the DFIG
L_{ss},L_{rr},L_m:	Leakage inductances of the DFIG
ψ_{ds}, ψ_{qs}:	Stator direct and quadrature axis flux linkage of the DFIG
ψ_{dr}, ψ_{qr}:	Rotor direct and quadrature axis flux linkage of the DFIG
T_e:	Electromagnetic torque
T_m:	Mechanical torque
H:	Inertia of the wind turbine
B_{eq}:	Equivalent shunt susceptance
C_{DC}:	DC capacitor
H_c:	Inertia constant of the DC capacitor
V_0:	DC bus voltage

m_a:	Modulation index
G_{sw}:	Conductance for computing the switching losses of the VSC
R_{1v}, X_{1v}:	Series resistance and reactance of the VSC
I_{nom}:	Nominal current of the VSC
S_{nom}:	Rated apparent power of the B-B converter
AC:	Alternating current
B-B:	Back-to-back converter
DAE:	Differential algebraic equations
DC:	Direct current
DFIG:	Doubly-fed induction generators
FP-FSWG:	Fixed-pitch fixed-speed wind generator
FSWG:	Fixed-speed wind generator
GSC:	Grid side converter
J:	Jacobian matrix
HVDC:	High voltage direct current
MPT:	Maximum power tracking
NR:	Newton Raphson
PFALFC:	Power flow with automatic load/frequency control
PMSG:	Permanent magnet synchronous generator
PR-FSWG:	Pitch-regulated fixed-speed wind generator
PWM:	Pulse-width modulation
RSC:	Rotor side converter
SCIG:	Squirrel-cage induction generator
SSWG:	Semi-variable speed wind generator
VSC:	Voltage source converter
VSWG:	Variable-speed wind generator
WECS:	Wind energy conversion system
WRIG:	Wound-rotor induction generator
WRSG:	Wound-rotor synchronous generator

Chapter 1

INTRODUCTION

1.1 Motivation and justification

The generation of electrical power using the wind as primary energy resource is a well-established production mechanism in the modern electricity supply industry worldwide. Its rate of growth is impressive, outperforming all other forms of renewable generation. This is even more so considering that it is less than two decades from the time when real resources were dedicated to develop the wind generation technology at industry-scale. Research on the various aspects of wind power generation have been taking place for much longer, with the early drive being on autonomous wind generators or wind farms as opposed to present-day grid-connected wind parks. These are rated at the multi-Mega-watt level, with some of them having been erected on-shore and some others off-shore. Through targeted research, the wind power technology has evolved in all fronts, resulting in larger and more efficient wind turbines and with a vastly improved operational performance. Today's wind parks using the latest wind turbines technology, may rival some of the conventional power generating stations in terms size, operational flexibility, efficiency, installation costs and operational costs. However, it is important to bear in mind that the stochastic behavior of the wind resource makes for a more difficult operation of wind parks compared to the operation of conventional power generating stations which have a rather stable fuel supply, or water supply in the case of a hydro-electric station. To keep par with the many breakthroughs in the wind power equipment manufacturing industry, power systems engineers ought to take on the task of providing suitable models of the new equipment and application software tool with which to assess whether or not the new types of generators can be integrated into the power networks, optimal locations and the required power grid reinforcements. With the passage of time, new kinds of wind generators are appearing in the market, with more power electronics than ever before, new control functionality, new types of rotating machines, lack of gearboxes, etc. This has provided the motivation for electrical engineers to develop mathematical representations of the new equipment and the electrical power networks to

which they are connected to. To ensure meaningful results, of real applicability, the elaboration of mathematical models, of grid-connected wind power generators call for software implementations and the comprehensive verification of results. Owing to the complexity of the task in hand, this is only possible through a comprehensive and sustained programme of research spanning several years.

In this context, a suitably upgraded power flow algorithm may become a useful tool for the planning and operation of power networks with embedded wind generators. Furthermore, power flow solutions are required to gather good initial conditions for dynamic simulation studies. From the outset of this research the effort is directed towards addressing the steady-state, fundamental frequency, positive-sequence modeling and analysis of the various kinds of wind power generators. This is followed by a reformulation of these steady-state models to enable their incorporation into a power flow formulation which is able to estimate system frequency variations. The DFIG wind technology has become the preferred option in modern wind parks owing to their far superior performance in terms of wind energy capture and smoother interaction with the operation of the electrical power grid. In spite of this, the modeling of DFIG equipment remains substantially under-developed for both steady-state and dynamic regimes. To remedy this situation, the DFIG receives research attention in this thesis, resulting in a new model for the back-to-back converters where the DC bus is explicitly represented and so are the converters switching and conduction losses. Moreover, the output variables at the AC sides of both converters fit on well with the variables of the stator and rotor of the wound induction machine. This makes up for a comprehensive and versatile model of the DFIG for the purpose of fundamental frequency, positive-sequence steady-state and dynamic solutions. The ensuing mathematical equations are non-linear and their solution is carried out by iteration. Reliability towards the convergence is of utmost concern and proven numerical methods should be employed to solve the associated non-linear equations. The Newton-Raphson (NR) method has shown to be the most successful iterative method for solving practical power networks. Hence, in this research, this approach has been adopted for solving the newly developed wind generator models together with the rest of the network equations for unified and efficient iterative solutions.

It should be stressed that in spite of the wind power area being one of the fastest moving fields in terms of the design of wind generator topologies and their controls, semiconductor valves for the power electronic converters and applications; paradoxically, there has been limited progress in terms of developing realistic and efficient models with

which to assess their impact on large-scale power grids. It should also be emphasized that there is a growing need for power system operators to be able to anticipate well in advance, all potential difficulties that may arise in the operation of the system caused by the rather large amounts of wind power penetration. For these models to be truly useful to the electrical power industry, they need to be embedded into software in order to enable the reliable solution of practical power networks in short periods of time, lasting no more than a few seconds of computer time. More often than not these studies would comprise numerous individual solutions to assess *what if* scenarios.

1.2 State of the art

The use of wind energy conversion systems (WECS) has established itself as the most rapidly growing renewable energy source for the purpose of electricity generation globally, such that the power generated by wind turbines accounts for a considerable percentage of the total power production in a number of European countries, China and USA [WWEC, 2013], [EWEA, 2013]. By the end of 2013, the global installed wind farm capacity has surpassed the 300 GW mark, out of which more than 44 GW were added in 2012. The growing trend is irreversible and a global capacity of more than 500 GW is expected to be reached by the year 2016 [WWEC, 2013]. In Mexico, a total wind capacity of 598 MW is currently installed, representing just over 1% of the total generation capacity [SENER, 2013]. Recent studies indicate, however, that Mexico's wind energy potential could reach more than 12 GW [SENER, 2012] within the next 8 years. In contrast, the Chinese Government, the largest owner of wind farms in the world has got at present, a total capacity of 80 GW.

The overwhelming majority of public opinion agrees that wind energy is an environment-friendly way of generating electricity; however, it does make the already complex task of achieving system controllability even more demanding. Consequently, the quantification of the effects that large-scale integration of wind generation will have on the power network is a matter of great importance that requires a great deal of attention when planning and operating the wind generation-upgraded electrical power system. Arguably, power flow analysis is the most frequently performed computational calculation in a power system's planning and operation, and this study has been selected as a starting point to quantify the electrical response of wind generators. To begin with, the conventional power flow method is used in this thesis in order to gain insight into the steady-state performance of power networks containing wind generators. On the other hand, since it is of interest for

power system operators to estimate by how much the reliability of an electric power system can be degraded by power imbalances between load and generation, which are inherent to its daily operation; developing suitable wind generator models within the context of power flows with automatic load frequency devices (PFALFC) is a basic necessity in this new environment. These models ought to be created in such a manner that they are consistent with the models available for conventional power flows and that have served the power systems community very well for more than half a century. The ensuing models incorporate a far greater level of detail than the conventional power flow models, particularly the phenomena associated with the all-important frequency deviations in the power network – an issue that is all but missed in the conventional application tool.

Furthermore, the power supply industry may be casting aside several of the challenges arising from the incorporation of large blocks of wind power into their power grids. A case in point is the need for maintaining system integrity in the face of a wind resource that is stochastic in nature - and so is wind power generation. It is not difficult to surmise that the power grid will be subjected to even more little, perpetual impulses than ever before. Hence, new dynamic models of wind power generators would need to be developed with which to carry out time-domain simulations so as to furnish wider information in electrical power systems with a substantial amount of wind power penetration. It is recommended in this space that power systems planners and operators have at their disposal comprehensive models of wind generators for assessing the performance of power networks containing WECS, within a variety of contexts. Cases in point are models suitable for computing the steady-state operation using conventional power flows, steady-state operation taking into account frequency variations in the power grid and dynamic models of wind generators using time-domain simulations. In the fullness of time other application tools may deem to be essential too, such as optimal power flows and state estimation, three-phase power flows, small-signal stability. However, in connection with this thesis, the aforementioned tools may be seen to be the essential ones.

Research in this area of electrical power systems is not new by any means. The earlier publications may be traced back to around the year 2000, where some contrived mathematical models may be found. For instance, models of wind generators were developed in the form of active and reactive power outputs derived from the steady-state equivalent circuit of the induction machine [Feijóo and Cidrás, 2000], [Divya and Rao, 2006], [Liu et al., 2008], [Feijóo, 2009]. In these papers, the power injections method is used to include the induction generators contribution into the power flow formulation, using a sequential approach to obtain an operating point of the

power system. It should be noticed that in these solution approaches, the network's state variables are calculated using a conventional power flow algorithm and that a sub-problem is formulated for updating the state variables of the wind generators together with their power injections at the end of each power flow iteration. Such a solution approach may be referred to as a sequential approach. It should be brought to attention that the sequential approach is the preferred option by some researches owing to its ease of implementation in existing AC power flow computer programs. However, the unified solutions provide more robust solutions towards the convergence. Admittedly, one iteration of the unified solution may take longer than one iteration of the sequential solution.

Some differences exist in the solution approach put forward in these publications but all of them refer to the modeling of fixed-speed wind generators using nodal power injections. In [Feijóo and Cidrás, 2000], the active power is obtained from the power curve and the reactive power output is estimated by using an approximated quadratic function dependent on the active power and the voltage magnitude measured at the wind generator's terminals. This model is referred to as the *PQ* model. On the other hand, the active and reactive power outputs of the models proposed in [Divya and Rao, 2006] and [Liu et al., 2008] are expressed in terms of the generators' variables and parameters using no approximations.

An alternative modeling approach for fixed-speed wind generator is to determine an equivalent variable impedance expressed in terms of the slip of the generator and its rotor and stator winding parameters [Feijóo and Cidrás, 2000], [Feijóo, 2009]. This impedance is included in the system's admittance matrix, and the network nodal voltages are computed through the power flow analysis. Based on these voltages, the air-gap power of the wind generator is calculated, and the value of the slip of the induction generator is then computed iteratively to match the air-gap power and mechanical power extracted from the wind. Following the same idea, the iterative process to compute the slip may be avoided by assuming that the mechanical power is known [Feijóo, 2009].

The power flow analysis of variable-speed wind turbines using doubly-fed induction generators has also been an object of study. A doubly-fed induction generator (DFIG) model for power flow studies is available in [Divya and Rao, 2006], where the total rotor current magnitude is checked at each iteration. If a limit violation in current is detected then the wind generator model gives priority to the reactive over the active power generation in order to support the bus voltage magnitude at the connecting node. From the power flow point of

view, this model is treated as a *PQ* bus with a fixed unity power factor, i.e. the active power output is obtained from the wind generator power curve, and the reactive power is set to zero.

In general terms, all the methods outlined above share the characteristic of using a sequential approach to calculate the state variables of the wind generators. This sequential iterative approach is rather attractive because it is straightforward to implement into existing power flow programs; however, caution has to be exercised because it will yield no quadratic convergence [Fuerte-Esquivel et al., 1997], [Smed et al., 1991], and an additional set of nonlinear algebraic equations have to be solved to obtain the values of the wind generator's state variables.

A fundamentally different approach for the modeling of WECS, within the framework of the power flow problem, is a method that simultaneously combines the state variables corresponding to the wind generators and the network in a single frame of reference for a unified iterative solution through a Newton-Raphson (NR) technique where its convergence characteristics are explained in Appendix A. From the reliability towards the iterative solution standpoint, i.e., the number of iterations required to obtain the power flow solution, this method is superior to the sequential one because all state variables are simultaneously adjusted during the iterative process. Furthermore, it arrives at the solution with local quadratic convergence regardless of network size if proper initial conditions are selected and the Jacobian matrix does not become singular at any stage of the solution process [Ortega and Rheinboldt, 2000], [Traub, 1964]. In this work reliable and comprehensive modeling approaches are put forward for the analysis of both conventional power flows and PFALFC in electric power systems containing WECS, using in a unified single frame of reference, as suggested in [Fuerte-Esquivel et al., 2001].

The original PFALFC algorithm was developed in the mid-1970s [Okamura et al., 1975]. In this approach, in addition to the state variables used in the conventional power flow formulation, the system's frequency deviation also becomes a state variable and solved simultaneously with all the other state variables of the power system. Furthermore, the voltage and frequency dependency of loads can be taken into account to represent their variation according to the various operating conditions. This methodology is quite attractive because it permits to estimate the steady-state operating point following the action of the primary frequency regulation of synchronous generators. In this sense, the mathematical models of the fixed-speed wind turbines developed in this thesis, which rely primarily on the power injection concept, are suitably represented with their active and reactive powers defined in terms of the induction machine's stator and rotor parameters as well as the system

frequency deviation. On the other hand, the variable-speed wind generators are built in such a way that they are able to provide primary frequency regulation by maintaining some spinning reserve via the prior de-loading of the wind turbine, as suggested in [Ramtharan et al., 2007], [Chowdhury et al., 2008], [Morren et al., 2006], [Moutis et al., 2009], [Teninge et al., 2009], [de Almeida and Peças Lopes, 2007], [de Almeida at al., 2006]. The simultaneous solution of the non-linear equations arising from any of these models along with those of the conventional power network, allows for efficient iterative solutions yielding information on system frequency deviations.

Concerning the available DFIG steady-state models, they are formulated on the assumption that they may be treated as either *PQ* or *PV* nodes. This formulation has the advantage of simplicity in terms of its implementation. However, the shortcomings of such a representation are self-evident. For one, it is not possible to estimate the internal state variables of the induction machine and the voltage source converters (VSCs) that are employed in the DFIG's back-to-back converter: the rotor-side converter (RSC) and the grid-side converter (GSC). This provides the motivation for developing more realistic and flexible models with which to assess the impact of DFIG wind power generator in large-scale power grids. Hence, the research reported in this thesis on a new generation of variable-speed wind generators bridges the gap in this all-important area of power systems. The early modeling approach where the VSC is represented as a controllable voltage source behind coupling impedance became a popular model to represent the steady-state fundamental frequency operation [Acha et al., 2005]. This simple concept explains well the operation of the converters from the standpoint of the AC network but its usefulness is very much reduced when the requirement involves the assessment of variables relating to the VSC's DC bus. This discussion may extrapolated almost with no change to the dynamic regime of the converter where the standard approach has also been the use of a controllable voltage source [Cañizares, 2000], [Barrios-Martinez et al., 2009], [Faisal et al., 2007], [Shahgholian et al., 2011], [Mahdavian et al., 2011], [Wang and Crow, 2011]. Perhaps the more advanced version of these models in the dynamic front is the one reported in [Cañizares, 2000], where the power flowing into the equivalent voltage source is used to directly control the DC voltage magnitude – to a greater or lesser extent, the DC bus of the VSC is collapsed into the ideal voltage source, including its effect but having no access to it. Following this idea, a model where the VSC is treated as a controllable reactive current source with a time delay, has been put forward in [Jabbari et al., 2011]. Nonetheless, all these models exhibit the same shortcoming, namely, the no explicit representation of its DC circuit. It has to be brought to

attention that DFIG's converter connected to the grid, termed grid-side converter (GSC), resembles very much the physical operation of a STATCOM whose main functions are: to fix the voltage at the DC side and to provide reactive power support to the grid.

Unlike the existing approach for representing the voltage source converter models comprised in the back-to-back converter (B-B) of the DFIG, this thesis advances a new model of the rotor-side converter (RSC) and the grid-side converter (GSC). They are formulated with enhanced attributes: (i) they make an explicit representation of the DC bus, which enables the inclusion of a realistic switching loss model; (ii) Segregating the overall VSC power losses into conduction and switching power losses becomes possible [Acha and Kazemtabrizi, 2013]. Hence, a new positive-sequence DFIG model for steady-state and dynamic simulations of power networks for fundamental frequency operation is reported in this work. Contrary to the current practice of DFIG modeling where controllable voltage sources are employed to represent the VSCs, the back-to-back VSC-HVDC link that forms a key part of the DFIG generator is modeled in full, resulting in a far superior model where the DC side of the back-to-back converter is explicitly available. In the new model, each VSC is represented as a complex tap-changing transformer: one where its primary and secondary sides quite naturally yield to the VSC's AC and DC sides, respectively [Acha and Kazemtabrizi, 2013]. The new VSC model combines with ease with the wound-rotor induction generator (WRIG) to constitute the new DFIG model for steady-state and dynamic simulations.

1.3 Objectives

The main objective of this research is to provide an all-encompassing mathematical modeling framework for the assessment of grid-connected wind power generators taking due account of the main design and operating characteristics of the wind power generators and the electrical power grid. The modeling framework should caters for both steady-state and dynamic operating regimes and the numerical solution of the ensuing set of nonlinear equations should be carried out using the Newton-Raphson method for efficient and reliable iterative solutions.

Three main issues on the modeling of wind generators would be addressed in this thesis in order to offer an all-encompassing modeling philosophy of grid-connected wind power generators. The first issue relates to the solution of power networks containing wind power farms in steady-state operating regimes, which may be referred to as the conventional

power flow solution. To this end, fixed-speed as well as variable-speed wind generator models have to be created and tested for performance and accuracy of responses using a number of power grids with different degree of complexity. These models should be made to follow as much as possible the response of those machines employed in real-life applications in order to ensure that the research output has a good degree of engineering realism. In the second modeling issue, the wind generator models developed for conventional power flows would have to be re-formulated in order to ensure full compatibility with the framework of power flows with automatic load frequency control devices. The third issue relates to the steady-state and dynamic modeling of grid-connected variable speed wind generator. In contrast to the current practice of DFIG modeling which has been identified as having shortcomings that may be worthwhile to remove, the development of a new breed of DFIG models will be carried out by firstly building on a new model of the STATCOM. This should result on models with enhanced features that allow the explicit representation of all the main components of the DFIG, such as: the wound-rotor induction machine, the rotor-side and grid-side converters together with their associated controls for both steady-state and dynamic operating regimes.

1.4 Methodology

The following research methodology has been adopted to comply with the objectives of the research project described in this thesis:

- To carry out a comprehensive review of the existing literature in the area of wind power generation, with particular emphasis on the mathematical representation of grid-connected wind power generators.
- To carry out the mathematical development of wind power generators using first principles and to carry out their computational implementation for assessing their performance in grid-connected simulation environments. All the developments were geared from the outset to have models suitable for unified power flow solutions using the Newton-Raphson method.
- To build the test case scenarios and to carry out comprehensive simulation studies and the associated analyses of results.
- To carry out a comprehensive literature review of wind power generator models with frequency-control device representation.

- To carry out the mathematical development and software implementation of models of wind power generators taking due account of the synchronous generators' frequency-control devices. The mathematical developments and ensuing coding were carried out for unified power flow formulations using the Newton-Raphson method.
- To build the test case scenarios and to carry out comprehensive simulation studies and the associated analyses of results.
- To carry out a comprehensive literature review of the current modeling practice in the electrical power systems area of voltage source converters, STATCOMs and VSC-HVDC; with particular emphasis in wind power applications.
- To carry out the mathematical development of the DFIG by resorting to first principles and software implementations. The ensuing model is rather comprehensive and suitable for steady-state and time-domain simulations. The uniqueness of the new DFIG model at this point in time is the use of the new back-to-back converter model, which builds into the overall DFIG model, unrivalled modeling flexibility.
- To build the test case scenarios and to carry out comprehensive simulation studies and the associated analyses of results.

1.5 Thesis outline

The remainder of this thesis is organized as follows:

Chapter 2 presents the steady-state, positive sequence models of various wind power generators. Models of fixed-speed, semi-variable speed and variable speed wind power generator, are addressed. The first two are directly derived from the steady-state representation of the equivalent circuit of the induction generator. For the case of the variable speed wind generator, this is treated as a *PV* source with reactive power support characteristics. General guidelines for their initialization of state variables are provided.

Chapter 3 addresses the representation of fixed-speed and variable-speed wind power generators with frequency dependency. In the case of variable-speed wind generators, their potential contribution to the system's frequency is analyzed. All the models are formulated within the context of the power flow formulation with automatic load frequency control devices, using a unified frame-of-reference. Suitable initialization of the state variables for reliable iterative solutions is paid attention to.

Chapter 4 presents a comprehensive mathematical model of the DFIG where the power converters are no longer modeled as controllable voltage sources but, rather, as phase-shifting transformers, enabling the explicit representation of the DC link and the calculation of switching and conduction losses. This complete model is used for computing the steady-state and the dynamic operation of DFIGs.

Chapter 5 illustrates the applicability of the newly developed models for the analysis of conventional power flows, power flows with automatic load frequency devices and time domain simulations in electric power systems containing wind power turbines. The proposed models are tested in networks of different size: an 8-bus system, the IEEE 14-bus system, the IEEE 30-bus system and the IEEE 118-bus system for the steady-state wind power generator models. The full DFIG model is tested in the 8-bus system and in the IEEE 30-bus network.

Chapter 6 gives the general conclusions of the thesis and provides suggestions for future research work.

Chapter 2

POWER FLOWS IN POWER SYSTEMS WITH WIND GENERATORS

2.1 Introduction

In this chapter, various wind generator models are developed using first principles. These are formulated in such a way that they can be used in unified solutions within power flow-like formulations, for efficient solutions. The two types of directly grid-connected wind generators, namely the fix-speed wind generator (FSWG) and the semi-variable speed wind generator (SSWG), are addressed. This is followed by the variable-speed wind generator (VSWG) of the conventional DFIG type and the PMSG type, bearing in mind that the VSWGs have reactive power support capabilities. This feature is of great importance because of its ability to comply with modern grid code requirements, such as reactive power and voltage support [Erlich and Bachmann, 2005], [Zavadil and Smith, 2005], [Fagan et al., 2005], [Christiansen and Johnsen, 2006]. A general strategy for the initialization of the state variables of wind generators is also presented.

2.2 Unified power flow formulation based on the Newton-Raphson method

The unified approach combines equations representing the active and reactive power balance at each node of the electrical network and at each wind generator into one set of nonlinear algebraic equations $f(X)$ with unknown variables given by $X = [\ X_{nAC}, X_{WG}]$, where X_{nAC} is a vector of all nodal voltage angles and magnitudes, and X_{WG} is a vector of all state variables associated with the wind generators. The NR method is then used to provide an approximate solution to this set of equations given by $f(X) = 0$, by solving for ΔX_i in the linear problem $J_i \Delta X_i = -f(X_i)$, where J is known as the Jacobian matrix given in expanded form by (2.1). The NR method starts from an initial guess for the X_0 and updates the solution at each iteration i, i.e. $X_{i+1} = X_i + \Delta X_i$, until a predefined tolerance is fulfilled. In this unified solution, the state

variables X_{WG} of the wind generators are adjusted simultaneously with the AC system state variables in order to compute the steady-state operating condition of the power system:

$$\begin{bmatrix} \Delta P \\ \Delta Q \\ \hline \Delta f(X_{WG}) \end{bmatrix}^i = -\left[\begin{array}{cc:c} \frac{\partial \Delta P}{\partial \theta} & \frac{\partial \Delta P}{\partial V} & \frac{\partial \Delta P}{\partial X_{WG}} \\ \frac{\partial \Delta Q}{\partial \theta} & \frac{\partial \Delta Q}{\partial V} & \frac{\partial \Delta Q}{\partial X_{WG}} \\ \hdashline \frac{\partial f(X_{WG})}{\partial \theta} & \frac{\partial f(X_{WG})}{\partial V} & \frac{\partial f(X_{WG})}{\partial X_{WG}} \end{array}\right]^i \begin{bmatrix} \Delta \theta \\ \Delta V \\ \hline \Delta X_{WG} \end{bmatrix}^i, \tag{2.1}$$

where ΔP and ΔQ are the active and the reactive power mismatch vectors, respectively. In addition, $\Delta\theta$, ΔV and ΔX_{WG} are the vectors of incremental changes in nodal voltage angles and magnitudes, as well as the wind generators' state variables.

2.3 Aerodynamic model of the wind turbine rotor

The conversion of the kinetic energy from the wind into mechanical power made by the wind turbine's rotor is computed by [Ackerman, 2005]

$$P_m = \frac{1}{2}\rho C_p A V_w^3 \tag{2.2}$$

where P_m is the mechanical power developed by the wind turbine, ρ is the air density [kg/m^3], A is the swept area of the blades [m^2] and V_w is the wind speed [m/s]. The aerodynamic coefficient of the rotor, C_p, represents the percentage of the kinetic energy of the air mass that is converted to mechanical power and is calculated as

$$C_p = c_1\left(\frac{c_2}{\lambda_i} - c_3\beta - c_4\beta^{c_5} - c_6\right)\cdot e^{\frac{-c_7}{\lambda_i}} \tag{2.3}$$

$$\lambda_i = \left[\left(\frac{1}{\lambda + c_8\cdot\beta}\right) - \left(\frac{c_9}{\beta^3+1}\right)\right]^{-1} \tag{2.4}$$

$$\lambda = \frac{R_b\cdot\omega_r}{V_w} = \frac{R_b\cdot n_{gb}\cdot\omega_s\cdot(1-s)}{V_w}, \tag{2.5}$$

where β is the pitch angle of the rotor blades [degrees] and λ is the tip speed ratio, n_{gb} is the gearbox ratio, ω_s is the angular synchronous speed [rad/s], s is the slip of the induction generator, ω_T is the angular speed of the turbine [rad/s], R_b is the radius of the rotor [m] and the constants c_1 to c_9 are the parameters of design of the wind turbine.

The maximum value of C_p can be found by setting $\beta = 0^o$ thus obtaining, the optimal value of the λ. Based on this, an optimal power curve may be constructed, which in turns is employed as a reference in the active power control strategy for maximizing the power extracted from the wind.

When wind speeds are high, the aerodynamic torque increases and the forces on the blades may provoke failure not only on the blades, but also on the drive train of the turbine. To prevent this, wind turbines are fitted with passive and active preventive control measures, namely, stall control and pitch control. The former strategy uses a fix pitch and it is commonly referred to as stall-regulated wind turbines in the wind power industry. They are designed in such a way that in high wind speeds their blades stall [Muljadi et al., 1998]. On the other hand, the active control system commonly referred to as blade pitch angle mechanism, smoothly pitches the blades for high wind speeds: it turns the turbine's blades on its own axis, resulting in a reduced aerodynamic torque, thus decreasing power production; not only does the pitching of the blades help to reduce the speed/torque in the drive train but it also permits to keep the power constant above the rated wind speeds. Figure 2.1 helps to illustrate these control strategies. Notice that both the fixed-pitch and the pitch-regulated wind turbines are shut down when the wind speed reaches the so-called cut-out wind speed.

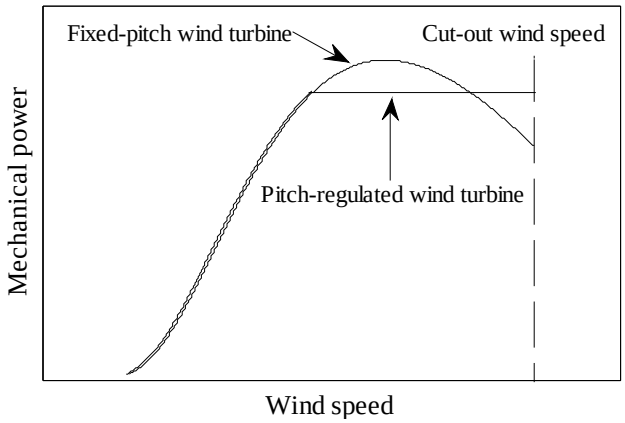

Figure 2.1: Power reduction control strategies for fixed-pitch and pitch-regulated wind turbines.

2.4 Modeling of fixed-speed wind generators (FSWGs)

The concept of this machine is based on a squirrel-cage induction generator (SCIG), which is driven by a wind turbine with its stator directly connected to the grid through a coupling power transformer as shown in Figure 2.2(a). Since the speed is almost fixed to the grid frequency and is not controllable, this asynchronous machine is considered a FSWG. The mathematical model suitable for power flow analysis is derived from the steady-state equivalent model of the induction machine shown in Figure 2.2(b), where the subscripts 1 and 2 represent stator and rotor variables, respectively, *m* symbolizes the magnetization branch, *R* is resistance and *X* represents a reactance, *I* is electric current, *s* is the slip of the induction generator, *V* is the terminal voltage, and P_g and Q_g are the active and reactive powers generated by the induction machine, respectively.

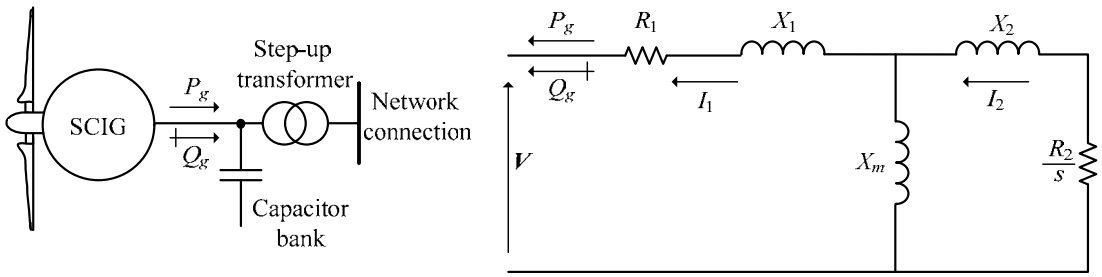

Figure 2.2: (a) Schematic representation of a FSWG, and (b) steady-state equivalent circuit model of the asynchronous generator.

When the generator mode is adopted, the power converted from mechanical to electrical form, P_{conv}, can be computed as follows [Fitzgerald et al., 2003]:

$$P_{conv} = -I_2^2 R_2 \left(\frac{1-s}{s} \right). \tag{2.6}$$

Because P_{conv} depends on the induction generator's slip, the active power, P_g, the reactive power, Q_g, the squared stator current, I_1^2, and the squared rotor current, I_2^2, are likewise affected by the machine's slip. Note that the aforementioned currents and powers are also directly affected by the generator terminal voltage, *V*. They can be determined by (2.7)-(2.10), which are derived after algebraic manipulation (as in Appendix B):

$$Q_g(V,s) = -V^2 \left\{ \frac{A + B\,s^2}{\left[C - D\,s\right]^2 + \left[E + F\,s\right]^2} \right\} \tag{2.7}$$

$$P_g(V,s) = -V^2 \left\{ \frac{K + H\,s + L\,s^2}{\left[C - D\,s\right]^2 + \left[E + F\,s\right]^2} \right\} \tag{2.8}$$

$$I_1^2(V,s) = V^2 \left\{ \frac{\left[K + H\,s + L\,s^2\right]^2 + \left[A + B\,s^2\right]^2}{\left(\left[C - D\,s\right]^2 + \left[E + F\,s\right]^2\right)^2} \right\} \tag{2.9}$$

$$I_2^2(V,s) = V^2 \left\{ \frac{\left[M\,s + N\,s^2\right]^2 + \left[T\,s - W\,s^2\right]^2}{\left(\left[C - D\,s\right]^2 + \left[E + F\,s\right]^2\right)^2} \right\} \tag{2.10}$$

where the constants *A* to *W* are associated to the generator's resistances and reactances.

In general, the above equations apply for any wind generator that is directly connected to the grid. Some types of wind turbines are equipped with control systems aimed at limiting the power captured from the wind in order to protect the mechanical drivetrain system; therefore, depending on the auxiliary systems of each wind generator, a different power flow formulation must be employed. The following section addresses the modeling of the fixed-pitch and pitch-regulated speed wind generator models.

2.4.1 Fixed-pitch fixed-speed wind generators (FP-FSWGs)

The FP-FSWG possesses the most basic mechanical construction among all the wind generators. Its generator is directly connected to the grid with no control systems, and the turbine's rotor blades are bolted onto the hubs at a fixed attack angle. The mechanical power, P_m, developed by its turbine is estimated by (2.2)-(2.5). When the FP-FSWG is connected at terminal *k* of the system, the set of mismatch power flow equations is

$$\Delta P_k = P_g(V,s) - P_{dk} - P_k^{cal} = 0 \tag{2.11}$$

$$\Delta Q_k = Q_g(V,s) - Q_{dk} - Q_k^{cal} = 0 \tag{2.12}$$

$$\Delta P_{WT1,k} = -\left(P_m - P_{conv}\right) = -\left[P_m + I_2^2 R_2 \left(\frac{1-s}{s}\right)\right] = 0\,, \tag{2.13}$$

where Q_g and P_g are given by (2.7) and (2.8), respectively, P_{dk} and Q_{dk} represent the active and reactive powers drawn by the load at bus k, respectively, and P_k^{cal} and Q_k^{cal} are active and reactive power injections given by

$$P_k^{cal} = V_k^2 G_{kk} + V_k \sum_{m \in k} V_m \left[G_{km} \cos\left(\theta_k - \theta_m\right) + B_{km} \sin\left(\theta_k - \theta_m\right) \right] \tag{2.14}$$

$$Q_k^{cal} = -V_k^2 B_{kk} + V_k \sum_{m \in k} V_m \left[G_{km} \sin\left(\theta_k - \theta_m\right) - B_{km} \cos\left(\theta_k - \theta_m\right) \right]. \tag{2.15}$$

Once equations (2.11)-(2.13) have been defined, the set of linearized power mismatch equations given by (2.16) must be assembled and combined with the Jacobian matrix J, the power mismatch vector $f(X)$ and the vector of incremental changes in state variables ΔX of the entire network for a unified solution of the voltage magnitudes V and angles θ associated with the network and the wind generator's slip:

$$\begin{bmatrix} \Delta P_k \\ \Delta Q_k \\ \Delta P_{WT1,k} \end{bmatrix}^i = \begin{bmatrix} \dfrac{\partial P_k^{cal}}{\partial \theta_k} & \left(\dfrac{\partial P_k^{cal}}{\partial V_k} - \dfrac{\partial P_g}{\partial V_k} \right) V_k & \dfrac{\partial P_g}{\partial s} \\ \dfrac{\partial Q_k^{cal}}{\partial \theta_k} & \left(\dfrac{\partial Q_k^{cal}}{\partial V_k} - \dfrac{\partial Q_g}{\partial V_k} \right) V_k & \dfrac{\partial Q_g}{\partial s} \\ 0 & \dfrac{\partial P_{WT1,k}}{\partial V_k} V_k & \dfrac{\partial P_{WT1,k}}{\partial s} \end{bmatrix}^i \begin{bmatrix} \Delta \theta_k \\ \dfrac{\Delta V_k}{V_k} \\ \Delta s \end{bmatrix}^i \tag{2.16}$$

After each iteration the state variable s is updated according to $s^{i+1} = s^i + \Delta s^i$.

2.4.2 Pitch-regulated fixed-speed wind generators (PR-FSWGs)

A pitch-regulated FSWG is usually operated at a fixed pitch below the rated wind speed of the turbine. In cases where the wind speed is above its rated value, the power extracted from the wind is limited by adjusting the pitch angle mechanism, and a rated power output is achieved for any given wind speed [Bianchi et al., 2006]. In other words, this wind generator has a certain capacity of active power control as opposed to a FP-FSWG; therefore, the generated active power $P_{g,pr}$, which can be obtained for any given wind speed from the wind generator power curve provided by the manufacturer, is constant through the iterative process: $P_{g,pr} = P_{g,pr}^{sp}$. On the other hand, the reactive power $Q_{g,pr} = Q_g$ needs to be calculated as in the case of the FP-FSWG: the reactive power equation (2.7) needs to be included and

solved within the iterative solution.

By neglecting the core losses in the induction machine, the mechanical power for a PR-FSWG is

$$P_{m,pr} = P_{g,pr}^{sp} + P_{losses,s} + P_{losses,r} = P_{g,pr}^{sp} + 3I_1^2 R_1 + 3I_2^2 R_2 \ , \tag{2.17}$$

where $P_{losses,s}$ and $P_{losses,r}$ are the three-phase stator and rotor power losses, respectively.

Substituting the expressions for the stator and rotor currents of a FSWG, (2.9) and (2.10) respectively, in (2.17) and assuming that the PR-FSWG is connected at node *k*, the values of the state variables that satisfy the mismatch equations (2.18)-(2.20) are obtained by superimposing the set of linear equations (2.21) to the entire set of the network's linearized equations and solving the resulting set of equations iteratively. In this case, equation (2.20) represents the power balance inside the induction machine

$$\Delta P_k = P_{g,pr}^{sp} - P_{dk} - P_k^{cal} = 0 \tag{2.18}$$

$$\Delta Q_k = Q_g\left(V, s\right) - Q_{dk} - Q_k^{cal} = 0 \tag{2.19}$$

$$\Delta P_{WT2,k} = -P_{g,pr}^{sp} - \left[\left(3I_1^2 R_1 + 3I_2^2 R_2\right) + I_2^2 R_2\left(\frac{1-s}{s}\right)\right] = 0 \tag{2.20}$$

$$\begin{bmatrix} \Delta P_k \\ \Delta Q_k \\ \Delta P_{WT2,k} \end{bmatrix}^i = \begin{bmatrix} \dfrac{\partial P_k^{cal}}{\partial \theta_k} & \dfrac{\partial P_k^{cal}}{\partial V_k} V_k & 0 \\ \dfrac{\partial Q_k^{cal}}{\partial \theta_k} & \left(\dfrac{\partial Q_k^{cal}}{\partial V_k} - \dfrac{\partial Q_g}{\partial V_k}\right) V_k & \dfrac{\partial Q_g}{\partial s} \\ 0 & \dfrac{\partial P_{WT2,k}}{\partial V_k} V_k & \dfrac{\partial P_{WT2,k}}{\partial s} \end{bmatrix}^i \begin{bmatrix} \Delta\theta_k \\ \dfrac{\Delta V_k}{V_k} \\ \Delta s \end{bmatrix}^i . \tag{2.21}$$

Accordingly, the state variable *s* is updated according to $s^{i+1} = s^i + \Delta s^i$ after each iteration.

2.5 Modeling of semi-variable speed wind generators (SSWGs)

This wind generator is equipped with a wound-rotor induction generator (WRIG) and a diode bridge that electronically controls an external resistor, R_{ext} [Burnham et al., 2009], added in the rotor circuit as seen in Figure 2.3(a). The resistor adjustment allows maintaining the generated active power at a specified value. Moreover, the turbine is constructed with a pitch

angle mechanism that enables an efficient power regulation above the rated wind speed, thus mitigating the mechanical stress and transient loads of the mechanical components of the wind generator.

In this case, the generator's slip cannot be regarded as the state variable because the resistor connected to the rotor circuit is also adjusted to achieve a desired power. In order to overcome this inconvenience, the total resistance of the rotor circuit, $(R_2+R_{ext})/s$, can be considered a single unknown variable, R_x [Divya and Rao, 2006].

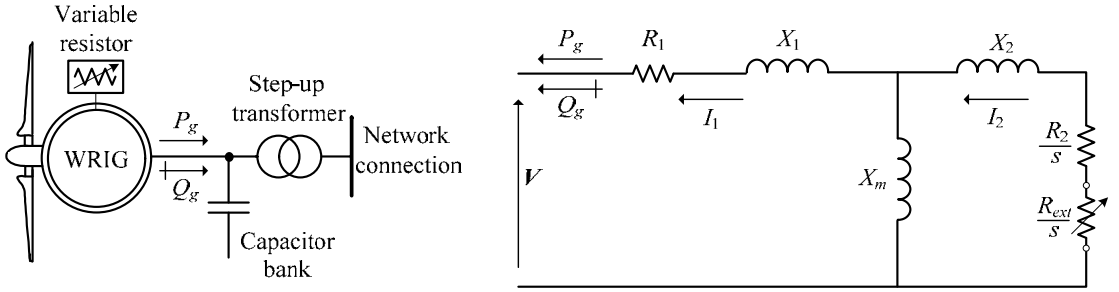

(a) (b)

Figure 2.3: (a) Schematic representation of a SSWG, and (b) steady-state equivalent circuit model of the SSWG.

Hence, stator and rotor currents as well as active and reactive powers will be dependent functions on R_x, and can be determined by (2.22)-(2.25) based on Figure 2.3(b), whose derivation is similar to that of the FSWG model shown in Appendix B but considers R_x instead of R_2/s:

$$Q_{g,ss}\left(V,R_x\right)=-V^2\left\{\frac{A'R_x^2+B}{\left[C'R_x-D\right]^2+\left[E'R_x+F\right]^2}\right\} \tag{2.22}$$

$$P_{g,ss}\left(V,R_x\right)=-V^2\left\{\frac{K'R_x{}^2+H'R_x+L}{\left[C'R_x-D\right]^2+\left[E'R_x+F\right]^2}\right\} \tag{2.23}$$

$$I_{1,ss}^2\left(V,R_x\right)=V^2\left\{\frac{\left[K'R_x{}^2+H'R_x+L\right]^2+\left[A'R_x^2+B\right]^2}{\left(\left[C'R_x-D\right]^2+\left[E'R_x+F\right]^2\right)^2}\right\} \tag{2.24}$$

$$I_{2,ss}^2\left(V,R_x\right)=V^2\left\{\frac{\left[M'R_x+N\right]^2+\left[T'R_x-W\right]^2}{\left(\left[C'R_x-D\right]^2+\left[E'R_x+F\right]^2\right)^2}\right\}, \tag{2.25}$$

where the constants *A*', *C*', *E*', *K*', *H*', *M*' and *T*' are associated with the generator's stator resistance and reactances.

For the purpose of power flow calculations, the reactive power output $Q_{g,ss}$ of the SSWG is computed iteratively, while its active power $P_{g,ss}$ is set to a fixed value obtained from the wind generator power curve, i.e., $P_{g,ss} = P_{g,ss}^{sp}$. Consequently, assuming no core losses in the induction machine exist, the mechanical power, $P_{m,ss}$, is computed by

$$P_{m,ss} = P_{g,ss}^{sp} + P_{losses,s} + P_{losses,r} = P_{g,ss}^{sp} + 3I_{1,ss}^2 R_1 + 3I_{2,ss}^2 R_2 \tag{2.26}$$

where $P_{losses,s}$ and $P_{losses,r}$ are the three-phase stator and rotor power losses, respectively. The slip's value approaches zero as the generator is closer to its rated operation; hence, the converted power, P_{conv}, and the active power mismatch associated with the internal energy balance, ΔP_{WT3}, is

$$P_{conv} = -I_{2,ss}^2 R_2 \left(\frac{1-s}{s} \right) \approx -I_{2,ss}^2 R_2 \left(\frac{1}{s} \right) = -I_{2,ss}^2 R_x \tag{2.27}$$

$$\begin{aligned} \Delta P_{WT3} &= -P_{g,ss}^{sp} - \left[\left(3I_{1,ss}^2 R_1 + 3I_{2,ss}^2 R_2 \right) + I_{2,ss}^2 R_x \right] \\ &\approx -P_{g,ss}^{sp} - \left(3I_{1,ss}^2 R_1 + I_{2,ss}^2 R_x \right) \end{aligned} . \tag{2.28}$$

Based on (2.27) and (2.28) and assuming that the wind generator is connected at node *k* of the power system, the Newton-based power flow formulation is given by

$$\Delta P_k = P_{g,ss}^{sp} - P_{dk} - P_k^{cal} = 0 \tag{2.29}$$

$$\Delta Q_k = Q_{g,ss}(V, R_x) - Q_{dk} - Q_k^{cal} = 0 \tag{2.30}$$

$$\Delta P_{WT3,k} = -P_{g,ss}^{sp} - \left(3I_{1,ss}^2 R_1 + I_{2,ss}^2 R_x \right) = 0 \tag{2.31}$$

$$\begin{bmatrix} \Delta P_k \\ \Delta Q_k \\ \Delta P_{WT3,k} \end{bmatrix}^i = \begin{bmatrix} \dfrac{\partial P_k^{cal}}{\partial \theta_k} & \dfrac{\partial P_k^{cal}}{\partial V_k} V_k & 0 \\ \dfrac{\partial Q_k^{cal}}{\partial \theta_k} & \left(\dfrac{\partial Q_k^{cal}}{\partial V_k} - \dfrac{\partial Q_{g,ss}}{\partial V_k} \right) V_k & \dfrac{\partial Q_{g,ss}}{\partial R_x} \\ 0 & \dfrac{\partial P_{WT3,k}}{\partial V_k} V_k & \dfrac{\partial P_{WT3,k}}{\partial R_x} \end{bmatrix}^i \begin{bmatrix} \Delta \theta_k \\ \dfrac{\Delta V_k}{V_k} \\ \Delta R_x \end{bmatrix}^i . \tag{2.32}$$

Accordingly, the state variable R_x is updated according to $R_x^{i+1} = R_x^i + \Delta R_x^i$ after each iteration.

2.6 Modeling of variable-speed wind generators (VSWGs)

An essential characteristic of the VSWG is that its active blade-pitch control enables them to regulate the aerodynamic power in a wider range compared to those with fixed speed operation. The decoupling technique used to operate and control the wind generator allows the rotor to act as a flywheel (accelerating or decelerating) to endow the wind generators with certain active power controllability. In addition to this, the use of power electronic devices makes them more attractive for taking over conventional power generation since they can also provide static and dynamic reactive power control. The existing VSWG can be further subdivided into two main groups, that is, doubly-fed induction generators (DFIGs) and wind generators with full-scale power converters. Both contain a voltage source converter (VSC) which is responsible for controlling the machine currents and another VSC connected to the grid for reactive power support purposes. The former VSWG makes use of a wound rotor induction generator (WRIG) whilst the latter may be fashioned with either a WRIG, a wound rotor synchronous generator (WRSG) or a permanent magnet synchronous generator (PMSG). In this section, the DFIG and PMSG-based wind generators are addressed. Both models are created in a rather simple fashion where the main assumptions are the following: (i) the power losses in the back-to-back (B-B) converters are neglected; (ii) because there is no explicit representation of the DC link, relating DC quantities with AC quantities is not possible. Nevertheless, in chapter 4 an enhanced DFIG model for power flow studies and dynamic simulations is presented with which the aforementioned shortcomings are overcome.

2.6.1 Modeling of doubly-fed induction generators (DFIGs)

Currently, this is the most popular scheme of wind turbines used for wind power extraction, where the stator is directly connected to the grid through a power transformer, while a B-B converter is used to connect the rotor of the generator to the power transformer and grid, as shown in Figure 2.4(a). An advantage of this system is that the converter enables a decoupling between the electrical frequency of the system and the mechanical frequency of the rotor. This decoupled control permits the separate handling of the active and reactive powers in the DFIG.

In the case of active power control, the decoupled *d-q* vector control is used to ensure a maximum energy capture when the wind speed is below the rated value, which is referred to as maximum power tracking (MPT). On the other hand, if the wind speed is above nominal speed, a blade-pitch angle control acts to limit the amount of active power injected into the network, preventing the wind turbine from suffering mechanical damage. Regarding the reactive power control, the B-B converter is operated according to the reactive power control mode set in the DFIG.

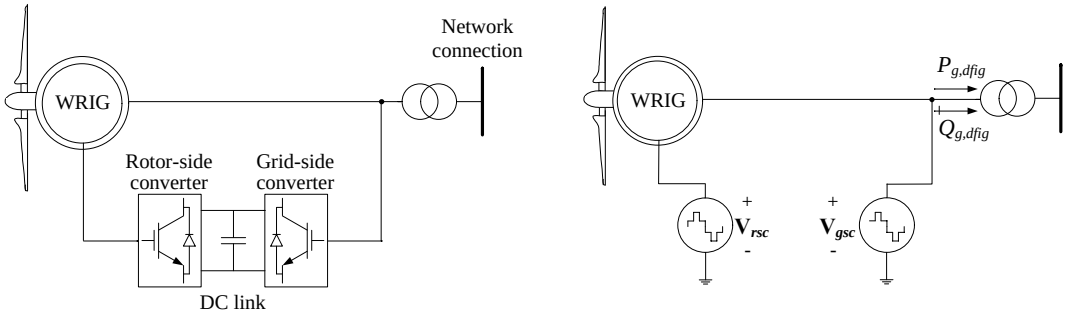

(a) (b)

Figure 2.4: DFIG: (a) schematic diagram, (b) model for power flow studies.

If the machine is operated at a fixed power factor, this wind generator can be treated in the power flow formulation as a *PQ* node with a fixed power factor [Divya and Rao, 2006], [Liu et al., 2008], where $P_{g,dfig}$ is the generated active power obtained from the power curve, and $Q_{g,dfig}$ is the reactive power output computed as $Q_{g,dfig} = P_{g,dfig}\ tan(\varphi)$, where φ is the power factor angle, as depicted in Figure 2.4(b). Therefore, if the VSWG-DFIG is connected at node *k*, the linearized set of power mismatch equations that must be included in the entire set of linearized equations to be solved iteratively are given by

$$\Delta P_k = P_{g,dfig} - P_{dk} - P_k^{cal} = 0 \tag{2.33}$$

$$\Delta Q_k = Q_{g,dfig} - Q_{dk} - Q_k^{cal} = 0 \tag{2.34}$$

$$\begin{bmatrix} \Delta P_k \\ \Delta Q_k \end{bmatrix}^i = \begin{bmatrix} \dfrac{\partial P_k^{cal}}{\partial \theta_k} & \dfrac{\partial P_k^{cal}}{\partial V_k} V_k \\ \dfrac{\partial Q_k^{cal}}{\partial \theta_k} & \dfrac{\partial Q_k^{cal}}{\partial V_k} V_k \end{bmatrix}^i \begin{bmatrix} \Delta \theta_k \\ \dfrac{\Delta V_k}{V_k} \end{bmatrix}^i \tag{2.35}$$

Note that in recent breakthroughs in power electronic equipment, the DFIGs are being endowed with reactive power capability similar to that of the synchronous generators. Hence, from the power system flow perspective they can also be treated as *PV* nodes where the active power, $P_{g,dfig}$, can be known from the power curve and the reactive power output, $Q_{g,dfig}$, is computed during the iterative process to achieve a specified voltage. For that reason, if the VSWG-DFIG is connected at node *k* and operates with a voltage control strategy, the linearized set of power mismatch equations is given by

$$\Delta P_k = P_{g,dfig} - P_{dk} - P_k^{cal} = 0 \tag{2.36}$$

$$\begin{bmatrix} \Delta P_k \\ \Delta Q_k \end{bmatrix}^i = \begin{bmatrix} \dfrac{\partial P_k^{cal}}{\partial \theta_k} & 0 \\ 0 & 0 \end{bmatrix}^i \begin{bmatrix} \Delta \theta_k \\ 0 \end{bmatrix}^i . \tag{2.37}$$

2.6.2 Modeling of permanent magnet synchronous generator (PMSG) – based wind generator

This type of wind generator possesses a PMSG and a full-rated converter to connect the generator to the network, resulting in complete speed and reactive power control [Hong-Woo et al., 2010]. Hence, all the generated power is supplied to the power system through a machine-side converter and grid-side converter. The schematic diagram of this topology is shown in Figure 2.5(a). Reactive power support is one of the characteristics that make this machine attractive for wind power production. In this case, the inclusion of the explicit representation of the wind generator step-up transformer is considered, which allows for direct voltage magnitude control at the high-voltage side of the transformer. The model for power flow studies is shown in the Figure 2.5(b) in which $P_{g,pmsg}$ represents the output power set by the wind generator power curve for a given wind speed, $\mathbf{V}_{msc}$ and $\mathbf{V}_{gsc}$ are the voltage at the machine-side converter and grid-side converter terminal, respectively, and $\mathbf{Z}_{st}$ is the step-up transformer impedance.

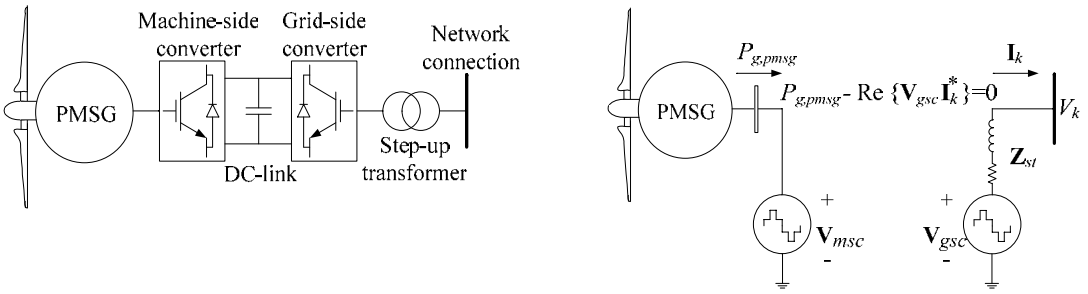

(b) (b)

Figure 2.5: PMSG-based wind generator: (a) schematic diagram, (b) model for power flow studies.

The power flow equations for the PMSG-based wind generator are derived assuming the following voltage at the grid-side converter terminal: $\mathbf{V}_{gsc} = V_{gsc}e^{j\delta gsc}$. Based on Figure 2.5(b), the active and reactive powers flowing from the grid-side converter terminal to the *k-th* bus are:

$$P_{gsc-k} = V_{gsc}^2 G_{st} + V_{gsc}V_k\left[G_{st}\cos\left(\delta_{gsc}-\theta_k\right)+B_{st}\sin\left(\delta_{gsc}-\theta_k\right)\right] \tag{2.38}$$

$$Q_{gsc-k} = -V_{gsc}^2 B_{st} + V_{gsc}V_k\left[G_{st}\sin\left(\delta_{gsc}-\theta_k\right)-B_{st}\cos\left(\delta_{gsc}-\theta_k\right)\right] \tag{2.39}$$

For the active and reactive powers at bus *k*, the subscripts *gsc* and *k* are exchanged in (2.38) and (2.39); therefore, the NR-based power flow formulation is given by

$$\Delta P_k = -P_{k-gsc} - P_{Lk} - P_k^{cal} = 0 \tag{2.40}$$

$$\Delta Q_k = -Q_{k-gsc} - Q_{Lk} - Q_k^{cal} = 0 \tag{2.41}$$

$$\Delta P_{WT4,k} = P_{g,pmsg} - P_{gsc-k} = 0 \tag{2.42}$$

$$\begin{bmatrix}\Delta P_k \\ \Delta Q_k \\ \Delta P_{WT4,k}\end{bmatrix}^i = \begin{bmatrix} \dfrac{\partial P_k^{cal}}{\partial\theta_k}+\dfrac{\partial P_{k-gsc}}{\partial\theta_k} & \dfrac{\partial P_{k-gsc}}{\partial V_{gsc}}V_{gsc} & \dfrac{\partial P_{k-gsc}}{\partial\delta_{gsc}} \\ \dfrac{\partial Q_k^{cal}}{\partial\theta_k}+\dfrac{\partial Q_{k-gsc}}{\partial\theta_k} & \dfrac{\partial Q_{k-gsc}}{\partial V_{gsc}}V_{gsc} & \dfrac{\partial Q_{k-gsc}}{\partial\delta_{gsc}} \\ \dfrac{\partial P_{WT4,k}}{\partial\theta_k} & \dfrac{\partial P_{WT4,k}}{\partial V_{gsc}}V_{gsc} & \dfrac{\partial P_{WT4,k}}{\partial\delta_{gsc}} \end{bmatrix}^i \begin{bmatrix}\Delta\theta_k \\ \dfrac{\Delta V_{gsc}}{V_{gsc}} \\ \Delta\delta_{gsc}\end{bmatrix}^i . \tag{2.43}$$

Note that equation (2.42) represents the power constraint in the AC/DC/AC converter in which active power losses are neglected.

2.7 Initialization of wind generators

As is commonly understood, adequate initial conditions must be chosen for the state variables to be solved when the NR algorithm is used. Hence, proposals to initialize the state variables of wind generators are described in this section.

In the case of FP-FSWG, a good initial slip value to execute simulations is given by $s^{(0)} = s_{nom}/2$, which implies starting approximately at the middle of the interval of mechanical speed values that the wind generator could experience: from low to high wind speeds.

Regarding PR-FSWG and SSWG, the initializations for the NR algorithm may be estimated by equations (2.44) and (2.45) reported in Table 2.1. These equations are obtained by solving (2.8) and (2.23) for s and R_x, respectively, assuming that the active power output can be obtained from the power curve for a given wind speed.

Table 2.1: Initializations for PR-FSWG and SSWG

PR-FSWG (2.44)	SSWG (2.45)
$s^{(0)} = min\left\lvert\frac{-b \pm \sqrt{b^2 - 4ac}}{2a}\right\rvert$	$R_x^{(0)} = min\left\lvert\frac{-b \pm \sqrt{b^2 - 4ac}}{2a}\right\rvert$
$a = (D^2 + F^2)P_{g,pr}^{sp} + LV^2$	$a = (C'^2 + E'^2)P_{g,ss}^{sp} + K'V^2$
$b = -2CDP_{g,pr}^{sp} + 2EFP_{g,pr}^{sp} + HV^2$	$b = -2C'DP_{g,ss}^{sp} + 2E'FP_{g,ss}^{sp} + H'V^2$
$c = (C^2 + E^2)P_{g,pr}^{sp} + KV^2$	$c = (D^2 + F^2)P_{g,ss}^{sp} + LV^2$

2.8 Modeling of wind farms

A wind farm is a group of wind generators located in the same geographic area which can be placed onshore or offshore forming itself a distribution system. The radial collector system may connect up to several hundred wind generators transporting their generated power to the point of common coupling of the network (PCC). In this thesis, all the wind generators making up the wind farm are simulated, as shown in Figure 2.6. This means that the wind farm is not modelled as a single equivalent wind generator producing the total amount of power delivered by the collection of generators. For instance, for a wind farm constituted by n fixed-pitch fixed-speed wind generators, the number of equations to be appended to the set of equations will be $3\ x\ n$, as reported in (2.46).

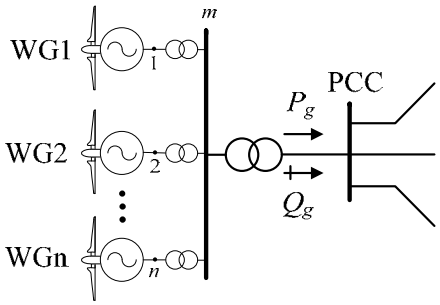

Figure 2.6: Schematic diagram of a wind farm

$$\left.\begin{aligned}\Delta P_k &= P_{gk} - P_{dk} - P_k^{cal} \\ \Delta Q_k &= Q_{gk} - Q_{dk} - Q_k^{cal} \\ \Delta P_{WTk} &= -\left(P_{mk} - P_{convk}\right)\end{aligned}\right\} \forall k = 1\ldots n \tag{2.46}$$

Therefore, the active and reactive power balances at node *m* are expressed as,

$$\Delta P_m = -\sum_{k\in m} P_{mk} - P_{dm} - \sum_{l\in m} P_{ml} \tag{2.47}$$

$$\Delta Q_m = -\sum_{k\in m} Q_{mk} - Q_{dm} - \sum_{l\in m} Q_{ml} \tag{2.48}$$

where P_{ml} and Q_{ml} are the active and reactive powers flowing through the branch that connects the node *m* with the PCC. This formulation is used in our simulations since it is applicable disregarding the type of wind generators composing the wind farm.

2.9 Conclusions

This chapter has presented mathematical models of fixed-speed, semi-variable speed and variable-speed wind generators. The FSWG and SSWG are derived from the equivalent circuit representation of the induction generator. Emphasis has been placed on their efficient implementation within the unified framework afforded by the Newton-Raphson method, for efficient power flow solutions comprising a large number of wind generators. Guidelines for the initializations of the state variables associated with the various types of wind generators have been provided.

Chapter 3

POWER FLOWS WITH AUTOMATIC LOAD-FREQUENCY CONTROL DEVICES

3.1 Introduction

The wind generator models developed in the preceding chapter are further developed for inclusion into the power flow formulation where the effect of automatic load-frequency control devices are taken into account in order to be able to assess the role that wind farms may have in achieving frequency regulation. This is carried out by reformulating the individual wind generator models to incorporate the effect of frequency deviations that commonly take place in the electrical power network. The mathematical models of wind turbines presented in this chapter rely primarily on the concept of power injections. The point should be made that, in practice, FSWGs are not equipped to provide frequency support but owing to their physical construction they do respond naturally to frequency deviations and voltage changes, with ensuing variations in their active and reactive power outputs. A different situation arises with VSWGs which owing to their finely regulated voltages and currents they do possess the ability to participate in the primary frequency regulation of the system by maintaining a certain degree of spinning reserve through the prior deloading of the wind turbine [Ramtharan et al., 2007], [Chowdhury et al., 2008], [Morren et al., 2006], [Moutis et al., 2009], [Teninge et al., 2009], [de Almeida and Peças Lopes, 2007], [de Almeida et al., 2006].

3.2 Power flow formulation with automatic load-frequency control devices and wind generators

The power flow formulation with automatic load-frequency control (PFALFC) devices includes the system frequency deviation as a state variable, which is calculated together with all the network's nodal voltages [Okamura et al., 1975]. Therefore, when a load or generation perturbation is applied, the operating point obtained by the PFALFC method is at an

off-nominal frequency value. The PFALFC is herein expanded to incorporate the developed wind generator models. Such models are implemented in such a way that the electrical network state variables, including frequency deviation and those related to wind generators, are solved simultaneously during the iterative process. The Newton-Raphson method is selected to solve the whole set of equations with the aim of taking advantage of its good convergence characteristics, as reported in Appendix A. In this context, all wind generator models developed herein can be readily included in the power flow formulation as shown in (3.1), where $\Delta f(X_{WG})$ and X_{WG} represent the power balance equation of each wind generator and its associated state variable, respectively. The power mismatch equations are denoted by ΔP and ΔQ at each network node and Δf is the system frequency deviation from its nominal value:

$$\begin{bmatrix} \Delta P \\ \Delta Q \\ \hline \Delta f(X_{WG}) \end{bmatrix}^i = -\left[\begin{array}{cc:cc} \frac{\partial \Delta P}{\partial \theta} & \frac{\partial \Delta P}{\partial V} & \frac{\partial \Delta P}{\partial X_{WG}} & \frac{\partial \Delta P}{\partial \Delta f} \\ \frac{\partial \Delta Q}{\partial \theta} & \frac{\partial \Delta Q}{\partial V} & \frac{\partial \Delta Q}{\partial X_{WG}} & \frac{\partial \Delta Q}{\partial \Delta f} \\ \hdashline \frac{\partial f(X_{WG})}{\partial \theta} & \frac{\partial f(X_{WG})}{\partial V} & \frac{\partial f(X_{WG})}{\partial X_{WG}} & \frac{\partial f(X_{WG})}{\partial \Delta f} \end{array}\right]^i \begin{bmatrix} \Delta\theta \\ \Delta V \\ \hline \Delta X_{WG} \\ \Delta\Delta f \end{bmatrix}^i . \qquad (3.1)$$

Unlike the conventional formulation of power flows, a slack generator does not exist in the PFALFC; a reference generator is only considered whose voltage phase angle serves as the reference against which all other remaining nodal voltage phase angles of the network are measured. Furthermore, one can consider multiple generator regulators that respond to frequency changes when a load/generation perturbation is presented. Table 3.1 shows a classification of bus types and their associated variables that can be used in the PFALFC program.

Table 3.1: Classification of bus types for the PFALFC

Bus types	Known variables	Unknown variables
Reference	P_G ,Q_G ,θ	V, Δf
Generator regulator	P_G ,Q_G	V, θ
PV Generator	P_G ,V	Q_G ,θ
Fixed load	P_L ,Q_L	V, θ
Frequency and voltage dependent load	P_{L_set} ,Q_{L_set}	V, θ

The synchronous generator models as well as the load models used in this work are briefly discussed below, where all presented equations are given in the per-unit (p.u.) system, unless otherwise stated.

3.2.1 Synchronous generator models

Two synchronous generator models from the four presented in [Okamura et al., 1975] are addressed in this section, since this work focuses on wind generator models within the context of the PFALFC. The first model represents a generator regulator that adjusts its active power output, P_G, and reactive power output, Q_G, according to (3.2)-(3.6), which are functions of the frequency deviation value estimated at each power flow iteration:

$$P_G = P_{G\_set} + \Delta P_G \tag{3.2}$$

$$\Delta P_G = -\frac{P_R}{R}\Delta f \tag{3.3}$$

$$P_{G\min} \le P_G \le P_{G\max} \tag{3.4}$$

$$Q_G = Q_{G\_set} + a_Q \Delta P_G + b_Q \Delta P_G^{\,2} \tag{3.5}$$

$$Q_{G\min} \le Q_G \le Q_{G\max} \tag{3.6}$$

where P_{G_set} and Q_{G_set} are the specified active and reactive powers of the generator, respectively, P_R is the nominal active power, R is the speed droop of the corresponding generator, a_Q and b_Q are the coefficients of the reactive power generation, and the subscripts *max* and *min* represent maximum and minimum values.

The second model employed in this work corresponds to the conventional *PV* generator, where its generated active power, P_G, and its terminal voltage magnitude, V, are set to specified values during the simulation process. Constant voltage operation is only possible if the generator reactive power design limits are not violated, i.e. $Q_{G\,\min} < Q_G < Q_{G\,\max}$. If the generator cannot provide the necessary reactive power support to constrain the voltage magnitude at the specified value then the reactive power is fixed at the violated limit, and the voltage magnitude is freed. In this case, the generated active power P_G and reactive power Q_G are specified, while nodal voltage magnitude V and phase angle θ are computed.

3.2.2 Load model

Most of the loads in power systems are voltage and frequency dependent, and their demanded power varies according to changes in these variables. The static representation of their active power, P_d, and reactive power, Q_d, is described by the following [Okamura et al., 1975], [Kundur, 1994]:

$$P_d = P_{L\_set}\left(1+K_p\,\Delta f\right)\left(p_p + p_c\left(\frac{V}{V_{LB}}\right)+ p_z\left(\frac{V}{V_{LB}}\right)^2\right) \tag{3.7}$$

$$Q_d = Q_{L\_set}\left(1+K_q\,\Delta f\right)\left(q_p + q_c\left(\frac{V}{V_{LB}}\right)+ q_z\left(\frac{V}{V_{LB}}\right)^2\right) \tag{3.8}$$

where P_{L_set} and Q_{L_set} are the specified active and reactive powers drawn by the load, respectively, V_{LB} is the nominal operating voltage of the node where the load is connected, K_p and K_q are the coefficients of the load-frequency characteristic, whereas p_p, p_c, p_z, q_p, q_c and q_z are the coefficients of the load-voltage characteristic. Note that if fixed loads need to be simulated, the coefficients p_c, p_z, q_c, q_z, K_p and K_q must be set to zero.

3.3 Modeling of FSWG for PFALFC calculations

The steady-state equivalent circuit model of the induction generator shown in Figure 3.1 is adopted, where the only simplification made in the model is related to the exclusion of the core losses. The equivalent circuit can be used to determine a wide variety of steady-state performance characteristics of the induction machine such as speed, current variations, power losses, etc. The circuit shows that the power transferred from the stator across the air gap together with the stator and rotor currents depend on the machine's slip, which is the difference between the synchronous speed ω_s and the mechanical speed ω_m. The slip can also be expressed in terms of the system's frequency deviation Δf, and the mechanical angular speed of the rotor ω_m, as

$$s = \frac{1+\Delta f - \omega_m}{1+\Delta f}\ . \tag{3.9}$$

This implies, therefore, that the active and reactive powers generated by a directly

grid-connected wind generator will vary according to changes in the system's frequency and in the mechanical angular speed of the rotor, as shown in Figure 3.2.

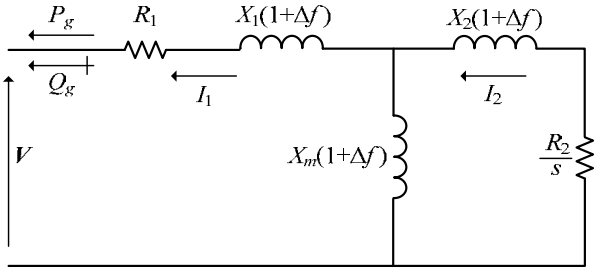

Figure 3.1: Steady-state equivalent circuit model of the induction machine taking into account the system frequency deviation.

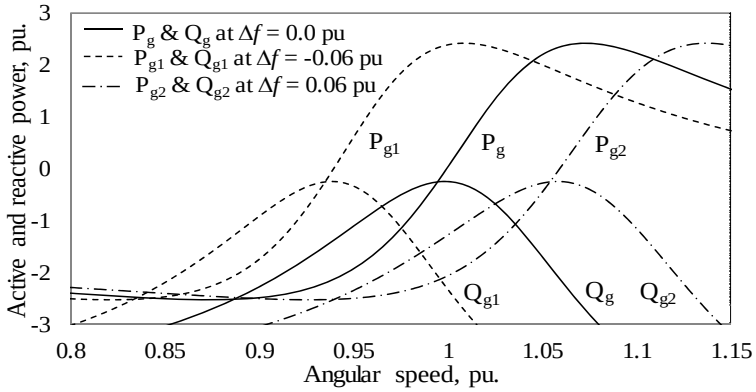

Figure 3.2: Response of directly grid-connected wind generators to frequency variations in the network.

Based on the previously mentioned information, the FSWG models, such as the fixed-pitch and pitch-regulated fixed-speed wind generator models can be suitably derived as a function of the frequency deviation by using the power injection concept. Contrary to the developed models for conventional power flow calculations, though, where the slip of the FSWG was taken as the state variable, the mechanical angular speed of the generator rotor $\omega_{m,}$ is used as the wind generator state variable within the iterative process. Hence, the power converted from the mechanical to electrical form P_{conv}, the generated powers P_g and Q_g, the rotor current I_2 and the stator current I_1 are expressed as follows:

$$P_{conv} = -I_2^2 R_2 \left(\frac{\omega_m}{1 + \Delta f - \omega_m} \right) \tag{3.10}$$

$$Q_g\left(V,\omega_m,\Delta f\right)=-V^2\left\{\frac{\alpha A+\alpha\sigma^2 B}{\left[C-\alpha\sigma D\right]^2+\left[\alpha E+\sigma F\right]^2}\right\} \tag{3.11}$$

$$P_g\left(V,\omega_m,\Delta f\right)=-V^2\left\{\frac{K+\alpha\sigma H+\sigma^2 L}{\left[C-\alpha\sigma D\right]^2+\left[\alpha E+\sigma F\right]^2}\right\} \tag{3.12}$$

$$I_1^2\left(V,\omega_m,\Delta f\right)=V^2\left\{\frac{\left[K+\alpha\sigma H+\alpha\sigma^2 L\right]^2+\left[\alpha A+\alpha\sigma^2 B\right]^2}{\left(\left[C-\alpha\sigma D\right]^2+\left[\alpha E+\sigma F\right]^2\right)^2}\right\} \tag{3.13}$$

$$I_2^2\left(V,\omega_m,\Delta f\right)=V^2\left\{\frac{\left[\alpha\sigma M+\sigma^2 N\right]^2+\left[\sigma T-\alpha\sigma^2 W\right]^2}{\left(\left[C-\alpha\sigma D\right]^2+\left[\alpha E+\sigma F\right]^2\right)^2}\right\} \tag{3.14}$$

where the constants *A* to *W* are the same as those of FSWG models for the conventional solution of power flows and are given in Appendix B, whereas $\alpha=\left(1+\Delta f\right)$ and $\sigma=\left(1+\Delta f-\omega_m\right)$.

3.3.1 Fixed-pitch FSWG for PFALFC calculations

The extracted power from the wind P_m of a fixed-pitch FSWG (FP-FSWG) is calculated by using (2.2)-(2.5). Clearly, it is a function of the rotor angular speed ω_m among other variables. In this case, the only unknown variable is the mechanical angular speed of the generator. Consequently, this parameter acts as the state variable within the iterative process which permits to find the internal equilibrium point in the FP-FSWG given by the conversion process of mechanical power into electrical power. In the framework of the PFALFC method, the set of power flow mismatch equations that has to be solved when a FP-FSWG is connected at the node *k* of the system is

$$\Delta P_k=P_g\left(V,\omega_m,\Delta f\right)-P_{dk}-P_k^{cal} \tag{3.15}$$

$$\Delta Q_k=Q_g\left(V,\omega_m,\Delta f\right)-Q_{dk}-Q_k^{cal} \tag{3.16}$$

$$\Delta P_{WT1,k}=-\left(P_m-P_{conv}\right)=-\left[P_m+I_2^2 R_2\left(\frac{\omega_m}{1+\Delta f-\omega_m}\right)\right] \tag{3.17}$$

The set of linearized equations (3.18) is integrated into the set of linearized power mismatch equations of the whole network (3.1) to compute a new equilibrium point through a power flow solution:

$$\begin{bmatrix} \Delta P_k \\ \Delta Q_k \\ \Delta P_{WT1,k} \end{bmatrix}^i = \begin{bmatrix} \dfrac{\partial P_k^{cal}}{\partial \theta_k} & \left(\dfrac{\partial P_k^{cal}}{\partial V_k} - \dfrac{\partial P_g}{\partial V_k}\right) V_k & -\dfrac{\partial P_g}{\partial \omega_m} & -\dfrac{\partial P_g}{\partial \Delta f} \\ \dfrac{\partial Q_k^{cal}}{\partial \theta_k} & \left(\dfrac{\partial Q_k^{cal}}{\partial V_k} - \dfrac{\partial Q_g}{\partial V_k}\right) V_k & -\dfrac{\partial Q_g}{\partial \omega_m} & -\dfrac{\partial Q_g}{\partial \Delta f} \\ 0 & \dfrac{\partial P_{WT1,k}}{\partial V_k} V_k & \dfrac{\partial P_{WT1,k}}{\partial \omega_m} & \dfrac{\partial P_{WT1,k}}{\partial \Delta f} \end{bmatrix}^i \begin{bmatrix} \Delta \theta_k \\ \dfrac{\Delta V_k}{V_k} \\ \Delta \omega_m \\ \Delta \Delta f \end{bmatrix}^i . \qquad (3.18)$$

In this case, the generator angular speed is updated after the *i-th* iteration as given by $\omega_m^{\,i+1} = \omega_m^{\,i} + \Delta\omega_m^{\,i}$.

3.3.2 Pitch-regulated FSWG for PFALFC calculations

A pitch-regulated FSWG has practically the same mechanical construction as the FP-FSWG; however, the PR-FSWG has a blade-pitch angle mechanism which operates for wind speeds beyond a rated value to limit the power extracted from the wind [Bianchi et al., 2006]. A typical pitch-angle controller is shown in Figure 3.3, which takes the power output $P_{g,pr}$ of the wind generator as the input signal and regulates the pitch angle β through a *PI* controller.

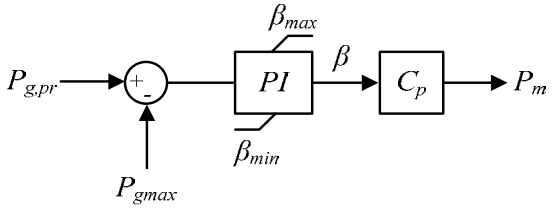

Figure 3.3: Typical blade pitch-angle controller.

(a) Mathematical model when the PR-FSWG is operating below its maximum power

The mathematical equations representing the FP-FSWG model are also valid to represent the steady-state operation of a PR-FSWG for an operating condition where the generated active power is below the specified value P_{gmax}, i.e., equations (3.15) to (3.17) apply for a PR-FSWG when its output active power $P_{g,pr} < P_{gmax}$.

(b) Mathematical model when the PR-FSWG is operating above maximum power

When the output power surpasses P_{gmax}, the blade-pitch angle controller is activated. In this case, the controller sets $P_{g,pr}$ at the reference value P_{gmax}, whereas the reactive power Q_g must be calculated within the iterative process. By thus neglecting the core losses in the induction machine, the mechanical power can be computed by

$$P_m = P_{gmax} + P_{losses,s} + P_{losses,r} = P_{gmax} + 3I_1^2 R_1 + 3I_2^2 R_2 \tag{3.19}$$

where $P_{losses,s}$ and $P_{losses,r}$ are the three-phase stator and rotor power losses, respectively.

Assuming that the PR-FSWG is connected at node *k*, the values of the network state variables and the wind generator that satisfy the mismatch equations (3.20)-(3.21) are obtained by solving (3.23). This last equation has to be accommodated with the rest of the linearized power mismatch equations of the network for a unified power flow solution:

$$\Delta P_k = P_{gmax} - P_{dk} - P_k^{cal} \tag{3.20}$$

$$\Delta Q_k = Q_g\left(V, \omega_m, \Delta f\right) - Q_{dk} - Q_k^{cal} \tag{3.21}$$

$$\Delta P_{WT2,k} = -P_{gmax} - \left[\left(3I_1^2 R_1 + 3I_2^2 R_2\right) + I_2^2 R_2\left(\frac{\omega_m}{1+\Delta f - \omega_m}\right)\right] \tag{3.22}$$

$$\begin{bmatrix} \Delta P_k \\ \Delta Q_k \\ \Delta P_{WT2,k} \end{bmatrix}^i = \begin{bmatrix} \frac{\partial P_k^{cal}}{\partial \theta_k} & \frac{\partial P_k^{cal}}{\partial V_k} V_k & 0 & 0 \\ \frac{\partial Q_k^{cal}}{\partial \theta_k} & \left(\frac{\partial Q_k^{cal}}{\partial V_k} - \frac{\partial Q_g}{\partial V_k}\right) V_k & -\frac{\partial Q_g}{\partial \omega_m} & -\frac{\partial Q_g}{\partial \Delta f} \\ 0 & \frac{\partial P_{WT2,k}}{\partial V_k} V_k & \frac{\partial P_{WT2,k}}{\partial \omega_m} & \frac{\partial P_{WT2,k}}{\partial \Delta f} \end{bmatrix}^i \begin{bmatrix} \Delta\theta_k \\ \frac{\Delta V_k}{V_k} \\ \Delta\omega_m \\ \Delta\Delta f \end{bmatrix}^i \tag{3.23}$$

where the state variable ω_m is updated after each iteration as $\omega_m^{\,i+1} = \omega_m^{\,i} + \Delta\omega_m^{\,i}$, and $\Delta P_{WT2,k}$ represents the power balance inside the induction machine obtained by equating (3.10) and (3.19).

In summary, the next conditions must be considered when a PR-FSWG is included in the PFALFC program: if $P_{g,pr} < P_{gmax}$, then (2.2)-(2.5) and (3.15)-(3.17) must be used. If $P_{g,pr} \geq P_{gmax}$, then (3.20)-(3.22) must be used instead, setting $P_{g,pr} = P_{gmax}$.

From the software design perspective, the simulation starts by employing the

mathematical equations representing the FP-FSWG. The active power generated by the PR-FSWG is checked at the end of the second iteration because the first iteration generally provides an inaccurate approximation to the power flow solution. If $P_{g,pr}$ happens to be equal or greater than P_{gmax}, the next iteration is then executed using (3.20)-(3.22). Note that even when a high wind speed is selected and $P_{g,pr}$ was meant to surpass its maximum limit, the drop in the system frequency can force $P_{g,pr}$ to be less than P_{gmax}. In such a case, the equations (2.2)-(2.5) and (3.15)-(3.17) will continue being used during the iterative process.

3.4 Modeling of VSWG for PFALFC calculations and their contribution to frequency support

The increasing integration of wind power into power systems has provided the momentum for exploring alternatives to endow wind turbines with frequency regulation capability. In the case of the primary frequency regulation, the key aspect is to attain a spinning reserve of active power in order to compensate active power imbalances. This goal can be achieved by forcing the wind generator to operate in a suboptimal power output level, which is referred to as “deloading”. Thus, each deloaded wind turbine will not extract the maximum power from the wind during normal conditions in order to maintain a spinning reserve, which will permit a release of power when a power imbalance perturbation occurs [Ramtharan et al., 2007], [Chowdhury et al., 2008], [Morren et al., 2006], [Moutis et al., 2009], [Teninge et al., 2009], [de Almeida and Peças Lopes, 2007], [de Almeida at al., 2006].

One of the techniques employed to deload a wind turbine calls for the action of the blade pitch mechanism, as seen in Figure 3.4(a), [Chowdhury et al., 2008], [Moutis et al., 2009], [Teninge et al., 2009]. In this case, the pitch angle is increased from β to β_1 or β_2 (depending on the required level of deloading), resulting in different output powers obtained at the same rotor angular speed $\omega_{m,opt}$. Therefore, the pitch-angle controller acts like a conventional speed governor.

On the other hand, by shifting the operating point to the right of the wind turbine power curve, as shown in Figure 3.4(b), a wind turbine can attain a spinning reserve of active power to be delivered in case of a power imbalance [Ramtharan et al., 2007], [de Almeida and Peças Lopes, 2007]. A rotor over speeding $\omega_{m,new}$, however, is presented with this deloading technique which limits its application beyond the rated wind speed due to mechanical stress [Morren et al., 2006]. Both discussed approaches, though, can be simultaneously applied as presented in [de Almeida at al., 2006].

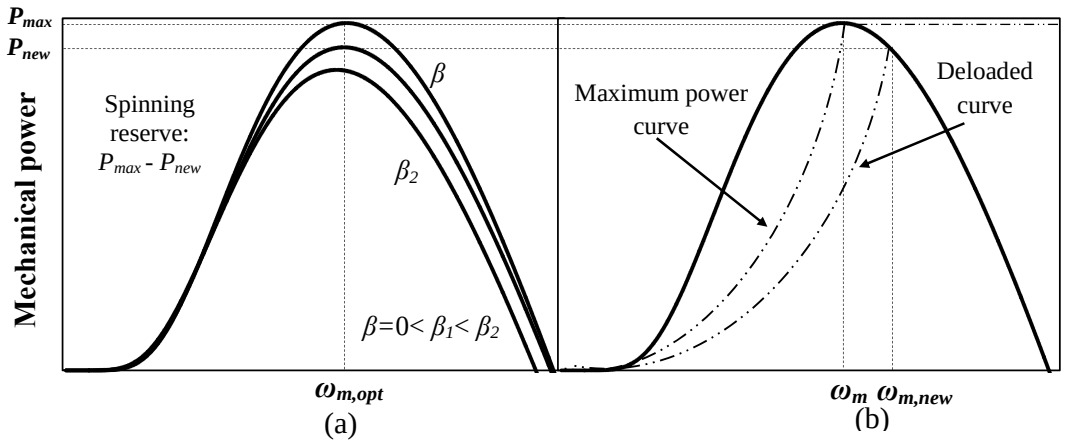

Figure 3.4: Achieving a spinning reserve: (a) by using the blade-pitch mechanism, and (b) by increasing the mechanical rotor angular speed.

Note that shifting the operating point towards the left of the power curve, shown in Figure 3.4(b), may also deload the wind turbine; however, when requiring frequency response, a rotor speed increase becomes necessary. In such a situation, a portion of the energy extracted from the wind will accelerate the rotor thus reducing the amount of power delivered to the network [Ramtharan et al., 2007].

3.4.1 DFIG with primary frequency regulation

The deloading of the wind turbine allows a DFIG to provide frequency support. Its response to frequency deviations will be dependent on its speed droop characteristic R and its power generation P_{G_set} (as seen in Figure 3.5) [Moutis et al., 2009], which is calculated according to the level of deloading of its wind turbine, η.

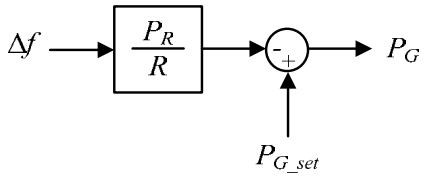

Figure 3.5: Automatic load-frequency control of a DFIG.

Hence, the active power generated by the DFIG is computed by using (3.24) and (3.25), where $P_{g,dfig}$ is the initial active power obtained from the power curve of the wind generator for any given wind speed:

$$P_{G\_set} = (1-\eta) P_{g,dfig} \tag{3.24}$$

$$P_G = P_{G\_set} - \frac{P_R}{R}\Delta f \ . \tag{3.25}$$

One of the most attractive features of this kind of wind generator is its reactive power control capability. The control strategy adopted to operate a DFIG defines if it will be absorbing or injecting reactive power. Therefore, depending on the reactive power control mode, a different set of power flow equations must be accommodated with the rest of the equations.

(a) Fixed power factor control mode

Given that the power factor is specified, the reactive power generated by the wind generator is computed according to $Q_G = P_{g,dfig}\, tan(\varphi)$, where φ stands for the power factor angle. Care should be taken, however, when choosing the value of the power factor so as not to exceed the reactive power limits, Q_{gmin} and $Q_{gmax,}$ imposed by the power electronic converter connected to the grid. Therefore, for a DFIG connected at node *k*, the power flow mismatch equations that must be solved simultaneously with the ones corresponding to the rest of the network are

$$\Delta P_k = P_G - P_{dk} - P_k^{cal} \tag{3.26}$$

$$\Delta Q_k = Q_G - Q_{dk} - Q_k^{cal} \tag{3.27}$$

$$\begin{bmatrix} \Delta P_k \\ \Delta Q_k \end{bmatrix}^i = \begin{bmatrix} \dfrac{\partial P_k^{cal}}{\partial \theta_k} & \dfrac{\partial P_k^{cal}}{\partial V_k} V_k & -\dfrac{\partial P_G}{\partial \Delta f} \\ \dfrac{\partial Q_k^{cal}}{\partial \theta_k} & \dfrac{\partial Q_k^{cal}}{\partial V_k} V_k & 0 \end{bmatrix}^i \begin{bmatrix} \Delta\theta_k \\ \dfrac{\Delta V_k}{V_k} \\ \Delta\Delta f \end{bmatrix}^i . \tag{3.28}$$

(b) Constant voltage magnitude control mode

In this control strategy, the voltage magnitude at the generator's terminals is specified, and its active power output is obtained from (3.24) and (3.25). Consequently, the PFALFC formulation for a DFIG controlling the voltage magnitude at its terminal *k* is given by

$$\Delta P_k = P_G - P_{Lk} - P_k^{cal} \tag{3.29}$$

$$\begin{bmatrix} \Delta P_k \\ 0 \end{bmatrix}^i = \begin{bmatrix} \dfrac{\partial P_k^{cal}}{\partial \theta_k} & 0 & -\dfrac{\partial P_G}{\partial \Delta f} \\ 0 & 0 & 0 \end{bmatrix}^i \begin{bmatrix} \Delta \theta_k \\ 0 \\ \Delta \Delta f \end{bmatrix}^i . \tag{3.30}$$

Despite the fact the reactive power mismatch equation of the voltage controlled node is not considered in the formulation, it is solved at each iterative step to assess whether or not the generator reactive power is within limits. If a limit violation occurs then the generated reactive power is fixed at that limit, and the voltage magnitude is freed. In this case, this model is converted into the DFIG model operating with a fixed power factor.

Note that the impact of the system's frequency on the stator electrical variables is considered to be negligible for both DFIG models. This is a reasonable assumption if we assume the electrical and mechanical rotor frequencies are decoupled: the voltage source converter connected to the slip rings of the rotor injects a current with a variable frequency to compensate for the difference between the mechanical and electrical frequencies [Ackerman, 2005].

3.4.2 PMSG-based wind generator with primary frequency regulation

Presently there is great interest in assessing how these wind generators can participate in the primary frequency control since they have been gaining prominence in power systems [Conroy and Watson, 2008]. Unlike a DFIG, the PMSG-based wind generator supplies its entire generated active power through its full-scale converter. Based on the electric circuit shown in Figure 2.3, a suitable model for PFALFC studies can be derived by explicitly including the representation of the wind generator step-up transformer.

Note that this model will also allow for direct voltage magnitude control at the transformer's high-voltage side for the cases where this reactive power control mode is selected. Assuming that the PMSG-based wind generator has a primary frequency controller represented by Figure 3.5, its generated active power will be determined by

$$P_{G\_set} = (1-\eta) P_{g,pmsg} \tag{3.31}$$

$$P_G = P_{G\_set} - \frac{P_R}{R} \Delta f \tag{3.32}$$

where $P_{g,pmsg}$ stands for the output power obtained from the wind generator power curve for a given wind speed. Depending on the adopted reactive power control strategy, a different set of power flow equations must be integrated with the rest of the network equations as shown next.

(a) Fixed power factor control mode

For a given power factor angle φ, the reactive power generated by this type of wind generator is calculated as $Q_G = P_{g,pmsg}\, tan(\varphi)$. Hence, having defined both generated powers, the set of power flow mismatch equations that must be solved when the generator is connected at node *k* is

$$\Delta P_k = -P_{k-gsc} - P_{dk} - P_k^{cal} \tag{3.33}$$

$$\Delta Q_k = -Q_{k-gsc} - Q_{dk} - Q_k^{cal} \tag{3.34}$$

$$\Delta P_{WT3,k} = P_G - P_{gsc-k} \tag{3.35}$$

$$\Delta Q_{WT3,k} = Q_G - Q_{gsc-k} \tag{3.36}$$

$$\begin{bmatrix} \Delta P_k \\ \Delta Q_k \\ \Delta P_{WT3,k} \\ \Delta Q_{WT3,k} \end{bmatrix}^i = \begin{bmatrix} \dfrac{\partial P_k^{cal}}{\partial \theta_k} + \dfrac{\partial P_{k-gsc}}{\partial \theta_k} & \left(\dfrac{\partial P_k^{cal}}{\partial V_k} + \dfrac{\partial P_{k-gsc}}{\partial V_k} \right) V_k & \dfrac{\partial P_{k-gsc}}{\partial \delta_{gsc}} & \dfrac{\partial P_{k-gsc}}{\partial V_{gsc}} V_{gsc} & 0 \\ \dfrac{\partial Q_k^{cal}}{\partial \theta_k} + \dfrac{\partial Q_{k-gsc}}{\partial \theta_k} & \left(\dfrac{\partial Q_k^{cal}}{\partial V_k} + \dfrac{\partial Q_{k-gsc}}{\partial V_k} \right) V_k & \dfrac{\partial Q_{k-gsc}}{\partial \delta_{gsc}} & \dfrac{\partial Q_{k-gsc}}{\partial V_{gsc}} V_{gsc} & 0 \\ \dfrac{\partial P_{gsc-k}}{\partial \theta_k} & \dfrac{\partial P_{gsc-k}}{\partial V_k} V_k & \dfrac{\partial P_{gsc-k}}{\partial \delta_{gsc}} & \dfrac{\partial P_{gsc-k}}{\partial V_{gsc}} V_{gsc} & -\dfrac{\partial P_G}{\partial \Delta f} \\ \dfrac{\partial Q_{gsc-k}}{\partial \theta_k} & \dfrac{\partial Q_{gsc-k}}{\partial V_k} V_k & \dfrac{\partial Q_{gsc-k}}{\partial \delta_{gsc}} & \dfrac{\partial Q_{gsc-k}}{\partial V_{gsc}} V_{gsc} & 0 \end{bmatrix}^i \begin{bmatrix} \Delta \theta_k \\ \dfrac{\Delta V_k}{V_k} \\ \Delta \delta_{gsc} \\ \dfrac{\Delta V_{gsc}}{V_{gsc}} \\ \Delta \Delta f \end{bmatrix}^i . \tag{3.37}$$

(b) Constant voltage magnitude control mode

Under this control strategy, the nodal voltage magnitude at the transformer's high-voltage side is maintained at a constant value by adjusting the generator's reactive power. In this case, the initial output of active power is computed using (3.31) and (3.32). The NR-based power flow formulation for this control strategy is thus given by

$$\Delta P_k = -P_{k-gsc} - P_{dk} - P_k^{cal} \tag{3.38}$$

$$\Delta Q_k = -Q_{k-gsc} - Q_{dk} - Q_k^{cal} \tag{3.39}$$

$$\Delta P_{WT3,k} = P_G - P_{gsc-k} \tag{3.40}$$

$$\begin{bmatrix} \Delta P_k \\ \Delta Q_k \\ \Delta P_{WT3,k} \end{bmatrix}^i = \begin{bmatrix} \frac{\partial P_k^{cal}}{\partial \theta_k} + \frac{\partial P_{k-gsc}}{\partial \theta_k} & \frac{\partial P_{k-gsc}}{\partial V_{gsc}} V_{gsc} & \frac{\partial P_{k-gsc}}{\partial \delta_{gsc}} & 0 \\ \frac{\partial Q_k^{cal}}{\partial \theta_k} + \frac{\partial Q_{k-gsc}}{\partial \theta_k} & \frac{\partial Q_{k-gsc}}{\partial V_{gsc}} V_{gsc} & \frac{\partial Q_{k-gsc}}{\partial \delta_{gsc}} & 0 \\ \frac{\partial P_{gsc-k}}{\partial \theta_k} & \frac{\partial P_{gsc-k}}{\partial V_{gsc}} V_{gsc} & \frac{\partial P_{gsc-k}}{\partial \delta_{gsc}} & -\frac{\partial P_G}{\partial \Delta f} \end{bmatrix}^i \begin{bmatrix} \Delta \theta_k \\ \frac{\Delta V_{gsc}}{V_{gsc}} \\ \Delta \delta_{gsc} \\ \Delta \Delta f \end{bmatrix}^i . \tag{3.41}$$

If the generator cannot provide the reactive power support to constrain its terminal voltage magnitude at the specified value, then the reactive power is fixed at the offending limit. In this case, the control strategy is changed to operate with a fixed power factor.

3.5 Initialization of wind generators

When solving power flows by using Newton's method, adequate initial conditions must be specified in order to achieve efficient iterative solutions. In this context, the proposals to initialize the wind generator state variables are stated below.

A good initial value of ω_m to execute power flow studies with a network having FP-FSWGs and PR-FSWGs is given by $\omega_m^{(0)} = \omega_{m\_nom}$, since the operating point of these generators is normally found close to the nominal mechanical angular speed.

The adopted strategy control must be considered first when initializing VSWGs. If a constant power factor is specified, then the reactive power is computed using the initial active power obtained from the power curve and is kept constant during the iterative process. On the other hand, if a constant voltage magnitude is selected, the output reactive power is calculated within the iterative process. In addition, the voltage magnitudes are initialized at 1 p.u. at all uncontrolled voltage magnitude nodes, while the controlled *PV* nodes are initialized at specified values that remain constant throughout the iterative solution if no generator reactive power limits are violated. The initial voltage phase angles are selected to be 0 at all buses.

3.6 Conclusions

This chapter has put forward mathematical models of various kinds of wind generators with frequency deviation-dependency. It should be remarked that these are steady-state models and yet they are able to take into account the effect of automatic load-frequency control devices. In this formulation, the system frequency deviation is taken to be a state variable which is computed by iteration with the other state variables of the power system using the Newton-Raphson method. This helps to identify the operating points of wind generators, following the action of the primary frequency controls in response to power imbalances in the power system.

The model formulation of the fixed-speed wind generators is based on the equivalent circuit of the induction machine. The overall modeling concept of system frequency deviations applied to FSWGs, has been extended to the case of VSWGs since their potential contribution to frequency support can be also analyzed with this modeling approach. It should be remarked that all the various models of wind generators with frequency deviation-dependency put forward in this chapter have been formulated to fit into a unified frame-of-reference which makes up for efficient iterative solutions and facilitates the estimation of the wind generators' responses following the action of the primary frequency regulation.

Chapter 4

DFIG MODEL FOR POWER SYSTEM SIMULATIONS

4.1 Introduction

The doubly-fed induction generator (DFIG) is at present time, the most popular technology for electrical energy extraction from the wind. One of the main advantages of the DFIG-VSWG is its advanced dynamic behaviour brought about by the recent developments in the power electronics and control strategies, i.e., improved reactive power and active power control capabilities with variable speed operation. Its upgraded mechanisms for capturing wind energy in an optimal manner and with less investment in power converters than the newer wind generator technology using full-rated converters, makes DFIG the technology of choice for wind farm owners, a fact that is reflected in the global wind energy market. Perhaps within the main drawbacks of the DFIG-VSWG technology compared to the fully-rated converters VSWG technology are: (i) the use of a gearbox which leads to noise and heat dissipation from friction, (ii) the direct grid connection of its stator causes that during network disturbance conditions large stator currents be produced, which in turns may cause high torque loads on the wind turbine's drive train [Li and Chen, 2008].

Figure 4.1 shows the schematic diagram of a DFIG. This wind generator may be subdivided into three major components: the wind turbine, the WRIG and the B-B converter. The turbine converts the kinetic energy from the wind into mechanical energy, which in turns is converted into electrical energy by the action of the induction generator. The power electronic converter is responsible for controlling the generator's mechanical torque as well as for providing reactive power support to the network. In contrast to current practice on DFIG modelling, the model presented in this chapter advances the level of detail with which the back-to-back converter is assembled, yielding new insight and information of key essential parameters. It combines seamlessly with the rest of the components making up the enhanced DFIG-based wind generator.

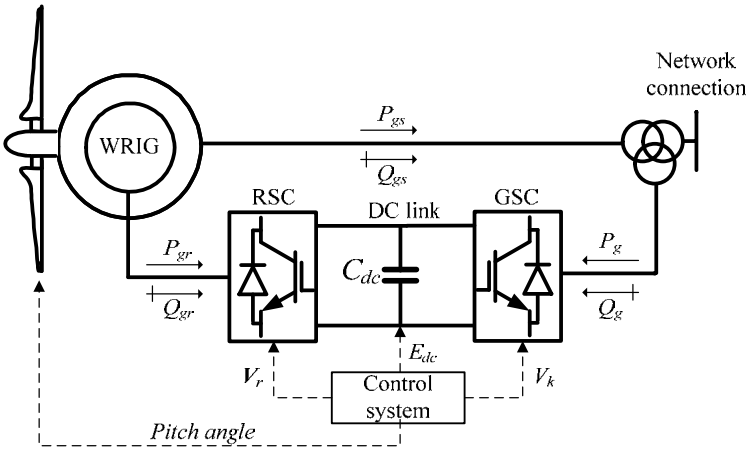

Figure 4.1: Schematic diagram of a DFIG

The following sections deal with the mathematical modeling of the various components which are combined to obtain a comprehensive DFIG model for steady-state and time-domain simulations using a unified frame of reference for efficient iterative solutions.

4.2 Frame of reference for computing dynamic power system simulations

Dynamic analysis yields the required information to determine the operating performance of a power system during a disturbance. The power system is very rich in dynamics, encompassing the very fast dynamics caused by atmospheric discharges and switching transients, the electromechanical oscillations of various kinds and the long-term dynamics originated from boiler and turbine controls, etc. [Cate and Gelopulos, 1984]. Hence, in power systems studies developing models of varying degrees of representation to target the phenomena of interest is normal.

In this work the interest is in assessing the dynamic behavior of the newly developed DFIG model in what we may consider as mid-term dynamics[Cate and Gelopulos, 1984], following a network topology change such as the tripping of a transmission line or transformer or simply a change in system load. To this end, the solution method presented in [Rafian et al., 1987] is selected to implement the DFIG model. This approach allows one to combine the set of algebraic equations (4.1) representing the network with the system of differential equations (4.2) describing the dynamic behavior of the machines and their controls, to obtain the solution as a function of time in a unified frame of reference. It makes use of the implicit trapezoidal method (as seen in Appendix C) which is known to be numerically stable, preserving reasonable accuracy, even when the time constants are much smaller than the integration time step [Rafian et al., 1987], [Dommel and Sato, 1972]:

$$0 = g\left(\mathbf{X}, \mathbf{Y}\right) \tag{4.1}$$

$$\dot{y} = f\left(\mathbf{X}, \mathbf{Y}\right), \tag{4.2}$$

where **X** and **Y** are vectors of variables that are computed at discrete points in time.

These equations are efficiently solved using the NR method which possesses strong convergence characteristics. In this case, the conventional power flows' Jacobian matrix, ***J***, is enlarged to accommodate the partial derivatives that arise from the discretized differential equations and their control variables. The NR method provides an accurate solution to the set of equations given by $f(\boldsymbol{Z})=0$, by solving for $\Delta\boldsymbol{Z}$ in the linearized problem $\boldsymbol{J}\,\Delta\boldsymbol{Z} = -\,f(\boldsymbol{Z})$ in a repetitive manner. In this case ***Z*** is a vector that contains the state variables that emerge from the network, synchronous generators and their controls or any other control device. In an expanded form,

$$\begin{bmatrix} \Delta P \\ \Delta Q \\ \hline \Delta F(y) \end{bmatrix}^i = -\left[\begin{array}{cc:c} \dfrac{\partial \Delta P}{\partial \theta} & \dfrac{\partial \Delta P}{\partial V} & \dfrac{\partial \Delta P}{\partial y} \\ \dfrac{\partial \Delta Q}{\partial \theta} & \dfrac{\partial \Delta Q}{\partial V} & \dfrac{\partial \Delta Q}{\partial y} \\ \hdashline \dfrac{\partial F(y)}{\partial \theta} & \dfrac{\partial F(y)}{\partial V} & \dfrac{\partial F(y)}{\partial y} \end{array}\right]^i \begin{bmatrix} \Delta\theta \\ \Delta V \\ \hline \Delta y \end{bmatrix}^i \tag{4.3}$$

where ΔP and ΔQ are the active and the reactive power mismatch vectors, respectively, $F(y)$ is a vector that contains the differential-algebraic equations (DAEs) of each machine or controlling device, and $\Delta\theta$, ΔV and Δy represent the vectors of incremental changes in nodal voltage angles and magnitudes, as well as the control variables arising from each differential equation. As in any NR method, the algorithm starts from an initial guess for $\boldsymbol{Z}_0$ and updates the solution at each iteration i, i.e. $\boldsymbol{Z}_{i+1} = \boldsymbol{Z}_i + \Delta\boldsymbol{Z}_i$, until a predefined tolerance is fulfilled. Hence, all of the state variables are adjusted simultaneously in order to compute the new equilibrium point of the power system at every time step.

This formulation is very advantageous from the numerical standpoint; the following sections show the mathematical model of the DFIG along with its components and controls with the aim of being numerically solved with this unified frame of reference.

4.3 Wind turbine modeling and its associated dynamic controls

The mechanical power extracted from the wind depends mainly on the wind speed, the swept area by the rotor blades and its aerodynamic power coefficient C_p, among other variables. For the sake of convenience, its equation is rewritten in this section:

$$P_m = \frac{1}{2}\rho C_p A V_w^3 \tag{4.4}$$

where

$$C_p = c_1\left(\frac{c_2}{\lambda_i} - c_3\beta - c_4\beta^{c_5} - c_6\right)\cdot e^{\frac{-c_7}{\lambda_i}} \tag{4.5}$$

$$\lambda_i = \left[\left(\frac{1}{\lambda + c_8\cdot\beta}\right) - \left(\frac{c_9}{\beta^3 + 1}\right)\right]^{-1} \tag{4.6}$$

$$\lambda = \frac{R_b\cdot\omega_r}{V_w} = \frac{R_b\cdot n_{gb}\cdot\omega_m}{V_w}. \tag{4.7}$$

In order to prevent mechanical stress in the rotor shaft when the wind speed surpasses the rated speed for which the wind turbine was constructed, the mechanical power must be reduced. To this end, a mechanical control which acts over the blade-pitch angle β is used, where this pitch control system ensures that the power is kept at its nominal value, P_{nom}. The changes in β occur, however, in the order of the 3-10 degrees per second according to the size of the turbine [Ackerman, 2005]. In this work, the pitch-angle controller monitors the electrical power output of the DFIG, P_e, and compares it with P_{nom}. The resultant difference is processed by a *PI* controller to produce a pitch angle reference value β^{ref} which in turn is used by the pitch-angle actuator to regulate β with the aim of bringing back the output power within limits, as shown in Figure 4.2 [Merabet et al., 2011].

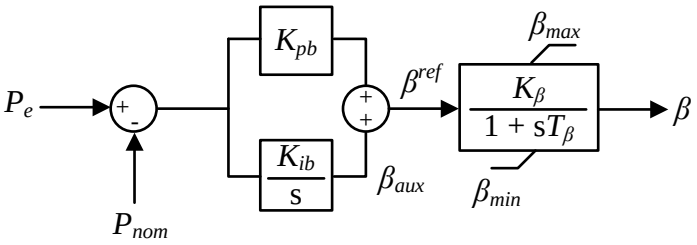

Figure 4.2: Blade-pitch angle controller

The equations arising from the control loops corresponding to the pitch-angle controller are,

$$\frac{d\beta_{aux}}{dt} = K_{ib}\left(P_e - P_{nom}\right) \tag{4.8}$$

$$\beta^{ref} = K_{pb}\left(P_e - P_{nom}\right) + \beta_{aux} \tag{4.9}$$

$$\frac{d\beta}{dt} = \frac{K_\beta \beta^{ref} - \beta}{T_\beta} \ . \tag{4.10}$$

We remind the reader that this controller is only active in situations when the active power generated by the DFIG overpasses its nominal power.

If the power coefficient is plotted versus the wind speed, one can observe from (4.7) that for every wind speed there is an optimal value of the tip-speed ratio λ, that is, an optimal value of the mechanical speed. In order to then reach a maximum power extraction for a given wind speed, the wind generator control system has to ensure that the DFIG is operating at its optimum rotational speed, $\omega_{m,opt}$. The control responsible to that end is termed maximum power tracking (MPT). Contrary to the pitch angle mechanism which is only active in the power limitation strategy, the MPT controller operates in both the power optimization and power limitation strategy.

In real practice, this optimal reference power curve is created according to the off-line experimental field tests and loaded in the memory of a microcontroller, thus working as a look-up table [Zou et al., 2011] which in turn is imposed in the DFIG during dynamic changes. For the purpose of this research, the look-up table is obtained by connecting the optimal operating points of the turbine where the resulting fitting curve is used as the MPT controller, as shown in Figure 4.3. Once the characteristic $P_{m,opt}$ vs $\omega_{m,opt}$ has been determined according to the parameters given for a particular wind turbine, it is employed to define a mechanical reference torque $T_{m,ref} = P_{m,opt} / \omega_{m,opt}$. Note that this controller is designed for generating the reference values for a wide range of wind speeds; the MPT controller then obliges the wind generator to operate at its maximum power for different mechanical rotor speeds [Price and Sanchez-Gasca, 2006].

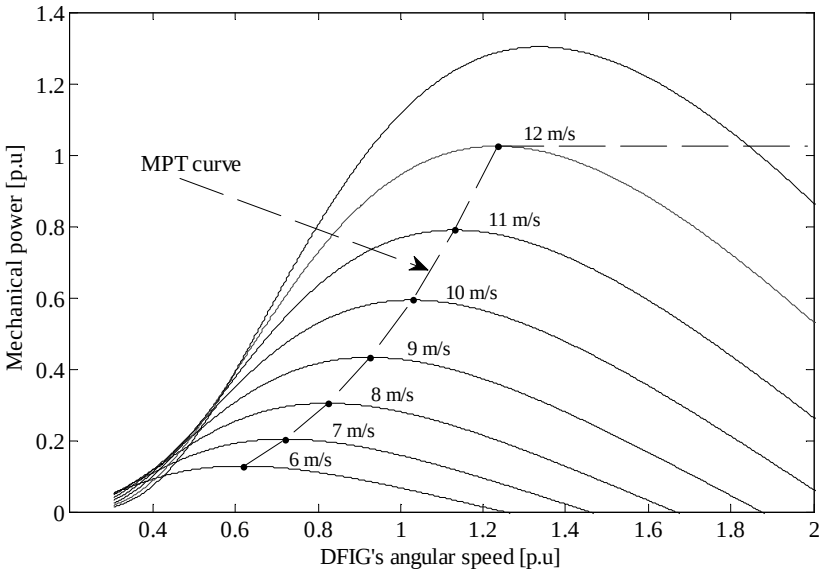

Figure 4.3: Curve for maximum power extraction, MPT.

4.4 Wound-rotor induction generator dynamic model

The wound-rotor induction generator has slip rings in its axis so the windings can be externally accessed. A three-phase WRIG then carries alternating currents in both the stator and rotor windings. The voltage equations governing the dynamic behavior of the DFIG are obtained by applying the fundamental Kirchhoff's and Faraday's laws as well as the Park transformation [Krause et al., 2002], [Kundur, 1994]:

$$v_{ds} = R_s i_{ds} - \omega_s \psi_{qs} + \frac{1}{\omega_b}\frac{d\psi_{ds}}{dt} \tag{4.11}$$

$$v_{qs} = R_s i_{qs} + \omega_s \psi_{ds} + \frac{1}{\omega_b}\frac{d\psi_{qs}}{dt} \tag{4.12}$$

$$v_{dr} = R_r i_{dr} - (\omega_s - \omega_m)\psi_{qr} + \frac{1}{\omega_b}\frac{d\psi_{dr}}{dt} \tag{4.13}$$

$$v_{qr} = R_r i_{qr} + (\omega_s - \omega_m)\psi_{dr} + \frac{1}{\omega_b}\frac{d\psi_{qr}}{dt} \tag{4.14}$$

where v is voltage, i is current, R is resistance, ψ represents the flux linkage, ω_s is the electrical rotating sped of the stator, ω_m is the mechanical speed of the generator rotor, ω_b is the base angular speed used to calculate the inductive reactances [rad/s], the subscripts d y q stand for the direct and quadrature axes, respectively, and the subscripts s y r represent

quantities corresponding to the stator and rotor, respectively. All of the above quantities are given in p.u. unless otherwise stated.

The stator and rotor flux linkages are expressed in the *dq* reference frame as follows:

$$\psi_{ds} = L_{ss} i_{ds} + L_m i_{dr} \tag{4.15}$$

$$\psi_{qs} = L_{ss} i_{qs} + L_m i_{qr} \tag{4.16}$$

$$\psi_{dr} = L_{rr} i_{dr} + L_m i_{ds} \tag{4.17}$$

$$\psi_{qr} = L_{rr} i_{qr} + L_m i_{qs} \ , \tag{4.18}$$

where $L_{ss} = L_{s\sigma} + L_m$ and $L_{rr} = L_{r\sigma} + L_m$. The subscripts *m* and σ stand for the mutual and leakage inductances, respectively.

On the other hand, the active and reactive powers generated by the stator and rotor are computed as follows:

$$P_{gs} = -\left(v_{ds} i_{ds} + v_{qs} i_{qs}\right) \tag{4.19}$$

$$Q_{gs} = -\left(v_{qs} i_{ds} - v_{ds} i_{qs}\right) \tag{4.20}$$

$$P_{gr} = -\left(v_{dr} i_{dr} + v_{qr} i_{qr}\right) \tag{4.21}$$

$$Q_{gr} = -\left(v_{qr} i_{dr} - v_{dr} i_{qr}\right) \tag{4.22}$$

Hence, the total active and reactive powers generated by the DFIG, and its developed electromagnetic torque are

$$P_e = P_{gs} + P_{gr} \tag{4.23}$$

$$Q_e = Q_{gs} + Q_{gr} \tag{4.24}$$

$$T_e = \psi_{ds} i_{qs} - \psi_{qs} i_{ds} \ . \tag{4.25}$$

It is worth mentioning that the total generated rotor powers are not directly injected to the grid. This is so because of the B-B converter interfacing between the rotor's circuit and the network's node where the DFIG is connected.

Some assumptions are commonly adopted regarding the implementation of the WRIG for transient stability studies in power systems: (i) the stator transients represented by the flux derivatives in (4.11) and (4.12) are neglected, i.e., $\dot{\psi}_{ds} = \dot{\psi}_{qs} = 0$, (ii) the reference frame rotates at the nominal synchronous speed, ω_b, and (iii) magnetic saturation is neglected. Hence, a WRIG dynamic model of order III can be obtained for the purpose of software simulations after some algebraic manipulations (as seen in Appendix C):

$$T_0' \frac{de_d'}{dt} = \omega_s L_m i_{qr} + \frac{(\omega_s - \omega_m) L_r}{R_r} e_q' - \frac{\omega_s L_m}{R_r} v_{qr} \tag{4.26}$$

$$T_0' \frac{de_q'}{dt} = -\omega_s L_m i_{dr} - \frac{(\omega_s - \omega_m) L_r}{R_r} e_d' + \frac{\omega_s L_m}{R_r} v_{dr} \tag{4.27}$$

$$\frac{d\omega_m}{dt} = \frac{T_e - T_m}{2H}. \tag{4.28}$$

where the equation (4.28) represents the motion equation of the DFIG and ω_m [p.u.] is the angular speed of the lumped mechanical system (turbine and generator), T_m [p.u.] is the mechanical torque and H [s] is the total inertia of the rotating mass, T'_0 is the transient open-circuit time constant [s], e_d' and e_q' are the per-unit e.m.f behind the transient reactance.

In addition, developing the WRIG's powers and electromagnetic torque in terms of the electrical network's variables is required to attain a correspondence between the grid and the DFIG. To this end, the equations (4.19) to (4.22) and (4.25) are now expressed in terms of meaningful variables as follows (as seen in Appendix C):

$$P_{gs} = V_k \frac{R_s \left(V_k + e_d' \sin(\theta_k - \theta_e) - e_q' \cos(\theta_k - \theta_e)\right) + X' \left(e_d' \cos(\theta_k - \theta_e) + e_q' \sin(\theta_k - \theta_e)\right)}{R_s{}^2 + X'^2} \tag{4.29}$$

$$Q_{gs} = V_k \frac{-R_s \left(e_d' \cos(\theta_k - \theta_e) + e_q' \sin(\theta_k - \theta_e)\right) + X' \left(V_k + \sin(\theta_k - \theta_e) e_d' - \cos(\theta_k - \theta_e) e_q'\right)}{R_s{}^2 + X'^2} \tag{4.30}$$

$$\begin{aligned} P_{gr} = &-v_{qr} \left\{ \frac{e_d'}{\omega_s L_m} - \frac{L_m}{L_r} \left[\frac{R_s \left(e_q' - V_k \cos(\theta_k - \theta_e)\right) - X' \left(e_d' + V_k \sin(\theta_k - \theta_e)\right)}{\left(R_s{}^2 + X'^2\right)} \right] \right\} + \\ &v_{dr} \left\{ \frac{e_q'}{\omega_s L_m} + \frac{L_m}{L_r} \left[\frac{R_s \left(e_d' + V_k \sin(\theta_k - \theta_e)\right) + X' \left(e_q' - V_k \cos(\theta_k - \theta_e)\right)}{\left(R_s{}^2 + X'^2\right)} \right] \right\} \end{aligned} \tag{4.31}$$

$$Q_{gr} = v_{dr}\left\{\frac{e'_d}{\omega_s L_m} - \frac{L_m}{L_r}\left[\frac{R_s\left(e'_q - V_k\cos\left(\theta_k-\theta_e\right)\right) - X'\left(e'_d + V_k\sin\left(\theta_k-\theta_e\right)\right)}{\left(R_s{}^2 + X'^2\right)}\right]\right\} + v_{qr}\left\{\frac{e'_q}{\omega_s L_m} + \frac{L_m}{L_r}\left[\frac{R_s\left(e'_d + V_k\sin\left(\theta_k-\theta_e\right)\right) + X'\left(e'_q - V_k\cos\left(\theta_k-\theta_e\right)\right)}{\left(R_s{}^2 + X'^2\right)}\right]\right\} \quad (4.32)$$

$$T_e = \frac{-R_s\left(e'_d{}^2 + e'_q{}^2 + e'_d V_k\sin\left(\theta_k-\theta_e\right) - e'_q V_k\cos\left(\theta_k-\theta_e\right)\right) + X'V_k\left(e'_d\cos\left(\theta_k-\theta_e\right) + e'_q\sin\left(\theta_k-\theta_e\right)\right)}{\omega_s\left(R_s{}^2 + X'^2\right)} \quad (4.33)$$

4.5 Back-to-back converter model

As shown in Figure 4.1, the B-B converter comprises a RSC, a GSC and a DC link to interconnect both converters. The three-phase winding of the rotor is fed by the RSC whose main goal is to control the active power output of the DFIG by means of the rotor currents through the MPT controller, whereas the GSC is responsible for keeping the DC voltage at its nominal value and, at the same time, for exerting reactive power control at the DFIG's network connection. In this work, the GSC is assumed to be able to provide voltage control at its terminal by regulating the reactive power exchange with the network.

In the ensuing sections, the mathematical modeling of the B-B converter is presented. Initially, a general VSC steady-state model is put forward. The complete B-B converter model is then derived for both the steady-state and dynamic regimes aimed at its integration with the WRIG to make up the new comprehensive DFIG model for power system simulations.

4.5.1 Voltage source converter (VSC) steady-state model

Physically, the VSC is built as a two-level or a multilevel converter that uses an array of self-commutating power electronic switches driven by a PWM control. On its DC side, the VSC employs a capacitor bank of small rating with the sole aim of supporting and stabilizing the voltage at its DC bus to enable the converter operation. The converter keeps the capacitor charged to the required voltage level by making its output voltage lag the AC system voltage by a small angle [Hingorani and Gyugyi, 1999]. The DC capacitor of value C_{DC} is shown quite prominently in Figure 4.4. It should be remarked that C_{DC} is not responsible *per se* for the actual VAR generation process and certainly not at all for the VAR absorption process.

Instead the VAR generation/absorption process is carried out by the PWM control which shifts the voltage and current waveforms within the VSC to yield either a leading or lagging VAR operation to satisfy operational requirements. Such an electronic processing of the voltage and current waveforms may be well characterized, from the fundamental frequency representation viewpoint, by an equivalent susceptance which can be either capacitive or inductive to conform to operating conditions.

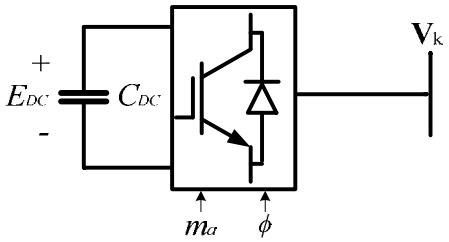

Figure 4.4: Schematic representation of a VSC

The VSC model, which can embody either the RSC or the GSC, comprises an ideal tap changing transformer with complex taps coupled to an impedance, an equivalent variable shunt susceptance B_{eq} placed on the right-hand side of the transformer and a resistor on its DC side, as seen in Figure 4.5. The series reactance X_{1v} represents the VSC's interface magnetics whereas the series resistor R_{1v} is associated with the conduction losses which are proportional to the AC terminal current squared. The shunt resistor (with a conductance value of G_{sw}) produces active power losses to account for the switching action of the PWM converter. This conductance is calculated according to the existing operating conditions and ensures that the switching losses be scaled by the quadratic ratio of the actual terminal current I_k to the nominal current I_{nom}:

$$G_{sw} = G_0 \left(\frac{I_k}{I_{nom}} \right)^2 . \tag{4.34}$$

The following assumptions are made in the model: (a) the complex voltage $\mathbf{V}_1 = m'_a e^{j\phi} E_{DC}$ is the voltage relative to the network's reference frame, (b) the tap magnitude m'_a of the ideal tap-changing transformer corresponds to the VSC's amplitude modulation coefficient where the following relationship holds for a two-level, three-phase VSC,

$m'_a = \sqrt{3}/2 \cdot m_a$, (c) the angle ϕ is the phase angle of voltage $\mathbf{V}_1$, and (d) E_{DC} is the DC bus amplitude voltage which is a real scalar and in a per-unit basis carries a value of $\sqrt{2}$.

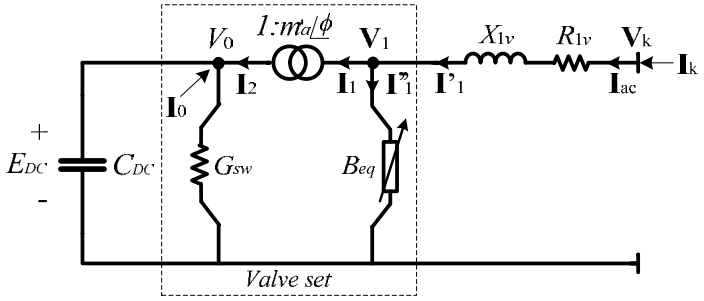

Figure 4.5: VSC equivalent circuit

The phase-shifting transformer composing the VSC model plays a crucial role in describing the converter operation; it decouples, angle-wise, the circuits connected at both ends of the transformer. Equally important is the fact that the phase angle of the nodal voltage on the left-hand side of the transformer keeps its initialization value. For the application pursued in this work, the phase angle of the bus 0 is fixed at zero; when looking at voltage $\mathbf{V_0}$ from the rectangular coordinates standpoint, its imaginary part does not exist [Acha and Kazemtabrizi, 2013]: if θ_0=0 then $\mathbf{V_0}$= V_0+j0= V_0.

In power system simulations, one generator node is assumed to be the slack bus where its phase angle gives the reference for the rest of the phase angles in the network. When considering the case, however, of a VSC the reference angle of the slack bus is not followed by the voltage at bus 0: this node would be inferred as the DC bus of the VSC given that its voltage is a real quantity.

This has two immediate consequences: from the AC power flow solution point of view, the phase angle of this node is an *a priori* known state variable, and the corresponding row and column may be deleted from the Jacobian equation, i.e., it does not need representation. The second consequence is that the AC-DC circuits brought about by the inclusion of one or more VSCs in the power network can be solved by using conventional AC power system applications, such as AC power flows. Bearing this in mind, the VSC nodal power flow equations are derived from the admittance matrix developed in Appendix C, as follows:

$$\begin{pmatrix}\mathbf{S}_k\\ \mathbf{S}_0\end{pmatrix}=\begin{pmatrix}\mathbf{V}_k & \\ & \mathrm{V}_0\end{pmatrix}\left\{\begin{pmatrix}\mathbf{Y}_1^* & -m_a'\angle-\phi\cdot\mathbf{Y}_1^*\\ -m_a'\angle\phi\cdot\mathbf{Y}_1^* & m_a'^2\left(\mathbf{Y}_1^*-\mathrm{j}B_{eq}\right)+G_{sw}\end{pmatrix}\begin{pmatrix}\mathbf{V}_k^*\\ \mathrm{V}_0\end{pmatrix}\right\} \tag{4.35}$$

After some arduous algebra, the expressions for the active and reactive powers of the VSC flowing from node *k* to 0, P_{ac} and Q_{ac}, as well as the powers flowing from node 0 to *k*, $P_{0'}$ and $Q_{0'}$, are reached:

$$P_{ac}=V_k^2G_1-m_a'V_kV_0\left[G_1\cos\left(\theta_k-\phi\right)+B_1\sin\left(\theta_k-\phi\right)\right] \tag{4.36}$$

$$Q_{ac}=-V_k^2B_1-m_a'V_kV_0\left[G_1\sin\left(\theta_k-\phi\right)-B_1\cos\left(\theta_k-\phi\right)\right] \tag{4.37}$$

$$P_{0'}=m_a'^2V_0^2G_1-m_a'V_kV_0\left[G_1\cos\left(\phi-\theta_k\right)+B_1\sin\left(\phi-\theta_k\right)\right] \tag{4.38}$$

$$Q_{0'}=-m_a'^2V_0^2B_1-m_a'V_kV_0\left[G_1\sin\left(\phi-\theta_k\right)-B_1\cos\left(\phi-\theta_k\right)\right]. \tag{4.39}$$

Note that in these last equations the voltage $\mathbf{V}_1$ does not play a role in calculating the powers in the VSC since it has been mathematically eliminated. Additionally, the nodal active and reactive powers for the shunt branches are expressed as follows:

$$P_{sw}=V_0^2G_0\left(\frac{I_k}{I_{nom}}\right)^2 \tag{4.40}$$

$$Q_{eq}=-m_a'^2V_0^2B_{eq} \tag{4.41}$$

with

$$I_k=\sqrt{\left(G_{1k}^2+B_{1k}^2\right)\left(V_k^2+m_a'^2V_0^2-2m_a'V_kV_0\cos\left(\theta_k-\phi\right)\right)}\ . \tag{4.42}$$

Hence, the set of mismatch power flow equations that must be solved to obtain the steady-state equilibrium point is

$$\Delta P_{ac}=-P_{ac}-P_{dk}-P_k^{cal} \tag{4.43}$$

$$\Delta Q_{ac}=-Q_{ac}-Q_{dk}-Q_k^{cal} \tag{4.44}$$

$$\Delta P_0=P_{0'}+P_{sw} \tag{4.45}$$

$$\Delta Q_0 = Q_{0'} + Q_{eq} \ , \tag{4.46}$$

where P_{dk} and Q_{dk} represent the active and reactive powers drawn by the load at bus k, respectively, and P_k^{cal} and Q_k^{cal} stand for the powers injected at bus k. They are given by

$$P_k^{cal} = V_k^2 G_{kk} + V_k \sum_{m \in k} V_m \left[G_{km} \cos\left(\theta_k - \theta_m\right) + B_{km} \sin\left(\theta_k - \theta_m\right) \right] \tag{4.47}$$

$$Q_k^{cal} = -V_k^2 B_{kk} + V_k \sum_{m \in k} V_m \left[G_{km} \sin\left(\theta_k - \theta_m\right) - B_{km} \cos\left(\theta_k - \theta_m\right) \right] \tag{4.48}$$

Since the objective is to regulate the voltage magnitude V_k within a specified value and, at the same time, to maintain V_0 at a constant value, the state variables (θ_k, m'_a, ϕ, B_{eq}) need to be found by solving (4.43) to (4.46). Furthermore, ensuring that the VSC operates in the linear range is necessary, say, m_a <1. Similarly, the total current magnitude I_k must be less than or equal to the nominal current I_{nom}.

4.5.2 Back-to-back converter steady-state model

If two VSC converters are linked as shown in Figure 4.6, a back-to-back converter is formed. In this arrangement, electric power is taken from the rotor circuit, converted to DC in the rectifier station, transmitted through the DC link, then converted back to AC in the inverter station and injected into the receiving AC network. In addition to transporting power in DC form, this combined system is also capable of providing independent dynamic voltage control at its two AC terminals. Note that the rectifier and inverter station can be equally the RSC or the GSC depending on the operating conditions of the DFIG: active power can flow in both directions, from the grid to the generator's rotor or vice versa, given that the induction generator can operate below or above the synchronous speed.

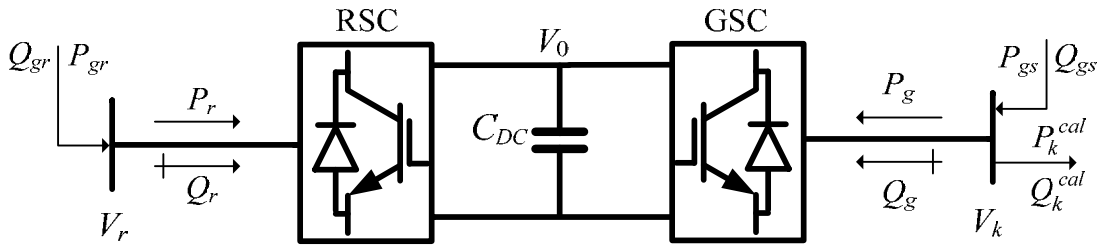

Figure 4.6: Schematic representation of the B-B converter used in the DFIG

Hence, assuming that the DFIG is connected at bus *k*, the set of mismatch equations to be solved iteratively to find the steady-state operating point of the B-B converter is

$$\Delta P_k = P_{gs} - P_g - P_{dk} - P_k^{cal} \tag{4.49}$$

$$\Delta Q_k = Q_{gs} - Q_g - Q_{dk} - Q_k^{cal} \tag{4.50}$$

$$\Delta P_r = P_{gr} - P_r \tag{4.51}$$

$$\Delta Q_r = Q_{gr} - Q_r \tag{4.52}$$

$$\Delta Q_{0r} = Q_{eqr} + Q_{0r} \tag{4.53}$$

$$\Delta Q_{0g} = Q_{eqg} + Q_{0g} \tag{4.54}$$

$$\Delta P_0 = P_{0r} + P_{swr} + P_{0g} + P_{swg} \ , \tag{4.55}$$

where P_{gs}, Q_{gs}, P_{gr}, and Q_{gr} are the active and reactive powers generated by the induction generator shown in (4.29) to (4.32). In addition, P_g, Q_g, P_r, and Q_r are the nodal power injections at the RSC's and GSC's terminals, respectively, and are computed as (4.56)-(4.59); P_{swr} and P_{swg} are the switching losses of the RSC and GSC, respectively, which are calculated similarly to (4.40). Finally, Q_{eqr} and Q_{eqg} stand for the reactive power generated/consumed by the equivalent susceptances B_{eqr} and B_{eqg}, respectively, and are calculated as in (4.41).

$$P_r = V_r^2 G_{1r} - m'_{ar} V_r V_0 \left[G_{1r} \cos\left(\theta_r - \phi_r\right) + B_{1r} \sin\left(\theta_r - \phi_r\right) \right] \tag{4.56}$$

$$Q_r = -V_r^2 B_{1r} - m'_{ar} V_r V_0 \left[G_{1r} \sin\left(\theta_r - \phi_r\right) - B_{1r} \cos\left(\theta_r - \phi_r\right) \right] \tag{4.57}$$

$$P_{0r} = m'^2_{ar} V_0^2 G_{1r} - m'_{ar} V_r V_0 \left[G_{1r} \cos\left(\phi_r - \theta_r\right) + B_{1r} \sin\left(\phi_r - \theta_r\right) \right] \tag{4.58}$$

$$Q_{0r} = -m'^2_{ar} V_0^2 B_{1r} - m'_{ar} V_r V_0 \left[G_{1r} \sin\left(\phi_r - \theta_r\right) - B_{1r} \cos\left(\phi_r - \theta_r\right) \right] \ . \tag{4.59}$$

Note that the previous equations and their state variables are expressed in the network's reference frame. The rotor voltage V_r and angle θ_r are then transformed from the network's reference frame into the *dq* reference frame for the sake of coherency as follows:

$$V_r = \sqrt{v_{dr}^2 + v_{qr}^2} \tag{4.60}$$

$$\theta_r = \arctan\left(\frac{V_{r,imag}}{V_{r,real}}\right) \tag{4.61}$$

$$\delta_r = \theta_e - \left(\omega_m \big/ \omega_s\right)\theta_k \tag{4.62}$$

$$\begin{bmatrix} V_{r,real} \\ V_{r,imag} \end{bmatrix} = \begin{bmatrix} \cos\delta_r & \sin\delta_r \\ \sin\delta_r & -\cos\delta_r \end{bmatrix} \begin{bmatrix} v_{qr} \\ v_{dr} \end{bmatrix}, \tag{4.63}$$

where δ_r represents the difference between the angular displacement θ_e of the synchronous rotating reference frame and the induction machine's rotor angle [Krause et al., 2002]. It is worth mentioning that this transformation is very convenient given that the rotor voltages in the *dq* reference frame are treated as state variables by the RSC controllers as seen in section 4.5.3.1.

A similar set of equations to that from (4.56) to (4.59) may be obtained for the powers injected at the GSC terminals by simply exchanging the subscripts *r* to *g*, bearing in mind that the node *g* would correspond to node *k* of the system: $V_k = V_g$ and $\theta_k = \theta_g$.

Given that the main goal of the B-B converter when coupled to the WRIG is to provide voltage control at DC bus, V_0, and at the network's node, V_k, then the state variables associated with such voltages are specified and kept constants for the steady state. For that reason, the set of state variables to be computed to find the steady-state operating point are θ_k, m'_{ag}, ϕ_r, m'_{ar}, B_{eqr}, B_{eqg}, ϕ_g. Note that the voltages at the rotor's terminals, v_{dr} and v_{qr}, do not appear in the set of variables given above. This is so because those state variables are calculated in accordance with the control strategy with which the DFIG is being operated, and that is implemented in the RSC dynamic controllers shown in section 4.5.3.1.

One salient point involves (4.55) which says that the power entering the RSC minus its power losses matches the power entering the GSC on the DC side: it guarantees the active power balance in the DC bus. Furthermore, in order to achieve realistic results, one must pay attention to the main limiting factor in power converter's operation, that is, the current passing through the electronic switches. One can then advantageously append to the developed set of equations, (4.49)-(4.55) the current control restriction which would be active in case the magnitude of the terminal current exceeds its nominal value I_{nom} at both VSCs. This is

$$\Delta I_{\lim} = I_{nom} - I_{rg} \tag{4.64}$$

where I_{rg} may represent the actual terminal current at either the RSC or the GSC terminals and is computed using (4.42).

Note that this formulation facilitates the calculation of the steady-state operating point of the B-B converter taking into account the power losses in the converters as well as its physical operating limits. Clearly, as in real operation of VSCs, the more current flowing through the electronic valves, the more active power losses are incurred in the converters.

4.5.3 Back-to-back converter dynamic model

The power converters that are employed by the DFIG are made up of two VSCs connected in a back-to-back arrangement with a capacitor located between them. The stator of the DFIG is connected directly to the network whereas the rotor circuit is interfaced with the grid through the B-B converter. This physical arrangement is intended for controlling, in an efficient manner, the rotor voltages as well as the network's voltage, thus modifying its dynamic behavior in the event of a disturbance in the grid. One way to achieve this is by decoupling the active power control from the reactive power control, where more often than not the analysis and implementation of the DFIG model are carried out in the *dq* reference frame [Pena et al., 1996]:

- Aligning the *q*-axis with the angular position of the stator voltage θ_k, the *d*-axis voltage is $v_{ds} = 0$ whilst the *q*-axis voltage equals the amplitude of the terminal voltage in the induction generator, $v_{qs} = V_k$, which is maintained constant by the GSC controller. Thus, if the active and reactive stator powers are given by (4.19) and (4.20), respectively, clearly the active power will be only a function of i_{qs} and the reactive power will only depend on i_{ds}: $P_{gs} = -V_k\, i_{qs}$ and $Q_{gs} = -V_k\, i_{ds}$.
- In addition, equations (4.15) and (4.16) show that the rotor currents are related to the stator currents. Therefore, through the adjustment of the rotor voltage, the desired rotor currents and hence the desired stator currents can be achieved. In turn, this will facilitate the acquisition of the corresponding stator currents that will enable the DFIG to operate at the optimum torque/power point as well as at the desired reactive power exchange at the stator's terminals whether to control the voltage or to operate at fixed power factor. This constitutes the base for the independent control of active power and reactive power in a DFIG-based wind generator [Lei et al., 2006].

4.5.3.1 Rotor side converter controller

In accordance with the assumptions previously discussed and ignoring the effect of the stator resistance, R_s = 0, in the dynamic behavior of the DFIG since it is much smaller than the stator reactance, the next active and reactive powers in the stator are then reached:

$$P_{gs} = \frac{-e'_d V_k}{X'} \tag{4.65}$$

$$Q_{gs} = \frac{-V_k{}^2 + V_k e'_q}{X'} \ . \tag{4.66}$$

The former equations prove further that P_{gs} and Q_{gs} can be controlled in a decoupled manner under the adopted assumptions. The active power is a function dependent on the *d*-axis e.m.f, e'_d, whereas the reactive power will depend merely on the *q*-axis e.m.f, e'_q.

By analyzing the equations governing the dynamic behavior for the DFIG presented in equations (4.26) and (4.27), one realizes that two control loops can be designed for controlling the induction machine. One where the active power/torque is controlled through the rotor voltage v_{qr} since this state variable plays an important role in the dynamic performance of e'_d. Similarly, equation (4.27) shows that the dynamic behavior of e'_q may be modified through altering the rotor voltage v_{dr}, thus controlling the reactive power Q_{gs}.

In accordance with equations (4.11)-(4.12) and bearing in mind that R_s = 0 and v_{ds} = 0, we have,

$$\psi_{qs} = 0 \tag{4.67}$$

$$V_k = \omega_s \psi_{ds} \ . \tag{4.68}$$

Because the stator is connected to the grid and the influence of R_s has been neglected, the magnetization current i_{ms} may be then considered constant:

$$\psi_{ds} = L_m i_{ms} \ . \tag{4.69}$$

By substituting (4.68) into (4.69), the following expression holds:

$$i_{ms} = \frac{V_k}{\omega_s L_m} \ . \tag{4.70}$$

Both the obtained expression for i_{ms} along with the reactive power strategy control serve to generate the reference *d*-axis current $i_{dr,ref}$, which consequently helps to produce the actual value of the rotor voltage v_{dr}. On the other hand, by knowing that the *q*-axis flux $\psi_{qs} = 0$ and solving (4.16) for i_{qs}, the following relationship is found

$$i_{qs} = -\frac{L_m}{L_{ss}} i_{qr} \quad . \tag{4.71}$$

By substituting (4.68) and (4.71) into the electromagnetic equation (4.25), we get

$$T_e = -\frac{V_k L_m}{\omega_s L_{ss}} i_{qr} \ . \tag{4.72}$$

This equation plays an important role in the design of the torque controller given that it is used to produce the reference *q*-axis current $i_{qr,ref}$ with which the voltage v_{qr} is generated, as shown in Figure 4.5.

By equating (4.16) and (4.69) and solving for i_{ds}, we have

$$i_{ds} = \frac{L_m \left(i_{ms} - i_{dr} \right)}{L_{ss}} \ . \tag{4.73}$$

Now, the stator current expressions (4.71) and (4.73) are used to find the rotor fluxes from (4.17) and (4.18) as

$$\psi_{dr} = \alpha i_{dr} + \left(L_{rr} - \alpha \right) i_{ms} \tag{4.74}$$

$$\psi_{qr} = \alpha i_{qr} \tag{4.75}$$

with

$$\alpha = \left(L_{rr} - \frac{L_m^2}{L_{ss}} \right) . \tag{4.76}$$

By substituting the above equations into (4.13) and (4.14), the rotor voltage equations are redefined as

$$\frac{\alpha}{\omega_b}\frac{di_{dr}}{dt} + R_r i_{dr} + v'_{dr} = v_{dr} \tag{4.77}$$

$$\frac{\alpha}{\omega_b}\frac{di_{qr}}{dt} + R_r i_{qr} + v'_{qr} = v_{qr} \tag{4.78}$$

where

$$v'_{dr} = -\alpha\left(\omega_s - \omega_m\right) i_{qr} \tag{4.79}$$

$$v'_{qr} = \left(\omega_s - \omega_m\right)\left[\alpha i_{dr} + \left(L_{rr} - \alpha\right) i_{ms}\right] . \tag{4.80}$$

In equations (4.77) and (4.78), it can be realized that through adequately controlling the *d*-axis rotor current i_{dr}, an appropriate *d*-axis rotor voltage v_{dr} may be obtained after adding the compensation term v'_{dr}. Likewise, the *q*-axis rotor voltage v_{qr} can be achieved by designing a controller for i_{qr} and adding to the actual value of v_{qr} the compensation term v'_{qr}. Indeed, this approach represents the decoupling technique that is carried out for controlling the DFIG by means of the RSC controller.

The overall RSC controllers are shown in Figures 4.7 and 4.8. In this work, the control loop that exerts voltage control in v_{dr} is intended for keeping a reference value of reactive power in the stator as $Q_{gs,ref} = P_{nom}\ tan(\varphi)$, where φ stands for the fixed power factor angle at which the stator is required to be operated during its dynamic performance. The primary stage of this controller provides the reference value of the *d*-axis rotor current $i_{dr,ref}$. As a second step, this reference value is compared with the actual value of the rotor current i_{dr}; the error is then processed by a PI controller, where its output signal serves to generate the final value of the rotor voltage v_{dr}. It should be brought to attention that the first stage of this controller slightly differs from the RSC controller used in recent publications such as [Anaya-Lara et al., 2009] and [Ugalde-Loo et al., 2013], where this controller is designed to inject reactive power to the grid via the stator's terminals in order to regulate the stator's voltage V_k.

In contrast, in this work the control of such voltage is performed via the GSC; this is to show the operating features of the newly develop VSC model representing the GSC.

On the other hand, the control loop shown in Figure 4.8 is responsible, generally speaking, for driving the DFIG to operate at the maximum power extraction point [Anaya-Lara et al., 2009], [Ugalde-Loo et al., 2013]. This controller regulates the rotor voltage v_{qr} in accordance with changes in the actual rotor speed ω_m. The first phase of this controller finds the optimum torque T_{ref} through the curve for maximum power extraction, that is, the MPT characteristic shown in Figure 4.3. Consequently, the reference value of q-axis rotor current $i_{qr,ref}$ is estimated and used to compare it with the actual value of the rotor current i_{qr}. After processing the error through a PI controller, its output signal allows to achieve the final value of the rotor voltage v_{qr}.

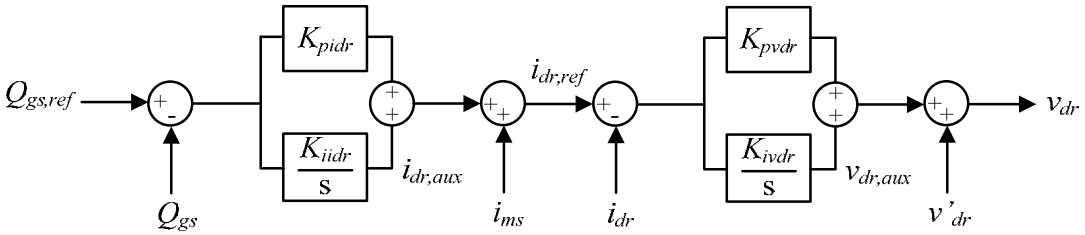

Figure 4.7: Control loop for reactive power control at stator's terminals.

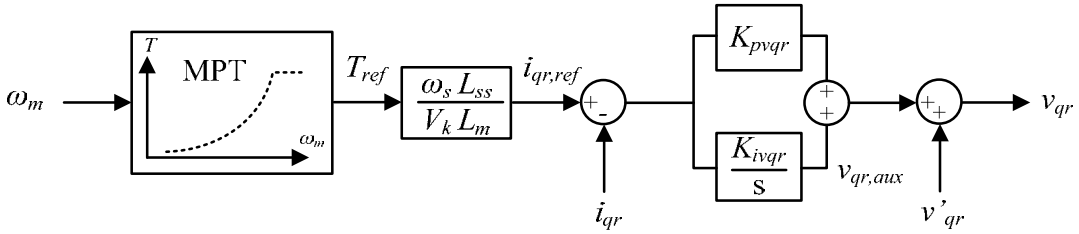

Figure 4.8: Control loop for maximum power extraction.

The equations arising from the control loop corresponding to the stator reactive power controller are

$$\frac{di_{dr,aux}}{dt} = K_{iidr}\left(Q_{gs,ref} - Q_{gs}\right) \tag{4.81}$$

$$i_{dr,ref} = K_{pidr}\left(Q_{gs,ref} - Q_{gs}\right) + i_{ms} + i_{dr,aux} \tag{4.82}$$

$$\frac{dv_{dr,aux}}{dt} = K_{ivdr}\left(i_{dr,ref} - i_{dr}\right) \tag{4.83}$$

$$v_{dr} = K_{pvdr}\left(i_{dr,ref} - i_{dr}\right) + v_{dr,aux} + v'_{dr} \ . \tag{4.84}$$

Similarly, the equations arising from the control loop related to the maximum power extraction in the DFIG are

$$\frac{dv_{qr,aux}}{dt} = K_{ivqr}\left(i_{qr,ref} - i_{qr}\right) \tag{4.85}$$

$$v_{qr} = K_{pvqr}\left(i_{qr,ref} - i_{qr}\right) + v_{qr,aux} + v'_{qr} \ . \tag{4.86}$$

4.5.3.2 DC-link dynamics and controller

In the steady-state regime, the voltage at the DC capacitor is kept constant at the value $V_{0,ref}$. Also, according to (4.87), clearly the current in the capacitor becomes zero given that the derivative of the voltage with respect to time is zero. When changes occur in the DC link, however, the capacitor goes through a charging/discharging stage, which is also reflected on its voltage:

$$i_c = C_{DC}\frac{dV_0}{dt}. \tag{4.87}$$

Therefore, the DC voltage dynamics are accurately captured if the dynamics in the DC capacitor are suitably represented when it is exposed to changes in the current flowing through it. Applying Kirchhoff's law to the DC circuit shown in Figure 4.9, the following relationship holds:

$$i_c = i_{dcr} - i_{dcg} \tag{4.88}$$

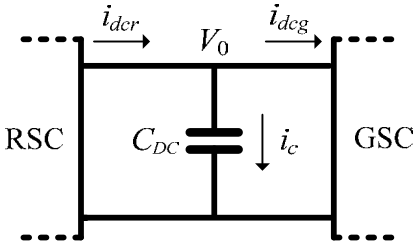

Figure 4.9: DC-link circuit.

By equating (4.87) and (4.88), we get

$$\frac{dV_0}{dt} = \frac{i_{dcr} - i_{dcg}}{C_{DC}} \ , \tag{4.89}$$

where i_{dcr} stands for the current leaving the RSC and i_{dcg} represents the current entering the GSC. Additionally, the current i_{dcr} can be computed as $i_{dcr} = -\frac{P_{0r} + P_{swr}}{V_0}$. By substituting this expression into (4.89), we arrive at the mathematical expression needed for properly calculating the DC-link voltage dynamics in the B-B converter:

$$\frac{dV_0}{dt} = \frac{1}{C_{DC}}\left(-\frac{P_{0r} + P_{swr}}{V_0} - i_{dcg} \right) . \tag{4.90}$$

Note that equation (4.90) may be thought of as the current balance inside the B-B converter, which undoubtedly is equivalent to the equation representing the power balance in (4.55) for steady-state operating conditions. Thus, whenever the current/power balance is broken, voltage variations will appear in the DC link. At this point, paying attention to the value of the capacitor C_{DC} is necessary as it plays a crucial role when attaining the DC voltage dynamics. In this work, its value is estimated according to the energy stored in the capacitor $W_c = ½\ C_{DC}\ (V_0)^2$. Arguably, the capacitor's energy storage bears a resemblance to the kinetic energy of rotating electrical machinery, where this energy can be further related to the inertia constant that impacts the machine's motion equation. Following the same reasoning, we can associate the *static energy stored* in the DC capacitor with an equivalent inertia constant H_c [s] as $W_c = H_c\ S_{nom}$, where S_{nom} would correspond to the rated apparent power of the B-B converter. This time constant may be taken to be $H_c = \omega_s^{-1}$ by drawing a parallel between the converter and a bank of thyristor-switched capacitors of the same rating [de Oliveira, 2000]. Hence, the per-unit value of the capacitor would be

$$C_{DC} = \frac{2 S_{nom} H_c}{V_0^2} \ . \tag{4.91}$$

As mentioned earlier in this chapter, the GSC is responsible for controlling the

voltage at the DC link regardless of the amount and direction of the rotor's active power. In the approach followed herein, the voltage control at the DC side of the B-B converters is performed via the proper control of the DC current entering or leaving the GSC, i_{dcg}. The implementation of the DC voltage controller is shown in Figure 4.10, in which the error between the actual voltage V_0 and $V_{0,ref}$ is processed through a PI controller to obtain the DC current i_{dcg}.

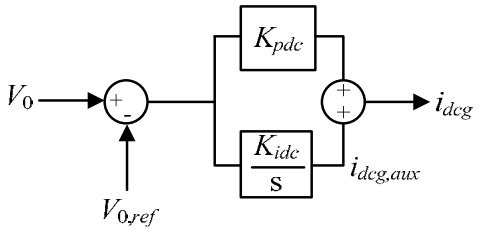

Figure 4.10: DC voltage controller.

The equations arising from the block diagram corresponding to the DC voltage controller are

$$\frac{di_{dcg,aux}}{dt} = K_{idc}\left(V_0 - V_{0,ref}\right) \tag{4.92}$$

$$i_{dcg} = K_{pdc}\left(V_0 - V_{0,ref}\right) + i_{dcg,aux} \ . \tag{4.93}$$

4.5.3.3 Grid-side converter controller

It would not be out of kilter to think of the GSC as a static synchronous compensator (STATCOM) from the reactive power support perspective owing to its direct connection to the grid. The modeling of the GSC aimed at time-domain simulations requires two basic control loops: one for the reactive current control and the other for the modulation index.

The control loop shown in Figure 4.11 is proposed with the aim of generating the necessary reactive current to modulate the voltage at the network's bus provided that it is between the physical limits of the VSC. During dynamic changes in the terminal voltage V_k, positive or negative variations will be produced for the reactive current $i_{reacg,aux}$. In this case, the current modulation is performed via a first-order control, which is blocked whenever the converter reaches either the maximum or minimum current, $I_{g,max/min}$.

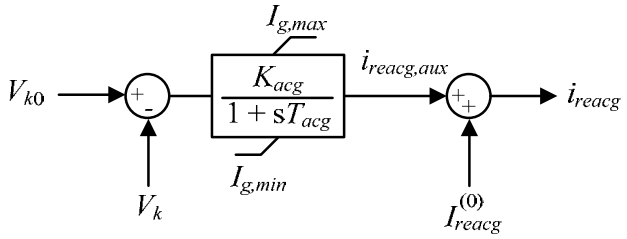

Figure 4.11: Reactive current control loop for the GSC.

In connection with Figure 4.11, we have to define the current $I_{reacg}^{(0)}$ as well to determine the current limits during dynamic changes; this is made as follows:

$$\frac{di_{reacg,aux}}{dt} = \frac{K_{acg}\left(V_{k0} - V_k\right) - i_{reacg,aux}}{T_{acg}} \tag{4.94}$$

$$i_{reacg} = i_{reacg,aux} + I_{reacg}^{(0)} \tag{4.95}$$

with

$$I_{reacg}^{(0)} = m_{ag}^{\prime(0)} V_{0,ref} B_{eqg}^{(0)} \tag{4.96}$$

$$I_{g,max/min} = \pm\sqrt{I_{nom}^2 - I_{realg}^2} \tag{4.97}$$

$$i_{realg} = \frac{i_{dcg} - P_{swg} \diagup V_0}{m_{ag}^{\prime}} \ , \tag{4.98}$$

where $m_{ag}^{\prime(0)}$, $V_{0,ref}$, $B_{eqg}^{(0)}$, V_{k0} are the steady-state values of the modulation index, DC voltage, equivalent susceptance and AC voltage at the network's node *k*, respectively. In addition, i_{realg} stands for the real current flowing on the AC side of the VSC (as seen in Figure 4.5) and is computed using equation (C.19) which appears in Appendix C. Note that in the event of a disturbance, the current i_{realg} will change as time passes, then the maximum/minimum reactive current $I_{g,max/min}$ must be updated every integration step using (4.97). For the sake of achieving realistic results, therefore, in case of incurring in a limit violation, the equation (4.94) shall be replaced by

$$\frac{di_{reacg,aux}}{dt} = \frac{K_{acg}\left(I_{g,max/min} - i_{reacg}\right) - i_{reacg,aux}}{T_{acg}} \quad . \tag{4.99}$$

The second GSC controller has been designed to provide additional support to the reactive current control loop via the adequate regulation of the modulation index m'_{ag}, as shown in Figure 4.12. This is so because when drastic changes in the DFIG's terminal voltage take place, the losses in the series branch on the VSC representing the GSC are increased. Counting on further support from the reactive power perspective standpoint is then beneficial. This control operates according to the changes of the angle $\delta_{gk} = \phi_g - \theta_k$, where δ_0 is the angle calculated after finding the steady-state operating conditions; it also takes into account the actual values of the reactive power injected at node k by the GSC and the terminal voltage of the DFIG, namely Q_{genk} and V_k, respectively. This controller is represented by three blocks. The first one produces the reference reactive power Q_{reg} after processing the error signal produced by comparing δ_{gk} and δ_0. In the second block the voltage signal V_{reg} is obtained by regulating the error between the GSC's reactive power output Q_{genk} and Q_{reg} with an integrator of gain K_{qm}. In the third block a new value of m'_{ag} is brought about by using the actual values of V_k and V_{reg}.

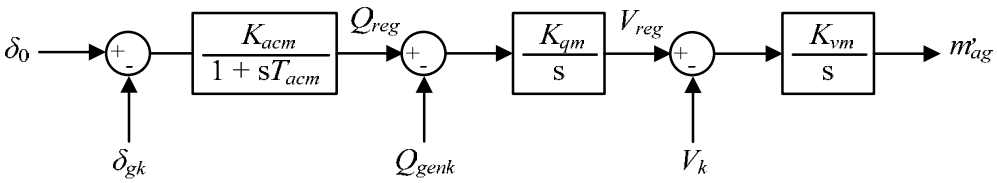

Figure 4.12: Modulation index control loop for the GSC.

The differential equations arising from this controller are

$$\frac{dQ_{reg}}{dt} = \frac{K_{acm}\left(\delta_0 - \delta_{gk}\right) - Q_{reg}}{T_{acm}} \tag{4.100}$$

$$\frac{dV_{reg}}{dt} = K_{qm}\left(Q_{reg} - Q_{genk}\right) \tag{4.101}$$

$$\frac{dm'_{ag}}{dt} = K_{vm}\left(V_{reg} - V_k\right) \; . \tag{4.102}$$

The overall dynamics of the DFIG's back-to-back converter are then captured using equations (4.81)-(4.86), (4.90), (4.92)-(4.95) and (4.100)-(4.102). Note that this new positive-sequence B-B converter dynamic model quite easily combines with the state variables that arise from WRIG's dynamic model. The following section shows in summary the proper way to include the comprehensive DFIG model: first in a power flow algorithm to compute the steady-state operating conditions of power systems with DFIGs, and secondly, the DFIG mathematical representation is formulated for time-domain simulations based on Newton's approach.

4.6 Complete DFIG model for steady-state and time-domain simulations

In this work, the newly developed DFIG model is aimed at steady-state and dynamic-state power system simulations. Its main assumptions rely on the following: (i) neglecting the electromagnetic transients in the stator of the induction generator, where such simplification is widely adopted in transient stability programs; (ii) assuming that the mechanical coupling between the turbine-generator is modeled as a lumped system; (iii) adding modeling flexibility to the B-B converter when it comes to representing its DC link, where the RSC and GSC are no longer represented as ideal voltage sources but as phase-shifting transformers each coupled to an equivalent variable shunt susceptance.

4.6.1 DFIG model for steady-state analysis

The in-depth steady-state DFIG model is essentially formulated starting from the algebraic and differential equations of the WRIG which are well combined with the rest of the equations arising from the power electronic converters, considering the control strategies implemented in modern DFIG-based wind turbines. Hence, the model is derived according to the following steps,

- Setting the time derivatives in (4.26)-(4.28) to zero.
- Recalling that the control loop for regulating the reactive power at stator's terminals imposes the WRIG to reach a fixed reference value $Q_{gs,ref}$.
- Driving the wind generator to operate at the optimal operating point for power extraction T_{ref}, which is obtained from the MPT characteristic.

The set of non-linear equations that must be solved to find the steady-state operating

conditions of a network containing DFIGs is then

$$\Delta P_k = P_{gs} - P_g - P_{dk} - P_k^{cal} \tag{4.103}$$

$$\Delta Q_k = Q_{gs} - Q_g - Q_{dk} - Q_k^{cal} \tag{4.104}$$

$$\Delta \chi_1 = \omega_s L_m i_{qr} + \frac{(\omega_s - \omega_m) L_r}{R_r} e'_q - \frac{\omega_s L_m}{R_r} v_{qr} \tag{4.105}$$

$$\Delta \chi_2 = -\omega_s L_m i_{dr} - \frac{(\omega_s - \omega_m) L_r}{R_r} e'_d + \frac{\omega_s L_m}{R_r} v_{dr} \tag{4.106}$$

$$\Delta T = T_{ref} - T_e \tag{4.107}$$

$$\Delta Q_{gs} = Q_{gs,ref} - Q_{gs} \tag{4.108}$$

$$\Delta P_r = P_{gr} - P_r \tag{4.109}$$

$$\Delta Q_r = Q_{gr} - Q_r \tag{4.110}$$

$$\Delta Q_{0r} = Q_{eqr} + Q_{0r} \tag{4.111}$$

$$\Delta Q_{0g} = Q_{eqg} + Q_{0g} \tag{4.112}$$

$$\Delta P_0 = P_{0r} + P_{swr} + P_{0g} + P_{swg} \tag{4.113}$$

Note that this thorough formulation does not omit a single component that takes part in the electrical operation of the DFIG. The first two equations represent the DFIG inclusion to any network at node *k*. The subsequent three equations are directly derived from the induction generator's dynamic model, whereas equation (4.108) comes from the reactive power control strategy. To end with, the last five equations permit the computation of the voltages and powers involved in the energy transmission from the rotor's circuit to the grid, highlighting that (4.113) may be thought of as the power balance equation in the DC link of the B-B converter.

Lastly, the matrix of partial derivatives J_{dfig}, shown in (4.114), results from the linearization of the above given set of equations. This equation is then used to compute the steady-state equilibrium point via a power flow solution, where the vector of state variables Δz does not include the voltages at the DC bus V_0 and at the network's node V_k since they are kept constant through the iterative process:

$$\Delta F^i = -J^i_{dfig}\,\Delta z^i \tag{4.114}$$

with

$$\Delta F = \begin{bmatrix} \Delta P_k & \Delta Q_k & \Delta \chi_1 & \Delta \chi_2 & \Delta T & \Delta Q_{gs} & \Delta P_r & \Delta Q_r & \Delta Q_{0r} & \Delta Q_{0g} & \Delta P_0 \end{bmatrix}^T \tag{4.115}$$

$$\Delta z = \begin{bmatrix} \Delta \theta_k & \Delta m'_{ag} & \Delta v_{dr} & \Delta v_{qr} & \Delta e'_d & \Delta e'_q & \Delta \phi_r & \Delta m'_{ar} & \Delta B_{eqr} & \Delta B_{eqg} & \Delta \phi_g \end{bmatrix}^T \tag{4.116}$$

$$J_{dfig} = \begin{bmatrix}
\frac{\partial \Delta P_k}{\partial \theta_k} & \frac{\partial \Delta P_k}{\partial m'_{ag}} & 0 & 0 & \frac{\partial \Delta P_k}{\partial e'_d} & \frac{\partial \Delta P_k}{\partial e'_q} & 0 & 0 & 0 & 0 & \frac{\partial \Delta P_k}{\partial \phi_g} \\
\frac{\partial \Delta Q_k}{\partial \theta_k} & \frac{\partial \Delta Q_k}{\partial m'_{ag}} & 0 & 0 & \frac{\partial \Delta Q_k}{\partial e'_d} & \frac{\partial \Delta Q_k}{\partial e'_q} & 0 & 0 & 0 & 0 & \frac{\partial \Delta Q_k}{\partial \phi_g} \\
\frac{\partial \Delta \chi_1}{\partial \theta_k} & 0 & 0 & \frac{\partial \Delta \chi_1}{\partial v_{qr}} & \frac{\partial \Delta \chi_1}{\partial e'_d} & \frac{\partial \Delta \chi_1}{\partial e'_q} & 0 & 0 & 0 & 0 & 0 \\
\frac{\partial \Delta \chi_2}{\partial \theta_k} & 0 & \frac{\partial \Delta \chi_2}{\partial v_{dr}} & 0 & \frac{\partial \Delta \chi_2}{\partial e'_d} & \frac{\partial \Delta \chi_2}{\partial e'_q} & 0 & 0 & 0 & 0 & 0 \\
\frac{\partial \Delta T}{\partial \theta_k} & 0 & 0 & 0 & \frac{\partial \Delta T}{\partial e'_d} & \frac{\partial \Delta T}{\partial e'_q} & 0 & 0 & 0 & 0 & 0 \\
\frac{\partial \Delta Q_{gs}}{\partial \theta_k} & 0 & 0 & 0 & \frac{\partial \Delta Q_{gs}}{\partial e'_d} & \frac{\partial \Delta Q_{gs}}{\partial e'_q} & 0 & 0 & 0 & 0 & 0 \\
\frac{\partial \Delta P_r}{\partial \theta_k} & 0 & \frac{\partial \Delta P_r}{\partial v_{dr}} & \frac{\partial \Delta P_r}{\partial v_{qr}} & \frac{\partial \Delta P_r}{\partial e'_d} & \frac{\partial \Delta P_r}{\partial e'_q} & \frac{\partial \Delta P_r}{\partial \phi_r} & \frac{\partial \Delta P_r}{\partial m'_{ar}} & 0 & 0 & 0 \\
\frac{\partial \Delta Q_r}{\partial \theta_k} & 0 & \frac{\partial \Delta Q_r}{\partial v_{dr}} & \frac{\partial \Delta Q_r}{\partial v_{qr}} & \frac{\partial \Delta Q_r}{\partial e'_d} & \frac{\partial \Delta Q_r}{\partial e'_q} & \frac{\partial \Delta Q_r}{\partial \phi_r} & \frac{\partial \Delta Q_r}{\partial m'_{ar}} & 0 & 0 & 0 \\
0 & 0 & \frac{\partial \Delta Q_{0r}}{\partial v_{dr}} & \frac{\partial \Delta Q_{0r}}{\partial v_{qr}} & 0 & 0 & \frac{\partial \Delta Q_{0r}}{\partial \phi_r} & \frac{\partial \Delta Q_{0r}}{\partial m'_{ar}} & \frac{\partial \Delta Q_{0r}}{\partial B_{eqr}} & 0 & 0 \\
\frac{\partial \Delta Q_{0g}}{\partial \theta_k} & \frac{\partial \Delta Q_{0g}}{\partial m'_{ag}} & 0 & 0 & 0 & 0 & 0 & 0 & 0 & \frac{\partial \Delta Q_{0g}}{\partial B_{eqg}} & \frac{\partial \Delta Q_{0g}}{\partial \phi_g} \\
\frac{\partial \Delta P_0}{\partial \theta_k} & \frac{\partial \Delta P_0}{\partial m'_{ag}} & \frac{\partial \Delta P_0}{\partial v_{dr}} & \frac{\partial \Delta P_0}{\partial v_{qr}} & 0 & 0 & \frac{\partial \Delta P_0}{\partial \phi_r} & \frac{\partial \Delta P_0}{\partial m'_{ar}} & 0 & 0 & \frac{\partial \Delta P_0}{\partial \phi_g}
\end{bmatrix} \tag{4.117}$$

Recall that in the case of a current limit violation in the GSC, expanding the set of mismatch equations (4.115) to include (4.64) is needed. The set of state variables (4.116) and the Jacobian matrix (4.117) must be, therefore, properly enlarged to incorporate V_k and the corresponding partial derivatives, respectively. Thus, the voltage at stator's terminals V_k becomes a new state variable which will be computed through the iterative process.

This formulation permits us to find the steady-state operating conditions of a power

system containing DFIGs with a wide variety of wind speed conditions. Furthermore, upon successful convergence of the power flow algorithm, the obtained solution is well suited to initialize transient stability type studies with no need for extra calculations given that the machine's active and reactive powers fully agree with its operating stator and rotor voltages as well as with its mechanical angular speed value.

4.6.2 DFIG model for dynamic analysis

Once the initial conditions of the DFIG model have been determined, time-domain simulations can be performed; however note that the dynamic controllers associated with the RSC, DC link and GSC are designed, to a greater or lesser extent, to regulate the currents i_{dr}, i_{qr}, i_{dcg} and i_{reacg}, respectively. This fact becomes rather convenient because it enables, in an easy way, to perform the current limit checking during the dynamic simulation. A slight reformulation of equations, however, needs to be made so as to take advantage of the use of currents as control variables. Hence, in contrast with the equations used for computing the power flows between the network and the DFIG, the equations (4.119)-(4.124) are used instead, where the reactive power injected by the GSC at bus *k* is now calculated as

$$Q_{genk} = -\left[Q_{eqg} + \left(i_{realg}^2 + i_{reacg}^2 \right) X_{1g} \right] \tag{4.118}$$

where i_{realg}^2 is computed using (4.98), and X_{1g} is the series reactance of the GSC.

The step-by-step numerical integration of the set of discretized algebraic equations, which emerge from the dynamic controllers, is required to perform dynamic simulations. Both the power flow equations and the DAEs can be solved simultaneously, in what could be termed a unified frame of reference approach. To this end, the resulting DAEs (4.125)-(4.138) are algebraically manipulated and expressed as mismatch equations (explained in Appendix C):

$$\Delta P_k = P_{gs} - P_g - P_{dk} - P_k^{cal} \tag{4.119}$$

$$\Delta Q_k = Q_{gs} - Q_{genk} - Q_{dk} - Q_k^{cal} \tag{4.120}$$

$$\Delta P_r = P_{gr} - P_r \tag{4.121}$$

$$\Delta Q_r = Q_{gr} - Q_r \tag{4.122}$$

$$\Delta Q_{0r} = Q_{eqr} + Q_{0r} \tag{4.123}$$

$$\Delta P_0 = P_{0g} + P_{swg} - V_0 i_{dcg} \tag{4.124}$$

$$F_{e'_d} = e'_{d(t-\Delta t)} + \frac{\Delta t}{2}\dot{e}'_{d(t-\Delta t)} - \left(e'_{d(t)} - \frac{\Delta t}{2}\dot{e}'_{d(t)} \right) \tag{4.125}$$

$$F_{e'_q} = e'_{q(t-\Delta t)} + \frac{\Delta t}{2}\dot{e}'_{q(t-\Delta t)} - \left(e'_{q(t)} - \frac{\Delta t}{2}\dot{e}'_{q(t)} \right) \tag{4.126}$$

$$F_{\omega_m} = \omega_{m(t-\Delta t)} + \frac{\Delta t}{2}\dot{\omega}_{m(t-\Delta t)} - \left(\omega_{m(t)} - \frac{\Delta t}{2}\dot{\omega}_{m(t)} \right) \tag{4.127}$$

$$F_{\beta_{aux}} = \beta_{aux(t-\Delta t)} + \frac{\Delta t}{2}\dot{\beta}_{aux(t-\Delta t)} - \left(\beta_{aux(t)} - \frac{\Delta t}{2}\dot{\beta}_{aux(t)} \right) \tag{4.128}$$

$$F_{\beta} = \beta_{(t-\Delta t)} + \frac{\Delta t}{2}\dot{\beta}_{(t-\Delta t)} - \left(\beta_{(t)} - \frac{\Delta t}{2}\dot{\beta}_{(t)} \right) \tag{4.129}$$

$$F_{i_{dr,aux}} = i_{dr,aux(t-\Delta t)} + \frac{\Delta t}{2}\dot{i}_{dr,aux(t-\Delta t)} - \left(i_{dr,aux(t)} - \frac{\Delta t}{2}\dot{i}_{dr,aux(t)} \right) \tag{4.130}$$

$$F_{v_{dr,aux}} = v_{dr,aux(t-\Delta t)} + \frac{\Delta t}{2}\dot{v}_{dr,aux(t-\Delta t)} - \left(v_{dr,aux(t)} - \frac{\Delta t}{2}\dot{v}_{dr,aux(t)} \right) \tag{4.131}$$

$$F_{v_{qr,aux}} = v_{qr,aux(t-\Delta t)} + \frac{\Delta t}{2}\dot{v}_{qr,aux(t-\Delta t)} - \left(v_{qr,aux(t)} - \frac{\Delta t}{2}\dot{v}_{qr,aux(t)} \right) \tag{4.132}$$

$$F_{V_0} = V_{0(t-\Delta t)} + \frac{\Delta t}{2}\dot{V}_{0(t-\Delta t)} - \left(V_{0(t)} - \frac{\Delta t}{2}\dot{V}_{0(t)} \right) \tag{4.133}$$

$$F_{i_{dcg,aux}} = i_{dcg,aux(t-\Delta t)} + \frac{\Delta t}{2}\dot{i}_{dcg,aux(t-\Delta t)} - \left(i_{dcg,aux(t)} - \frac{\Delta t}{2}\dot{i}_{dcg,aux(t)} \right) \tag{4.134}$$

$$F_{i_{reacg,aux}} = i_{reacg,aux(t-\Delta t)} + \frac{\Delta t}{2}\dot{i}_{reacg,aux(t-\Delta t)} - \left(i_{reacg,aux(t)} - \frac{\Delta t}{2}\dot{i}_{reacg,aux(t)} \right) \tag{4.135}$$

$$F_{Q_{reg}} = Q_{reg(t-\Delta t)} + \frac{\Delta t}{2}\dot{Q}_{reg(t-\Delta t)} - \left(Q_{reg(t)} - \frac{\Delta t}{2}\dot{Q}_{reg(t)} \right) \tag{4.136}$$

$$F_{V_{reg}} = V_{reg(t-\Delta t)} + \frac{\Delta t}{2}\dot{V}_{reg(t-\Delta t)} - \left(V_{reg(t)} - \frac{\Delta t}{2}\dot{V}_{reg(t)} \right) \tag{4.137}$$

$$F_{m'_{ag}} = m'_{ag(t-\Delta t)} + \frac{\Delta t}{2}\dot{m}'_{ag(t-\Delta t)} - \left(m'_{ag(t)} - \frac{\Delta t}{2}\dot{m}'_{ag(t)} \right) \tag{4.138}$$

The above expressions make up the set of mismatch equations that must be solved together with the equations of the whole network in every integration step, for reliable

dynamic simulations. The linearised form of the DFIG equations is

$$\Delta F^i = -\left[\begin{array}{c|c} J_{11} & J_{12} \\ \hline J_{21} & J_{22} \end{array}\right]^i \Delta z^i \tag{4.139}$$

with

$$\begin{aligned} \Delta F = \big[& \Delta P_k \quad \Delta Q_k \quad \Delta P_r \quad \Delta Q_r \quad \Delta Q_{0r} \quad \Delta P_0 \quad F_{e'_d} \quad F_{e'_q} \quad F_{\omega_m} \quad F_{\beta_{aux}} \quad F_{\beta} \ldots \\ & F_{i_{dr,aux}} \quad F_{v_{dr,aux}} \quad F_{v_{qr,aux}} \quad F_{V_0} \quad F_{i_{dcg,aux}} \quad F_{i_{reacg,aux}} \quad F_{Q_{reg}} \quad F_{V_{reg}} \quad F_{m'_{ag}} \big]^T \end{aligned} \tag{4.140}$$

$$\begin{aligned} \Delta z = \big[& \Delta\theta_k \quad \Delta V_k \quad \Delta\phi_r \quad \Delta m'_{ar} \quad \Delta B_{eqr} \quad \Delta\phi_g \quad \Delta e'_d \quad \Delta e'_q \quad \Delta\omega_m \quad \Delta\beta_{aux} \quad \Delta\beta \ldots \\ & \Delta i_{dr,aux} \quad \Delta v_{dr,aux} \quad \Delta v_{qr,aux} \quad \Delta V_0 \quad \Delta i_{dcg,aux} \quad \Delta i_{reacg,aux} \quad \Delta Q_{reg} \quad \Delta V_{reg} \quad \Delta m'_{ag} \big]^T , \end{aligned} \tag{4.141}$$

where J_{11}[6X6] comprises the first-order partial derivatives of the inner power flow equations of the DFIG with respect to their own state variables, as shown more explicitly in (4.142). Likewise, J_{12} [6X14] in (4.143) shows the partial derivatives arising from the DFIG's power flow equations with respect to the control variables corresponding to the DFIG's differential equations. The matrix J_{21} [14X6] consists of partial derivatives of the DFIG's DAEs with respect to the state variables associated with the DFIG's power flow equations, as shown in (4.144). On the other hand, J_{22} [14X14] is a matrix that accommodates the first-order partial derivatives of the DFIG's discretized differential equations with respect to their own control variables, as shown in (4.145).

$$J_{11}=\begin{bmatrix} \frac{\partial \Delta P_k}{\partial \theta_k} & \frac{\partial \Delta P_k}{\partial V_k} & 0 & 0 & 0 & \frac{\partial \Delta P_k}{\partial \phi_g} \\ \frac{\partial \Delta Q_k}{\partial \theta_k} & \frac{\partial \Delta Q_k}{\partial V_k} & 0 & 0 & 0 & \frac{\partial \Delta Q_k}{\partial \phi_g} \\ \frac{\partial \Delta P_r}{\partial \theta_k} & \frac{\partial \Delta P_r}{\partial V_k} & \frac{\partial \Delta P_r}{\partial \phi_r} & \frac{\partial \Delta P_r}{\partial m'_{ar}} & 0 & 0 \\ \frac{\partial \Delta Q_r}{\partial \theta_k} & \frac{\partial \Delta Q_r}{\partial V_k} & \frac{\partial \Delta Q_r}{\partial \phi_r} & \frac{\partial \Delta Q_r}{\partial m'_{ar}} & 0 & 0 \\ 0 & 0 & \frac{\partial \Delta Q_{0r}}{\partial \phi_r} & \frac{\partial \Delta Q_{0r}}{\partial m'_{ar}} & \frac{\partial \Delta Q_{0r}}{\partial B_{eqr}} & 0 \\ \frac{\partial \Delta P_0}{\partial \theta_k} & \frac{\partial \Delta P_0}{\partial V_k} & 0 & 0 & 0 & \frac{\partial \Delta P_0}{\partial \phi_g} \end{bmatrix} \tag{4.142}$$

$$J_{12}=\begin{bmatrix} \frac{\partial \Delta P_k}{\partial e'_d} & \frac{\partial \Delta P_k}{\partial e'_q} & 0 & 0 & 0 & 0 & 0 & 0 & \frac{\partial \Delta P_k}{\partial V_0} & 0 & 0 & 0 & 0 & \frac{\partial \Delta P_k}{\partial m'_{ag}} \\ \frac{\partial \Delta Q_k}{\partial e'_d} & \frac{\partial \Delta Q_k}{\partial e'_q} & 0 & 0 & 0 & 0 & 0 & 0 & \frac{\partial \Delta Q_k}{\partial V_0} & \frac{\partial \Delta Q_k}{\partial i_{dcg}} & \frac{\partial \Delta Q_k}{\partial i_{reacg}} & 0 & 0 & \frac{\partial \Delta Q_k}{\partial m'_{ag}} \\ \frac{\partial \Delta P_r}{\partial e'_d} & \frac{\partial \Delta P_r}{\partial e'_q} & 0 & 0 & 0 & 0 & \frac{\partial \Delta P_r}{\partial v_{dr}} & \frac{\partial \Delta P_r}{\partial v_{qr}} & \frac{\partial \Delta P_r}{\partial V_0} & 0 & 0 & 0 & 0 & 0 \\ \frac{\partial \Delta Q_r}{\partial e'_d} & \frac{\partial \Delta Q_r}{\partial e'_q} & 0 & 0 & 0 & 0 & \frac{\partial \Delta Q_r}{\partial v_{dr}} & \frac{\partial \Delta Q_r}{\partial v_{qr}} & \frac{\partial \Delta Q_r}{\partial V_0} & 0 & 0 & 0 & 0 & 0 \\ 0 & 0 & 0 & 0 & 0 & 0 & \frac{\partial \Delta Q_{0r}}{\partial v_{dr}} & \frac{\partial \Delta Q_{0r}}{\partial v_{qr}} & \frac{\partial \Delta Q_{0r}}{\partial V_0} & 0 & 0 & 0 & 0 & 0 \\ 0 & 0 & 0 & 0 & 0 & 0 & 0 & 0 & \frac{\partial \Delta P_0}{\partial V_0} & \frac{\partial \Delta P_0}{\partial i_{dcg}} & 0 & 0 & 0 & \frac{\partial \Delta P_0}{\partial m'_{ag}} \end{bmatrix} \tag{4.143}$$

$$J_{21}=\begin{bmatrix}
\frac{\partial F_{e'_d}}{\partial \theta_k} & \frac{\partial F_{e'_d}}{\partial V_k} & 0 & 0 & 0 & 0 \\
\frac{\partial F_{e'_q}}{\partial \theta_k} & \frac{\partial F_{e'_q}}{\partial V_k} & 0 & 0 & 0 & 0 \\
\frac{\partial F_{\omega_m}}{\partial \theta_k} & \frac{\partial F_{\omega_m}}{\partial V_k} & 0 & 0 & 0 & 0 \\
\frac{\partial F_{\beta_{aux}}}{\partial \theta_k} & \frac{\partial F_{\beta_{aux}}}{\partial V_k} & 0 & 0 & 0 & 0 \\
0 & 0 & 0 & 0 & 0 & 0 \\
\frac{\partial F_{i_{dr,aux}}}{\partial \theta_k} & \frac{\partial F_{i_{dr,aux}}}{\partial V_k} & 0 & 0 & 0 & 0 \\
\frac{\partial F_{v_{dr,aux}}}{\partial \theta_k} & \frac{\partial F_{v_{dr,aux}}}{\partial V_k} & 0 & 0 & 0 & 0 \\
\frac{\partial F_{v_{qr,aux}}}{\partial \theta_k} & \frac{\partial F_{v_{qr,aux}}}{\partial V_k} & 0 & 0 & 0 & 0 \\
0 & 0 & \frac{\partial F_{V_0}}{\partial \phi_r} & \frac{\partial F_{V_0}}{\partial m'_{ar}} & 0 & 0 \\
0 & 0 & 0 & 0 & 0 & 0 \\
0 & \frac{\partial F_{i_{reacg,aux}}}{\partial V_k} & 0 & 0 & 0 & 0 \\
\frac{\partial F_{Q_{reg}}}{\partial \theta_k} & 0 & 0 & 0 & 0 & \frac{\partial F_{Q_{reg}}}{\partial \phi_g} \\
\frac{\partial F_{V_{reg}}}{\partial \theta_k} & \frac{\partial F_{V_{reg}}}{\partial V_k} & 0 & 0 & 0 & \frac{\partial F_{V_{reg}}}{\partial \phi_g} \\
0 & \frac{\partial F_{m'_{ag}}}{\partial V_k} & 0 & 0 & 0 & 0
\end{bmatrix} \tag{4.144}$$

$$J_{22}=\begin{bmatrix}
\frac{\partial F_{e'_d}}{\partial e'_d} & \frac{\partial F_{e'_d}}{\partial e'_q} & \frac{\partial F_{e'_d}}{\partial \omega_m} & 0 & 0 & \frac{\partial F_{e'_d}}{\partial v_{dr}} & \frac{\partial F_{e'_d}}{\partial v_{qr}} & 0 & 0 & 0 & 0 & 0 & 0 & 0 \\
\frac{\partial F_{e'_q}}{\partial e'_d} & \frac{\partial F_{e'_q}}{\partial e'_q} & \frac{\partial F_{e'_q}}{\partial \omega_m} & 0 & 0 & \frac{\partial F_{e'_q}}{\partial v_{dr}} & \frac{\partial F_{e'_q}}{\partial v_{qr}} & 0 & 0 & 0 & 0 & 0 & 0 & 0 \\
\frac{\partial F_{\omega_m}}{\partial e'_d} & \frac{\partial F_{\omega_m}}{\partial e'_q} & \frac{\partial F_{\omega_m}}{\partial \omega_m} & \frac{\partial F_{\omega_m}}{\partial \beta_{aux}} & 0 & 0 & 0 & 0 & 0 & 0 & 0 & 0 & 0 & 0 \\
\frac{\partial F_{\beta_{aux}}}{\partial e'_d} & \frac{\partial F_{\beta_{aux}}}{\partial e'_q} & 0 & \frac{\partial F_{\beta_{aux}}}{\partial \beta_{aux}} & 0 & 0 & 0 & 0 & 0 & 0 & 0 & 0 & 0 & 0 \\
0 & 0 & 0 & 0 & \frac{\partial F_{\beta}}{\partial \beta} & 0 & 0 & 0 & 0 & 0 & 0 & 0 & 0 & 0 \\
\frac{\partial F_{i_{dr,aux}}}{\partial e'_d} & \frac{\partial F_{i_{dr,aux}}}{\partial e'_q} & 0 & 0 & 0 & \frac{\partial F_{i_{dr,aux}}}{\partial i_{dr,aux}} & 0 & 0 & 0 & 0 & 0 & 0 & 0 & 0 \\
\frac{\partial F_{v_{dr,aux}}}{\partial e'_d} & \frac{\partial F_{v_{dr,aux}}}{\partial e'_q} & 0 & 0 & 0 & 0 & \frac{\partial F_{v_{dr,aux}}}{\partial v_{dr}} & 0 & 0 & 0 & 0 & 0 & 0 & 0 \\
\frac{\partial F_{v_{qr,aux}}}{\partial e'_d} & \frac{\partial F_{v_{qr,aux}}}{\partial e'_q} & 0 & 0 & 0 & 0 & 0 & \frac{\partial F_{v_{qr,aux}}}{\partial v_{qr}} & 0 & 0 & 0 & 0 & 0 & 0 \\
0 & 0 & 0 & 0 & 0 & 0 & \frac{\partial F_{V_0}}{\partial v_{dr}} & \frac{\partial F_{V_0}}{\partial v_{qr}} & \frac{\partial F_{V_0}}{\partial V_0} & \frac{\partial F_{V_0}}{\partial i_{dcg}} & 0 & 0 & 0 & 0 \\
0 & 0 & 0 & 0 & 0 & 0 & 0 & 0 & \frac{\partial F_{i_{dcg,aux}}}{\partial V_0} & \frac{\partial F_{i_{dcg,aux}}}{\partial i_{dcg}} & 0 & 0 & 0 & 0 \\
0 & 0 & 0 & 0 & 0 & 0 & 0 & 0 & 0 & 0 & \frac{\partial F_{i_{reacg,aux}}}{\partial i_{reacg}} & 0 & 0 & 0 \\
0 & 0 & 0 & 0 & 0 & 0 & 0 & 0 & 0 & 0 & 0 & \frac{\partial F_{Q_{reg}}}{\partial Q_{reg}} & 0 & 0 \\
0 & 0 & 0 & 0 & 0 & 0 & 0 & 0 & \frac{\partial F_{V_{reg}}}{\partial V_0} & \frac{\partial F_{V_{reg}}}{\partial i_{dcg}} & \frac{\partial F_{V_{reg}}}{\partial i_{reacg}} & \frac{\partial F_{V_{reg}}}{\partial Q_{reg}} & \frac{\partial F_{V_{reg}}}{\partial V_{reg}} & \frac{\partial F_{V_{reg}}}{\partial m'_{ag}} \\
0 & 0 & 0 & 0 & 0 & 0 & 0 & 0 & 0 & 0 & 0 & 0 & \frac{\partial F_{m'_{ag}}}{\partial V_{reg}} & \frac{\partial F_{m'_{ag}}}{\partial m'_{ag}}
\end{bmatrix} \quad (4.145)$$

4.7 Initialization of DFIGs

When performing time-domain simulations of any power system, adequate initial conditions are mandatory if accuracy wants to be guaranteed. Such starting conditions are attained through a power flow calculation; however, the power flow computation also calls for providing good initial estimations of the state variables that take part in the iterative process. This becomes more important when the selected algorithm to solve the set of nonlinear equations is the Newton-Raphson technique. Bearing this in mind, suitable initial conditions can be obtained from the control strategies adopted to operate the machine.

To ensure that the wind turbine is operating at an optimal operating point from the beginning of the simulation, the initial values for the torque developed by the WRIG T_{ref} as well as its corresponding mechanical speed $\omega_m^{(0)}$ are firstly determined from the MPT curve (as seen in Figure 4.3) in accordance with the wind speed V_w at which the wind turbine is operating. Subsequently, the slip in per-unit value is computed as $s = \left(\omega_s - \omega_m^{(0)}\right) \Big/ \omega_s = 1 - \omega_m^{(0)}$ with the synchronous speed at its nominal value $\omega_s = 1$. From this wind generator's slip value and neglecting the power losses in the induction machine, the rotor voltage can be initially estimated by relating it to the stator voltage $V_k^{(0)}$ (or specified voltage at the GSC terminals) as $V_r^{(0)} = \left| sV_k^{(0)} \right|$. Hence, the initial rotor voltage values are estimated as follows:

$$\begin{bmatrix} v_{qr}^{(0)} \\ v_{dr}^{(0)} \end{bmatrix} = \begin{bmatrix} \cos\delta_r^{(0)} & \sin\delta_r^{(0)} \\ \sin\delta_r^{(0)} & -\cos\delta_r^{(0)} \end{bmatrix} \begin{bmatrix} V_r^{(0)} \\ 0 \end{bmatrix} \tag{4.146}$$

where

$$\delta_r^{(0)} = -\left(\omega_m^{(0)} \Big/ \omega_s \right) \theta_k^{(0)} \ . \tag{4.147}$$

If the wind generator is running at super-synchronous speed, $\omega_m^{(0)} > 1.0$, then

$$\phi_r^{(0)} = \pi \ . \tag{4.148}$$

Otherwise, if the wind generator is running at sub-synchronous speed, $\omega_m^{(0)} < 1.0$, then

$$\phi_r^{(0)} = 0 \ . \tag{4.149}$$

Additionally, the RSC modulation index is calculated as

$$m'^{(0)}_{ar} = \frac{V_r^{(0)}}{V_0^{(0)}} \ . \tag{4.150}$$

Moreover, the state variables associated with the GSC are initialized as $m_{ag}^{(0)} = 1$ and $\phi_g = 0$.

4.8 Synchronous generator and its controls

4.8.1 Synchronous generator

For the purpose of dynamic simulations, this work makes use of the synchronous generator two-axis model which is expressed in terms of four differential equations and two algebraic equations. The swing equation, given by two first-order differential equations, (4.151) and (4.152), describes the motion of the generators' rotor, whereas (4.153) to (4.154) define the electrical transient behavior of the rotor circuits, in the *dq* reference frame.

$$\frac{d\omega}{dt} = \frac{\omega_0}{2H}\left\{P_m - P_g - D\left(\omega - \omega_0\right)\right\} \tag{4.151}$$

$$\frac{d\delta}{dt} = \omega - \omega_0 \tag{4.152}$$

$$T'_{d0}\frac{dE'_q}{dt} = E_{fd} - E'_q - (X_d - X'_d)I_d \tag{4.153}$$

$$T'_{q0}\frac{dE'_d}{dt} = -E'_d - (X_q - X'_q)I_q \tag{4.154}$$

$$V_d = -R_a I_d + X'_q I_q + E'_d \tag{4.155}$$

$$V_q = -R_a I_q - X'_d I_d + E'_q \tag{4.156}$$

where T'_{d0}, T'_{q0} are open-circuit transient time constants; E'_d, E'_q are the internal transient flux voltages; V_d, V_q are generator's terminal voltages; E_{fd} is the excitation voltage; I_d, I_q are generators terminal currents; X'_d, X'_q are transient reactances; X_d, X_q are synchronous

reactances; H is the inertia constant [s], P_m is the mechanical input power [p.u], P_g is the electrical output power [p.u], D stands for the damping coefficient [s/rad], ω is the synchronous speed [rad/s], f_0 is the system operating frequency [Hz] and δ is the so-called load angle [rad].

4.8.2 Automatic voltage regulator (AVR)

A simplified version of the IEEE-type I AVR model [IEEE, 1968] is used in this work to regulate the voltage at the generator's terminals V through the applied field voltage E_{fd}. In this representation, the saturation function is neglected as well as the transductor function which represents the delay in the measuring of the voltage at the generator's terminal.

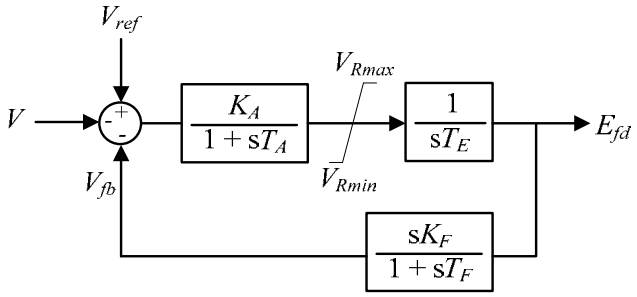

Figure 4.13: AVR dynamic model.

4.8.3 Turbine and governor

For the case of the hydroturbine and governor equipment, the models used in our dynamic simulations are shown in [Rafian et al., 1987]

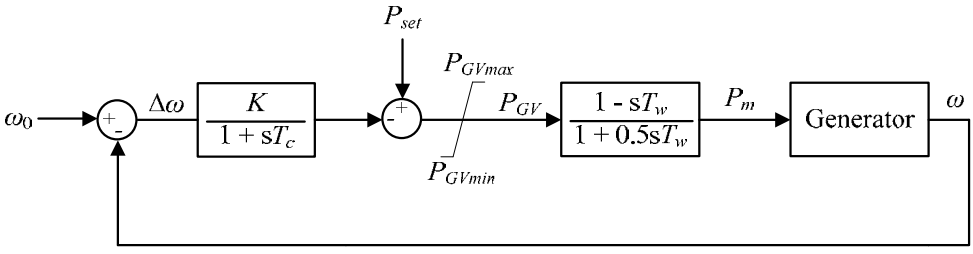

Figure 4.14: Dynamic model for the turbine-governor system

where T_w is the water time constant [s], P_{GV} is the equivalent input power to turbine [p.u] and P_m stands for the equivalent input power to generator [p.u], and ω_0 represents the nominal synchronous speed of the generator [p.u].

4.9 Methodology to applying disturbances

Discontinuity conditions are present in the daily operation of electrical networks. Such is the case of the disconnection of a transmission line or transformer, or just, the abrupt change of load or generation. A digital program developed to perform dynamic simulations in power systems, therefore, must be able to calculate the disturbance and post-disturbance condition. At the instant of the occurrence of the disturbance, the control variables associated with the dynamic controllers cannot change instantaneously. At this point in time, these variables are kept constant and their corresponding changes with respect to time become zero. The algebraic variables, however, are abruptly adjusted so as to accomplish the power balance at all nodes of the system. For the purpose of software implementation, this work follows the approach of setting the integration step to zero: $\Delta t = 0$, whereas the set of algebraic equations are solved considering the control variables associated with the differential equations as a fixed input at the very moment of the application of the disturbance.

As mentioned in section 4.2, the frame of reference employed in this thesis takes advantage of the Newton's algorithm. The conventional Jacobian matrix $\boldsymbol{J}$ is enlarged, as shown in (4.157), to accommodate both the set of power mismatch equations arising from the network, ΔP and ΔQ, and the set of discretized differential equations corresponding to the dynamics of the synchronous machines and DFIGs along with their dynamic controllers, $F(y)$.

$$\begin{bmatrix} \Delta P \\ \Delta Q \\ \Delta F_1(y) \\ \vdots \\ \Delta F_n(y) \end{bmatrix}^i = \begin{bmatrix} \frac{\partial \Delta P}{\partial \theta} & \frac{\partial \Delta P}{\partial V} & \frac{\partial \Delta P}{\partial y_1} & & \frac{\partial \Delta P}{\partial y_n} \\ \frac{\partial \Delta Q}{\partial \theta} & \frac{\partial \Delta Q}{\partial V} & \frac{\partial \Delta Q}{\partial y_1} & \cdots & \frac{\partial \Delta Q}{\partial y_n} \\ \frac{\partial \Delta F_1(y)}{\partial \theta} & \frac{\partial \Delta F_1(y)}{\partial V} & \frac{\partial \Delta F_1(y)}{\partial y_1} & & \frac{\partial \Delta F_1(y)}{\partial y_n} \\ & \vdots & & \ddots & \vdots \\ \frac{\partial \Delta F_n(y)}{\partial \theta} & \frac{\partial \Delta F_n(y)}{\partial V} & \frac{\partial \Delta F_n(y)}{\partial y_1} & \cdots & \frac{\partial \Delta F_n(y)}{\partial y_n} \end{bmatrix}^i \begin{bmatrix} \Delta\theta \\ \Delta V \\ \Delta y_1 \\ \vdots \\ \Delta y_n \end{bmatrix}^i \tag{4.157}$$

Let the disturbance be applied at $t = t_0$, the solution to the whole set of equations is then found as (4.158), recalling that $y_{t=t_0} = y_{t=t_0-\Delta t}$:

$$\begin{bmatrix} \Delta P \\ \Delta Q \\ \Delta F_1(y) = 0 \\ \vdots \\ \Delta F_n(y) = 0 \end{bmatrix}_{t=t_0}^{i} = \begin{bmatrix} \frac{\partial \Delta P}{\partial \theta} & \frac{\partial \Delta P}{\partial V} & 0 & & 0 \\ \frac{\partial \Delta Q}{\partial \theta} & \frac{\partial \Delta Q}{\partial V} & 0 & \cdots & 0 \\ 0 & 0 & 1 & & 0 \\ & \vdots & & \ddots & \vdots \\ 0 & 0 & 0 & \cdots & 1 \end{bmatrix}_{t=t_0}^{i} \begin{bmatrix} \Delta\theta \\ \Delta V \\ \Delta y_1 \\ \vdots \\ \Delta y_n \end{bmatrix}_{t=t_0}^{i}$$

(4.158)

Once the numerical solution has been found for $t = t_0$, the new values for the algebraic variables $\Delta\theta$ and ΔV are used together with (4.157) to compute all the state and control variables in the ensuing integration step. The simulation continues until the final time of simulation is reached.

4.10 Conclusions

The mathematical model of an advanced DFIG has been put forward in this chapter. It departs radically from the idea of representing the RSC and GSC as equivalent voltage sources. Instead the individual converters are modeled by using a new representation of the VSC where the main parameters such as amplitude modulation ratio, switching and conduction losses, reactive power production and the DC bus are all explicitly represented. The back-to-back connection of two of these VSC models enables the explicit representation of the DC bus and explicit voltage and current ports on both sides of the VSC-HVDC-link for direct connection with the stator and rotor terminals of the wound rotor induction machine, resulting in a brand new model of the DFIG with unrivalled modeling flexibility for the purpose of fundamental frequency, positive-sequence power flow studies.

This model covers both the steady-state and the dynamic operating regimes. It is perhaps in the latter where the new model of the back-to-back VSC-HVDC converter shows its full capabilities, it cannot only be easily combined with the rest of the dynamic equations and the rotating frame-of-reference of the WRIG but its adaptation to a wide range of control strategies; resulting in a rather advanced DFIG dynamic model for performing time domain simulations. Concerning the numerical implementation of the overall dynamic model, the differential equations of all the controllers are discretized using the trapezoidal rule integration and the ensuing equations are linearized and suitably combined with non-linear algebraic equations of the static part of the network for unified iterative solutions at each time step. In this extended frame-of-reference, all elements of the conventional power grid,

including electrical, electronic and mechanical components in either static or dynamic form, are assembled together for unified iterative dynamic solutions of large scale power systems, where the latest addition is the representation of DFIG wind power generators.

Chapter 5

CASE STUDIES

5.1 Introduction

In this Chapter, the various wind generator models developed within the unified frame-of-reference using the Newton-Raphson method, are put through their paces. The models coded in software are suitable for carrying out conventional power flow studies as well as for conducting power flow studies taking due account of frequency deviations and automatic load/frequency responses. The results obtained from the proposed models included in the conventional power flow tool are validated with respect to those associated with the proposed models and its solution technique reported in [Divya and Rao, 2006], whereas the model that serves as basis for developing frequency-responsive fixed speed wind generators, namely the FP-FSWG, is corroborated by comparison with an existing wind generator model in the software Simulink. All the steady-state models are additionally tested on a variety of power networks: an 8-bus system, the IEEE 14-bus system, the IEEE 30-bus system and the IEEE 118-bus system. On the other hand, the new DFIG model for steady-state and dynamic simulations is validated by appealing to its captured physical phenomena during the performed tests using the 8-bus system and the IEEE 30-bus network.

The wind farms are implemented and simulated according to the procedure shown in Section 2.8. All the models and methods developed in this research work were coded in Matlab and its simulation environment was used to run all the cases presented in this thesis.

5.2 Conventional power flows

5.2.1 IEEE 14-bus network, 3 wind farms

The typical IEEE 14-bus network is used to illustrate the power flow solutions given by the N-R method. As shown in Figure 5.1, it contains two synchronous generators (SG), three synchronous condensers (SC), seventeen transmission lines and three transformers. This test system is slightly modified to include three wind farms comprising five FP-FSWGs, five

PR-FSWGs and five SSWGs, connected at nodes 10, 11 and 12, respectively, through a step-up transformer with a reactance of 0.08p.u. The mathematical models of wind generators are implemented in the NR algorithm for solving power flows with a convergence criterion of 10^{-12}. The power flow results are obtained assuming that wind speed is V_w = 10 m/s at all wind farms. The information regarding the parameters of the power system and wind generators can be found in Appendix D.

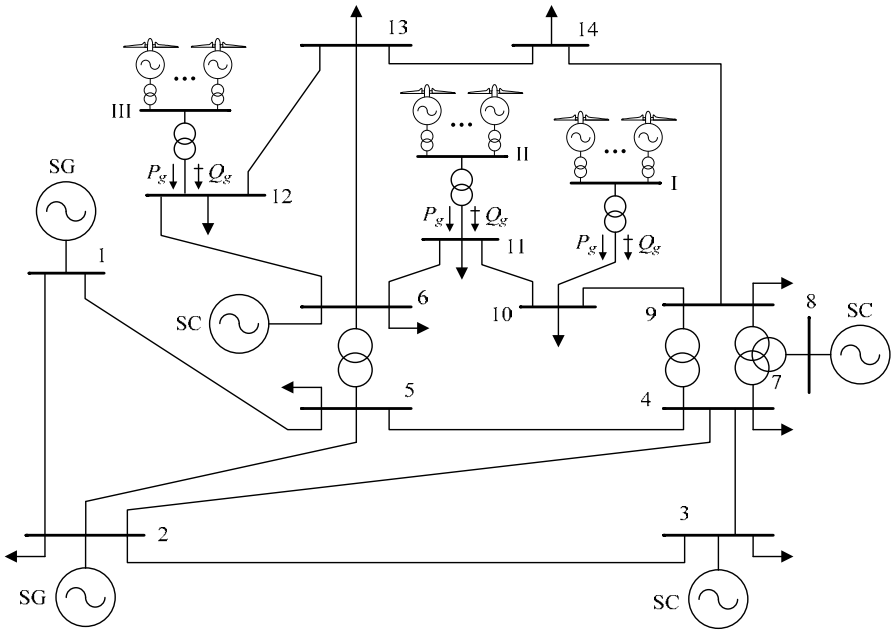

Figure 5.1: Modified IEEE 14-bus network to incorporate three wind farms.

For the sake of validating some of the new developed models along with its implementation, a comparison is carried out against the models and formulation presented in [Divya and Rao, 2006]. As reported in Table 5.1, the computed state variables associated with wind generators are quite similar in both approaches, causing that the generated active and reactive powers as well as the voltage magnitudes at the point of interconnection of the wind farms to be practically equal. The proposed formulation, however, performs better in terms of number of iterations with respect to the case of the sequential approach proposed in [Divya and Rao, 2006].

Table 5.1: Comparison between the new formulation and an existing one

Models	WECS	P_g (MW)	Q_g (MVAr)	V (p.u)	s	R_x	Iterations
Proposed	I. FP-FSWG	2.9882	-0.7399	1.05181	-0.00264	------	4
	II. PR-FSWG	1.7985	-0.0271	1.05809	-0.00272	------	
	III. SSWG	2.9545	-0.7026	1.05684	------	-163.30541	
[Divya and Rao, 2006]	I. FP-FSWG	2.9803	-0.7380	1.05181	-0.00263	------	8
	II. PR-FSWG	1.7985	-0.0271	1.05809	-0.00272	------	
	III. SSWG	2.9545	-0.6964	1.05685	------	-164.46175	

5.2.2 IEEE 30-bus network, 4 wind farms

The standard IEEE 30-bus test system depicted in Figure 5.2 is used to incorporate four wind farms connected one at a time at node 30, as shown in Table 5.2, through a step-up transformer with a reactance of 0.08p.u. This power system comprises two synchronous generators, four synchronous condensers, thirty four transmission lines and seven transformers. In this case, the reactive power limits of the synchronous generators and condensers are not considered in the simulations. The data for this system are also presented in Appendix D.

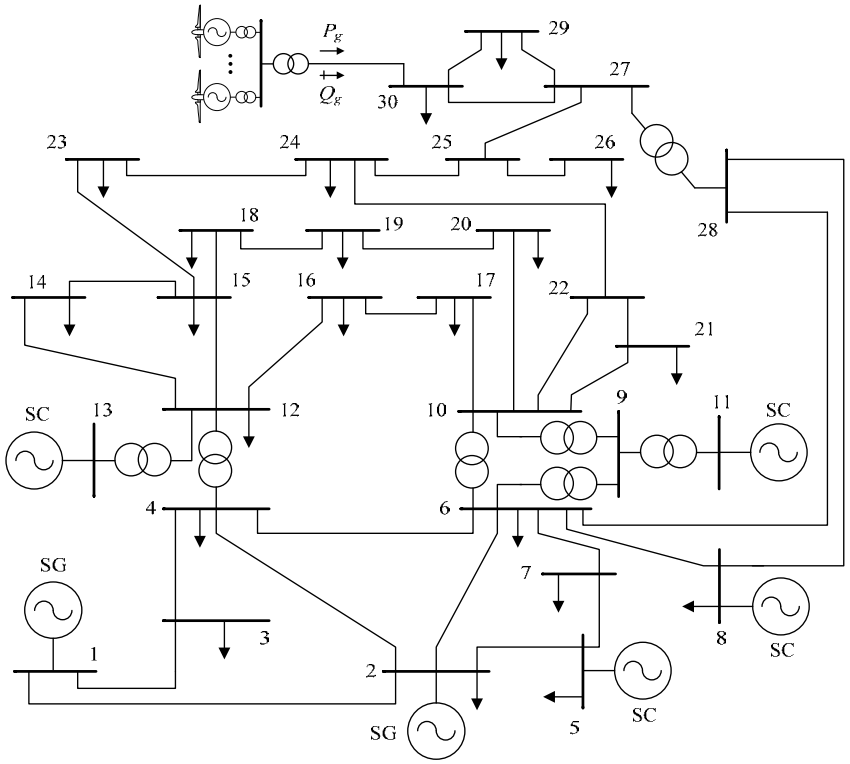

Figure 5.2: Modified IEEE 30-bus network to incorporate wind farms

For the WECS described in Table 5.2, the same wind speed is assumed for all wind farms. The nominal power P_{nom} as well as its reactive power compensation Q_{comp} for each

wind generator is provided. For the fixed speed and semi variable speed wind generators, the reactive power compensation is modeled as fixed capacitor banks, whereas for the DFIG the reactive power is provided as a function of the maximum/minimum possible power factor at which the power converter connected to the grid can operate. The convergence criterion in the NR algorithm for power flow mismatches is assumed to be 10^{-12}.

Table 5.2: Models of wind generators connected to IEEE 30-bus test system

Model	Number of WGs	P_{nom} (MW)	Q_{comp} (MVAr)	WECS total capacity
I. FP-FSWG	20	0.9	30% of P_{nom}	18 MW
II. PR-FSWG	30	0.6	30% of P_{nom}	18 MW
III. SSWG	20	1.0	30% of P_{nom}	20 MW
IV. DFIG	10	2.0	±0.95 pf	20 MW

The outcome of the power flow simulations for different wind conditions: 8, 10 and 12 m/s, is shown in Table 5.3. Since the wind generators making up each wind farm are placed very close to each other, electrically speaking, and hence no power losses are incurred inside the wind farm, then their corresponding state variables, s and R_x, turn out to be numerically the same. It should be brought to attention that disregarding the various simulated scenarios, the voltage magnitude at wind farm's point of connection to the grid is not considerably deviated from 1 p.u. This is so because, even when the reactive power consumed by the wind farms is increasing when the wind speed is higher, the active power is also increased and the neighboring loads are being fed locally, thus resulting in less power losses.

Table 5.3: Results with WECS connected to node 30 of the IEEE 30-bus test system

Case	Type of WECS	P_g (MW)	Q_g (MVAr)	V (p.u)	s	R_x	Iterations
1 V_w= 8 m/s	I	6.409	-1.933	0.997	-0.00158	--	4
	II	5.787	0.894	1.015	-0.00155	--	4
	III	7.887	-1.792	1.002	--	-221.768	4
	IV (1 pf)	5.556	-0.225	1.007	--	--	4
2 V_w= 10 m/s	I	11.953	-3.337	1.002	-0.00296	--	4
	II	10.791	-0.761	1.017	-0.00297	--	4
	III	11.818	-3.406	1.001	--	-143.1047	4
	IV (0.98 pf)	12.000	2.575	1.045	--	--	4
3 V_w= 12 m/s	I	16.079	-4.990	1.001	-0.00408	--	4
	II	15.304	-3.455	0.996	-0.00452	--	4
	III	17.000	-7.127	0.987	--	-88.990	5
	IV (0.96 pf)	16.888	3.871	1.061	--	--	5

As expected, the simulations indicate that the principles in the operation of wind generators are consistent, i.e., the higher the wind speed, the higher the active power generated by the wind farms. Note that the algorithm takes four iterations in most cases regardless of the value of the wind speed, being the proposed approach very efficient to determine the impact of the inclusion of WECS in a power system. In other words, the inherent convergence characteristics of the NR method are not affected by the equations that arise from the wind generators.

5.2.3 IEEE 118-bus network, 4 wind farms

To further prove the performance of the proposed formulation, a more complex system has been used. The IEEE 118-bus test system has been modified to consider four different types of wind farms distributed in different buses as described in Table 5.4, with 80 wind generators in total.

Table 5.4: WECS connected to IEEE 118-bus test system

Model	Number of WGs	Bus	WECS capacity
I. FP-FSWG	20	38	18 MW
II. PR-FSWG	30	81	18 MW
III. SSWG	20	102	20 MW
IV. DFIG (1 pf)	10	109	20 MW

Likewise, the same assumptions described in the previous example have been considered in performing the simulations whose results are reported in Table 5.5. The third column reports the results associated with the base case: wind farms are not connected to the system. Results obtained for wind speeds of 11 m/s, 13 m/s, and 15 m/s are detailed in columns 4, 5, and 6, respectively. The same number of iterations was required for all simulations.

Table 5.5: Power flow results for the IEEE 118-bus test system

WECS		Wind speed (m/s)			
Bus no.	Results	Base case	11	13	15
38	P_g (MW)	----	14.262	17.361	18.318
	Q_g (MVAr)	----	-4.345	-5.925	-6.495
	V (p.u)	0.9613	0.9609	0.9606	0.9605
81	P_g (MW)	----	13.500	17.109	18.762
	Q_g (MVAr)	----	-2.414	-5.175	-6.845
	V (p.u)	0.9968	0.9967	0.9963	0.9961
102	P_g (MW)	----	14.600	18.400	19.800
	Q_g (MVAr)	----	-5.189	-8.535	-10.20
	V (p.u)	0.9891	0.9882	0.9870	0.9864
109	P_g (MW)	----	14.666	18.666	20.000
	Q_g (MVAr)	----	-1.711	-2.795	-3.220
	V (p.u)	0.9670	0.9687	0.9689	0.9689
Iterations		5	5	5	5

5.3 Power flows with automatic load-frequency devices

5.3.1 8-bus network, 1 FP-FSWG

The FP-FSWG model along with its implementation within the PFALFC algorithm is used to assess its response in view of frequency disturbances. This new developed model is compared to an existing model from the well-known simulation software Matlab/Simulink. For this validation test, the 8-bus test system operating at 50 Hz depicted in Figure 5.3 is used. It comprises two synchronous generators, one FP-FSWG, four transformers and four transmission lines. Only the SG connected at node 1 has the automatic load-frequency control capability, and the one connected to node 3 acts as a *PV* generator controlling its terminal voltage to 1 p.u.

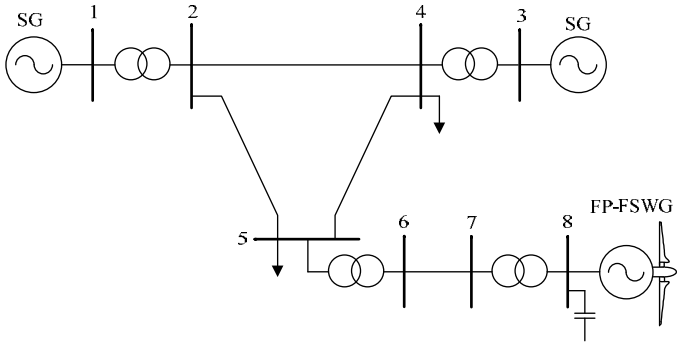

Figure 5.3: Power system used for the validation test.

The validation test consists of comparing the electrical response of the FP-FSWG for different values of the system frequency by using a dynamic and stationary analysis. The wind speed of the wind generator is 17 m/s for both studies. The additional information concerning the test system is found in the Appendix D. The Simulink tool aids in executing the former analysis, using library models for the asynchronous generator and the wind turbine. In this case, the values of the frequency shown in Table 5.6 are set by specifying the angular speed reference of the synchronous machine's governor ω_{ref}, and the steady-state values of P_g, Q_g, T_m and ω_m are then obtained after 60 seconds of time simulation. On the other hand, the stationary analysis is effectuated by employing the proposed PFALFC approach with a convergence criterion of 10^{-12}. In this case, the loads connected at nodes 4 and 5 are modified by a trial and error process until the power flow solution converges to an equilibrium point corresponding to each value of the system frequency shown in the first column of Table 5.6. For the same values of the frequency, the wind generator computed variables are quite similar to those from the dynamic simulation. In fact, the largest errors were 0.26% for P_g at 51 Hz, 2.53% for Q_g at 48 Hz, 0.29% for T_m at 50.5 Hz and 0.18% for ω_m at 51 Hz. Consequently, the suggested model can manage to reliably predict the electrical response of a FP-FSWG after the action of the primary frequency regulation.

Table 5.6: Validation test for the FP-FSWG model

Frequency (Hz)	Simulink				Proposed formulation			
	P_g (MW)	Q_g (MVAr)	T_m (p.u)	ω_m (p.u)	P_g (MW)	Q_g (MVAr)	T_m (p.u)	ω_m (p.u)
48.0	1.7303	-0.9083	-0.8501	0.9745	1.7265	-0.8853	-0.8516	0.9754
48.5	1.7822	-0.9241	-0.8676	0.9851	1.7788	-0.9069	-0.8688	0.9858
49.0	1.8343	-0.9409	-0.8849	0.9956	1.8313	-0.9287	-0.8858	0.9962
49.5	1.8864	-0.9591	-0.9018	1.0061	1.8827	-0.9453	-0.9033	1.0071
50.0	1.9383	-0.9787	-0.9185	1.0168	1.9336	-0.9639	-0.9209	1.0182
50.5	1.9902	-0.9981	-0.9349	1.0273	1.9849	-0.9867	-0.9377	1.0291
51.0	2.0421	-1.0194	-0.9510	1.0378	2.0366	-1.0117	-0.9538	1.0397
51.5	2.0936	-1.0414	-0.9667	1.0484	2.0891	-1.0374	-0.9691	1.0501
52.0	2.1452	-1.0648	-0.9821	1.0589	2.1422	-1.0632	-0.9837	1.0601

5.3.2 8-bus network, 1 PR-FSWG

As stated in Section 3.3.2, the blade pitch angle regulator acts when the generated active power of a PR-FSWG rises above its maximum allowed power P_{gmax}. In this context, because the power output of any FSWG is frequency dependent, the blade angle regulator can be activated or deactivated depending on the frequency deviations in the network, and not only because of wind speeds beyond a specified rated value. To validate this statement, this

example concerns the performance of the PR-FSWG model when using the PFALFC algorithm. The same 8-bus test system used in the previous example is employed along with its assumptions; in this case the PR-FSWG replaces the SR-FWG as shown in Figure 5.4.

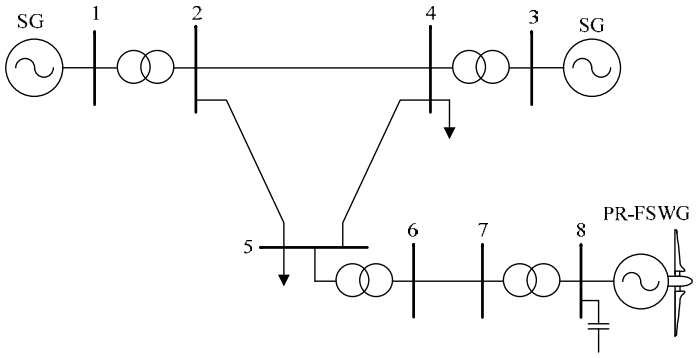

Figure 5.4: Power system used to accommodate a PR-FSWG.

The disturbances ΔD that deviate the frequency from its nominal value are simulated by altering the active and reactive power demanded by all the system's loads assuming a constant power factor. The base case corresponds to the power flow solution obtained by considering that ΔD=0%. For all simulations whose power flow solutions are reported in Table 5.7 for a power mismatch tolerance of 10^{-12}, the rated values of the active power and the wind speed of the wind generator are 2 MW and 15 m/s, respectively.

Table 5.7: Electrical response of a PR-FSWG for different ΔD values

Wind speed (m/s)	Electrical response	ΔD= 0%	ΔD=10%	ΔD= -10%
V_w= 14 m/s	P_g (MW)	1.9066	1.8739	1.9393
	Q_g (MVAr)	-0.9516	-0.9406	-0.9650
	V (p.u)	0.9967	1.0065	0.9921
	ω_m (p.u)	1.0179	1.0086	1.0271
System frequency (Hz)		50	49.5757	50.4220
Iterations		4	4	4
V_w= 15 m/s	P_g (MW)	1.9969	1.9567	2.0000
	Q_g (MVAr)	-0.9937	-0.9773	-1.1741
	V (p.u)	0.9966	1.0064	0.9913
	ω_m (p.u)	1.0188	1.0094	1.0311
System frequency (Hz)		50	49.5755	50.4213
Iterations		4	4	6
V_w= 16 m/s	P_g (MW)	2.0000	1.9951	2.0000
	Q_g (MVAr)	-1.1685	-0.9949	-1.1740
	V (p.u)	0.9959	1.0063	0.9913
	ω_m (p.u)	1.0222	1.0098	1.0311
System frequency (Hz)		50	49.5769	50.4220
Iterations		6	4	5

Three key aspects can be drawn from the results presented in Table 5.7. Firstly, when simulating the PR-FSWG with a wind speed of 14 m/s, the generated active and reactive powers are different for each value of ΔD. This is primarily because of the frequency deviations since they force the wind generator to find another equilibrium point. Secondly, the blade pitch angle mechanism is activated when simulating a ΔD=-10% at rated wind speed. In this case, the generated active power hits P_{gmax} because of the increment in the system's frequency. Lastly, when simulating the scenario where the wind speed is above the rated one, i.e. 16 m/s, a deactivation of the pitch angle mechanism occurs because of the frequency drop caused by the increase of 10% in the total system load.

The above conclusions can be physically inferred: a decrease in the mechanical speed of the induction machine will lead to a decrement in the output power of the wind generator and vice versa.

The number of iterations required to obtain the solution in each case is also reported in Table 5.7. Note that in this scenario, the algorithm arrives at the solution in four iterations except when the pitch angle mechanism is activated as described above; in this case, one or two additional iterations are needed to obtain the power flow solution since the activation/deactivation can be seen as numerical perturbations that delay the convergence of the algorithm.

5.3.3 IEEE 14-bus network, 2 wind farms

The well-known IEEE 14-test system (as seen in Figure 5.1) is used to provide another example with the inclusion of two wind generator models within the context of the PFALFC tool. In this case, the test network is slightly modified to incorporate two wind farms made up of ten FP-FSWGs and forty DFIGs connected at nodes 10 and 12, respectively. The characteristics of the generators and loads are given in the Appendix D.

One has to bear in mind that the FP-FSWG responds naturally to frequency deviations in the system. Conversely, the DFIG model is endowed with the frequency regulation capability according to the level of deloading of its wind turbine. However, for the sake of comparison, this example presents the power flow results without frequency regulation for the DFIG as well. Two scenarios are presented regarding the active power regulation capability of the DFIG-based wind farm, i.e. η = 5% and η = 10% of the deloading of each wind generator. Simulation results are reported in Table 5.8.

Table 5.8: Power flow results for the IEEE 14-bus test system including wind farms

Wind farm	Results	Deloading of DFIG, η = 5%				Deloading of DFIG, η = 10%			
		DFIG without regulation		DFIG with regulation		DFIG without regulation		DFIG with regulation	
		ΔD=7%	ΔD=15%	ΔD=7%	ΔD=15%	ΔD=7%	ΔD=15%	ΔD=7%	ΔD=15%
I. FP-FSWG V_w= 16 m/s	P_q (MW)	18.659	18.402	18.700	18.444	18.660	18.402	18.742	18.487
	Q_q (MVAr)	-3.732	-3.609	-3.762	-3.640	-3.727	-3.604	-3.789	-3.667
	V(pu)	1.003	1.004	1.002	1.002	1.003	1.004	1.001	1.002
II. DFIG V_w= 15 m/s	P_g (MW)	76.00	76.00	80.00	80.00	72.00	72.00	80.00	80.00
	Q_q (MVAr)	-3.611	-3.617	-3.986	-3.993	-3.254	-3.260	-3.987	-3.994
	V(pu)	1.068	1.067	1.071	1.069	1.066	1.065	1.070	1.069
System's frequency (Hz)		49.755	49.473	49.801	49.521	49.755	49.473	49.847	49.567

The system frequency is improved substantially when the DFIG-based wind farm is providing frequency regulation. For example, when an increase in the system load of ΔD = 15% is simulated, the frequency deviation is 0.433 Hz and 0.527 Hz with and without frequency regulation support, respectively, as seen in Table 5.8 for η = 10%. Furthermore, the power system experiences a smaller frequency deviation when the level of deloading of the wind turbines is higher. However, from the system's frequency perspective, it should be taken into account that not only the percentage of the deloading of the wind turbines will impact the final value of the frequency when facing a perturbation, but also the number of wind generators and the level of the system demand will do it.

5.3.4 IEEE 14-bus network, 4 wind farms

Lastly, in order to examine the joint operation of all the wind generator models proposed within the context of the PFALFC algorithm, the IEEE 14-bus test system is modified according to Figure 5.5 to accommodate four wind farms. Wind farms I and II are composed of five FP-FSWGs and five PR-FSWGs, respectively, whereas the remaining are VSWG-based wind farms comprised of fifteen DFIGs and fifteen PMSGs, respectively. The DFIGs are operating at unity power factor whereas the PMSGs are controlling their terminal voltage at 1 p.u. Generators connected at buses 1 and 2 are assumed to possess automatic load-frequency control capability, where the generator 1 is considered as the reference generator.

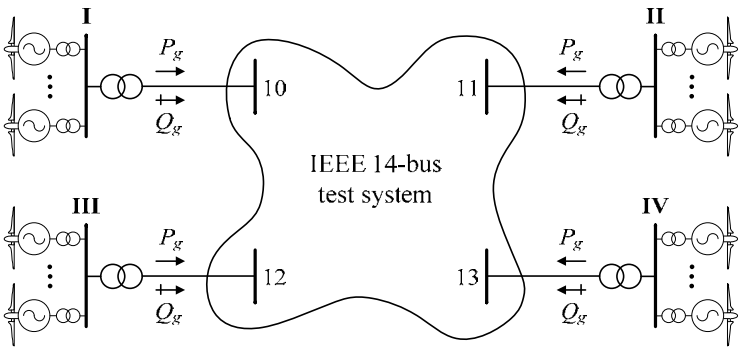

Figure 5.5: Modified IEEE 14-bus test system.

In this example, the active and reactive powers generated by each wind farm as well as the system frequency are reported for two different load perturbations in the system, that is, ΔD=7% and ΔD=15%. In addition, two scenarios were simulated to demonstrate the power regulation capability of the VSWG-based wind farms by assuming a deloading of 5% and 10% for each wind generator composing these wind farms. The power flow results of these simulations are given in Table 5.9.

Table 5.9: Power flow results and system's frequency for different values of ΔD and η

Wind farm	Results	Deloading of VSWGs, η = 5%				Deloading of VSWGs, η = 10%			
		Without frequency regulation		With frequency regulation		Without frequency regulation		With frequency regulation	
		ΔD=7%	ΔD=15%	ΔD= 7%	ΔD=15%	ΔD=7%	ΔD=15%	ΔD=7%	ΔD=15%
I. FP-FSWG V_w= 16 m/s	P_q (MW)	9.323	9.198	9.339	9.215	9.323	9.198	9.355	9.232
	Q_g (MVAr)	-1.929	-1.866	-1.942	-1.879	-1.928	-1.865	-1.953	-1.891
	V_I (p.u)	0.978	0.979	0.977	0.978	0.978	0.979	0.976	0.977
II. PR-FSWG V_w= 14 m/s	P_q (MW)	9.432	9.323	9.447	9.338	9.432	9.323	9.461	9.353
	Q_q (MVAr)	-1.939	-1.888	-1.949	-1.898	-1.938	-1.887	-1.957	-1.907
	V_{II} (p.u)	0.986	0.986	0.985	0.986	0.986	0.986	0.985	0.985
III. DFIG V_w= 15 m/s	P_q (MW)	28.500	28.500	30.000	30.000	27.000	27.000	30.000	30.000
	Q_q (MVAr)	-0.712	-0.713	-0.788	-0.789	-0.641	-0.641	-0.788	-0.789
	V_{III} (p.u)	1.013	1.012	1.014	1.013	1.012	1.011	1.014	1.013
IV. PMSG V_w= 15 m/s	P_q (MW)	28.500	28.500	30.000	30.000	27.000	27.000	30.000	30.000
	Q_q (MVAr)	3.904	4.703	3.477	4.284	4.407	5.209	3.545	4.363
	V_{IV} (p.u)	1.000	1.000	1.000	1.000	1.000	1.000	1.000	1.000
System's frequency (Hz)		49.7627	49.4885	49.7995	49.5261	49.7626	49.4883	49.8362	49.5635

As expected, for the case of the FSWG-based wind farms, simulations show that their active and reactive powers are different from one scenario to another because of their frequency and voltage dependency. Additionally, the PMSG-based wind farm controls its terminal voltage at 1 p.u., as specified in all simulations, by injecting into the grid the required reactive power. In contrast, the DFIG-based wind farm is absorbing reactive power to cope with the reactive power losses of each wind turbine's individual transformer because

the wind generators are operating at unity power factor. Such a situation is also reflected in the different voltage magnitudes V_{III} obtained for the various scenarios.

The results presented in Table 5.9 also reveal that a load increase of 15% leads to a system frequency beyond 49.5 Hz when the VSWG-based wind farms are not providing frequency support. However, when they are participating in the frequency control, all wind turbines use all their spinning reserve regardless of the level of deloading, resulting in a system frequency of 49.526 Hz and 49.563 Hz for η = 5% and 10%, respectively.

In this case, the wind power penetration accounts for 30% of the total system load. The VSWG-based wind farms' contribution to the frequency regulation corresponds to 3 MW and 6 MW of active power that was used as spinning reserve for η = 5% and 10%, respectively. If frequency response is provided by wind farms then the power system is clearly strengthened and acquires more flexibility when facing abnormal conditions. The importance of the deloading of wind generators lies in the fact that the system will count on other distributed slack generators which will help to mitigate active power imbalances.

5.4 Time-domain simulations with DFIGs

Two study cases are carried out so as to show the dynamic behavior of the newly developed DFIG. In both cases all the synchronous generators are modeled as shown in section 4.8. Likewise, all the active and reactive powers drawn by the loads are represented by their polynomial representation [Kundur, 1994], shown in (3.7) and (3.8), in which their degree of dependency with respect to their terminal voltage is taken into account. The corresponding parameters of such models are given in the Appendix D.

5.4.1 8-bus network, 1 DFIG

To illustrate the steady-state and dynamic performance of the enhanced DFIG model presented in Chapter 4, the 8-bus power system is considered in this case of study. A DFIG is embedded in this network at node 8 as shown in Figure 5.6. To begin with, the wind generator is tested only for the steady-state regime. Several scenarios are simulated where the DFIG is subjected to different wind speed values. The nominal values of the DFIG are P_{nom} = 2 MW and V_w =12 m/s, whereas its B-B converter is assumed to be rated at 35% of the DFIG's nominal power: $S_{nom,b\text{-}b} = 0.35P_{nom}$. The system data is presented in the Appendix D along with the rest of the DFIG parameters.

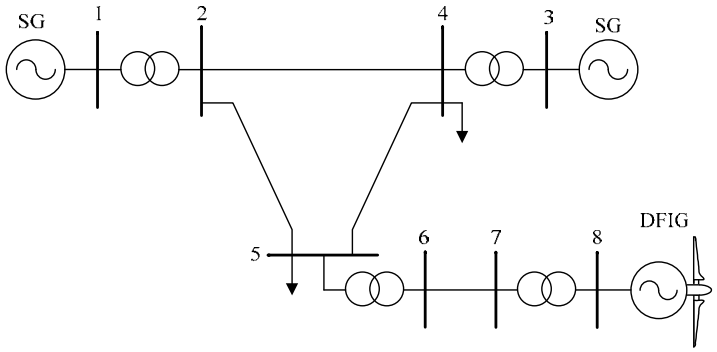

Figure 5.6: Power system used to accommodate a DFIG.

The state variables as given by the NR algorithm are presented in Table 5.10. These results are obtained under the following two conditions: (i) the grid-side converter is responsible for exerting voltage control at its corresponding AC terminal at V_8 = 1p.u; (ii) whilst the rotor-side converter is controlling the rotor's voltage so as to uphold the active and reactive power commands for the WRIG, i.e., $T_m = T_{m,ref}$ and $Q_{gs} = Q_{gs,ref}$, respectively. The reference torque is obtained from the MPT controller according to the prevailing wind conditions. On the other hand, the reference value of reactive power for the machine's stator is computed assuming that a fixed unity power factor strategy is followed, $cos(\varphi) = 1$; hence, $Q_{gs,ref} = P_{nom}\ tan(0) = 0$. All values are given in per-unit except those for the angles which are given in degrees.

With unity power factor in the stator, the angle between the stator voltage $\mathbf{V_s}$ and the stator current $\mathbf{I_s}$ becomes zero. Given that the machine's magnetization is produced through the rotor, this causes the magnitude of the rotor's current $\mathbf{I_r}$ to be larger than the current yielded in the stator $\mathbf{I_s}$. This has a direct correlation with the fact in order to produce a unity power factor in the stator: the magnetic flux in the rotor $\mathbf{Y_r}$ is bigger than the one produced in the stator $\mathbf{Y_s}$. As expected, the angle of the magnetic flux in the stator $\mathbf{Y_s}$ corresponds to the voltage angle in the stator at the network's reference frame, θ_k. Furthermore, for the subsynchronous condition, $\mathbf{V_r}$ is almost in phase with the inner e.m.f **E'**, and for the supersynchronous condition both voltages are in anti-phase. These statements are supported by the space-phasor diagram shown in Figure 5.7 which is obtained fixing the coordinate system space at the synchronous speed, $\omega_b = \omega_s$.

Table 5.10: Results given by the power flow solution for different wind speeds

Results	Wind speed (m/s)					
	7	8	9	10	11	12
V_k	1.00000	1.00000	1.00000	1.00000	1.00000	1.00000
θ_k	-4.32452	-4.27858	-4.21976	-4.14656	-4.05748	-3.95105
Subsynchronous operation				Supersynchronous operation		
ω_m	0.72052	0.82302	0.92612	1.02923	1.13172	1.23483
$T_{m,ref}$	-0.28223	-0.36882	-0.46667	-0.57602	-0.69725	-0.82964
E'_d	-0.07547	-0.12228	-0.17514	-0.23417	-0.29952	-0.37078
E'_q	1.01349	1.01837	1.02376	1.02961	1.03584	1.04234
V_{dr}	-0.01882	-0.01927	-0.01006	0.01071	0.04487	0.09467
V_{qr}	0.30063	0.19491	0.08775	-0.02037	-0.12892	-0.23932
m_{ar}	0.30232	0.23302	0.17602	0.14492	0.15415	0.19736
ϕ_r	15.59211	27.61074	46.85392	76.68056	110.45696	136.18741
B_{eqr}	0.01298	0.02295	0.04324	0.068434	0.06287	0.03667
m_{aq}	0.82361	0.82344	0.82321	0.82295	0.82263	0.82227
ϕ_q	-4.46339	-4.39739	-4.29152	-4.13914	-3.93398	-3.66804
B_{eqg}	0.00607	0.00591	0.00572	0.00548	0.00520	0.00488
I_{ds}	0.02117	0.02734	0.03406	0.04124	0.04874	0.05635
I_{qs}	0.28005	0.36545	0.46166	0.56884	0.68722	0.81598
I_{dr}	-0.16675	-0.17336	-0.18059	-0.18832	-0.19642	-0.20465
I_{qr}	-0.27950	-0.36817	-0.46810	-0.57942	-0.70239	-0.83619

Note that the value of the modulation index of the GSC m_{ag} does not change substantially from low to high wind speeds. This is so because, as shown in Table 5.11, the amount of reactive power that is produced by the GSC, in order to uphold the DFIG's terminal voltage at the specified value, changes little for the various wind speed conditions. However, this is not the case for the modulation index of the RSC, given that its value is calculated in accordance with the proper rotor's voltage that enables to achieve the torque and stator's reactive power commands, $T_{m,ref}$ and $Q_{gs,ref}$. It stands out that the farther the WRIG is operating from the synchronous speed, the larger the voltage magnitude at the rotor's side is; this is also reflected in the computed values for the m_{ar}.

From results yielded by the power flow solution, it can be seen that the GSC's phase-shifting angle ϕ_g is very much like the voltage angle of the node where the DFIG is connected, θ_k; this was expected as this converter is directly interacting with the network's voltage. Yet, these angles clearly differ from those computed for the RSC's phase-shifting angle, since its values were found within a wider range, $0<\phi_r<\pi$.

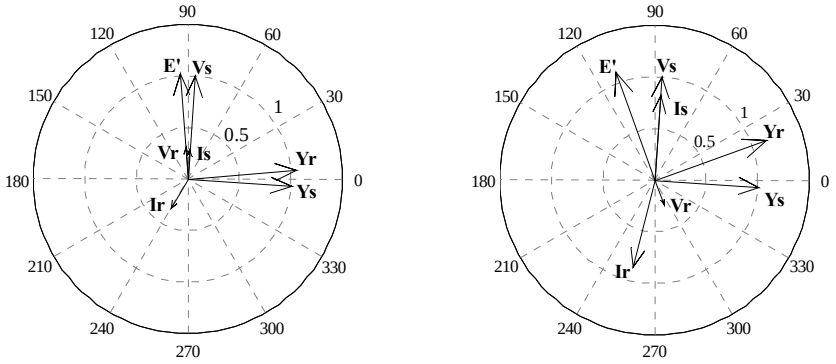

Figure 5.7: Space-phasor diagram of the DFIG operating at unity stator power factor: (a) subsynchronous operation, V_w = 7 m/s; (b) supersynchronous operation, V_w = 12 m/s.

The power flows and power losses incurred in the back-to-back converter are given in Table 5.11 in real values, MW and MVAr. The power losses are broken down into RSC and GSC losses for the various simulated scenarios; the total losses $P_{loss,b\text{-}b}$ (%) of the B-B converter (given in percentage) with respect to its nominal power are also provided.

Since the stator is operated at unity power factor, in the subsynchronous operation mode, active and reactive powers are absorbed through the rotor, whereas in the supersynchronous operation mode, the opposite case occurs since the active and reactive powers are generated. As expected, in both operating modes, the active power is being delivered through the stator and no reactive power is being produced or consumed at the stator's terminals.

Table 5.11: DFIG's power flows for different wind speeds

Results	Wind speed (m/s)					
	7	8	9	10	11	12
	Subsynchronous operation			Supersynchronous operation		
P_e	0.39667	0.59250	0.84322	1.15532	1.53514	1.98897
Q_e	0.61175	0.59632	0.57678	0.55279	0.52411	0.49057
P_{qs}	0.56169	0.73293	0.92584	1.14066	1.37789	1.63586
Q_{gs}	0.00000	0.00000	0.00000	0.00000	0.00000	0.00000
P_{qr}	-0.16178	-0.13684	-0.07852	0.01957	0.16347	0.36148
Q_{qr}	-0.11078	-0.08177	-0.04111	0.02008	0.11367	0.25628
P_g	0.16502	0.14043	0.08262	-0.01465	-0.15725	-0.35311
Q_q	-0.61175	-0.59632	-0.57678	-0.55279	-0.52411	-0.49057
P_{swr}	0.00022	0.00034	0.00052	0.00076	0.00109	0.00152
P_{swq}	0.00229	0.00214	0.00194	0.00175	0.00171	0.00209
$P_{loss,rsc}$	0.00089	0.00139	0.00212	0.00312	0.00447	0.00623
$P_{loss,gsc}$	0.00235	0.00219	0.00199	0.00179	0.00175	0.00214
$P_{loss,b\text{-}b}$	0.46313	0.51292	0.58637	0.70163	0.88935	1.19571

From the results presented for the rotor currents in Table 5.10, it can be seen that its magnitude increases as the wind speed does it. This tendency is mirrored in the computed values for the switching losses of the RSC, recalling that P_{swr} is a function of the current leaving/entering to its terminals. By the same token, the overall losses $P_{loss,rsc}$ follows the same trend. On the other hand, this simulation shows that the power losses related to the operation of the GSC are very similar in magnitude. This can be justified when we look at the total apparent power leaving/entering the GSC, $|\boldsymbol{S}_g| = sqrt(P_g^2 + Q_g^2)$, which does not change drastically for the various simulated scenarios of wind speed.

Since more apparent power is flowing through the GSC compared to the RSC, more power losses are incurred in the GSC for every wind speed condition. Furthermore, the minimum power loss incurred in B-B converter $P_{loss,b\text{-}b}$ is encountered when the wind speed has its lowest value and higher power losses appear as the wind speed increases. Note that the overall maximum power losses reached 1.19571% for a wind speed of 12 m/s.

Having analyzed the DFIG from the steady-state standpoint, it is now feasible to carry out time domain simulations to evaluate its performance in the event of changes either in the wind speed or in the network. To this end, assuming that the wind generator is initially operating at a wind speed of V_w = 12 m/s, the sequence of simulated events is the following: (i) at time t = 0.5s, the wind speed changes to V_w = 10 m/s; (ii) at time t = 1.0s, the wind speed decreases again to a value of V_w = 8 m/s; (iii) at time t = 1.5s, the wind speed rises to its initial value of V_w = 12 m/s. The simulation runs for 3s, the selected time step is 1ms and the tolerance used is 10^{-6}.

Arguably, this scenario evaluates a realistic sequence of events that occurs in the real-life operation of wind turbines. Habitually, they are subjected to sudden changes in its primary energetic source owing to the stochastic nature of the wind. Clearly the wind variations lead the wind generators to run at different operating points which in the case of DFIGs are optimal for the sake of extracting the maximum available amount of energy from the wind. Hence, changes in the wind speed lead to changes in the mechanical torque, which in turn, are reflected in the stator powers as well as in the rotor powers. By the same token, some fluctuations are expected in the variables associated with the network, that is, voltage magnitude and voltage angle, as shown in Figure 5.8 and Figure 5.9. In this scenario, such voltage variations are negligible; it is fair to state that in practice, these voltage variations do not endanger the power system daily operation.

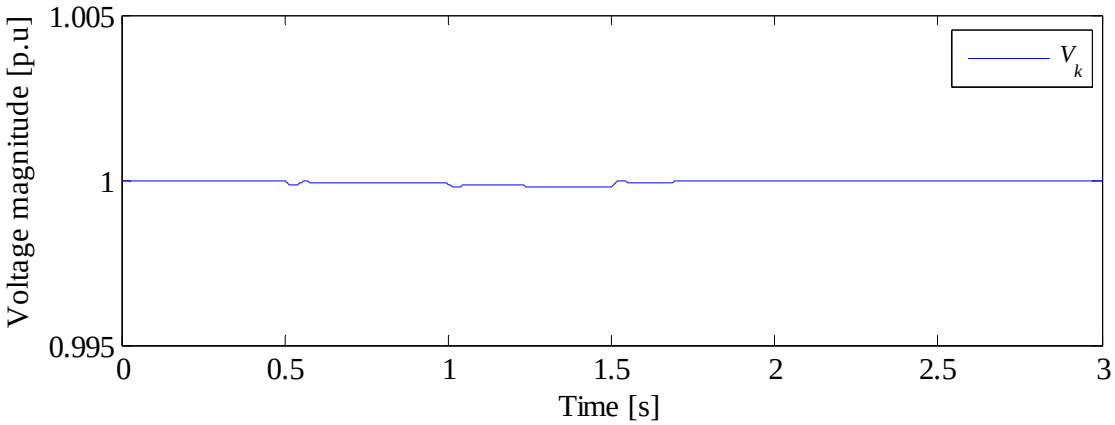

Figure 5.8: Voltage performance at the DFIG's network bus.

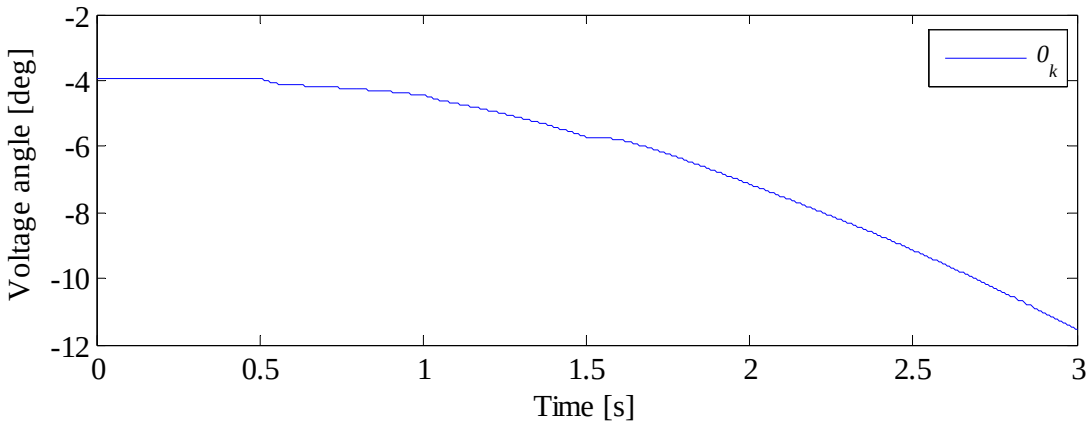

Figure 5.9: Voltage angle performance at the DFIG's network bus.

Figure 5.10 and Figure 5.11 show the active and reactive power dynamic behavior, respectively, at stator's and rotor's terminals, where it must be remarked that the wind generator is driven smoothly to the new operating conditions. Owing to the physical arrangement of the converters, only the active power oscillations at the rotor's terminals are spread to the DC link in the form of voltage variations. The voltage performance at the stator terminals is not only influenced by the power variations in the stator, but also it is slightly affected by the DC link voltage fluctuations because the reactive power injected/consumed by the GSC depends on it among other variables.

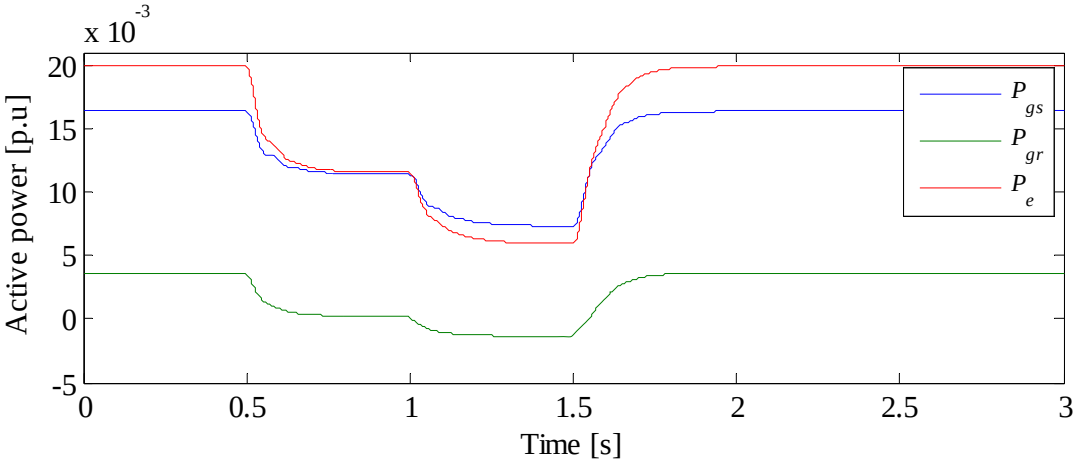

Figure 5.10: Stator active power, rotor active power and total active power.

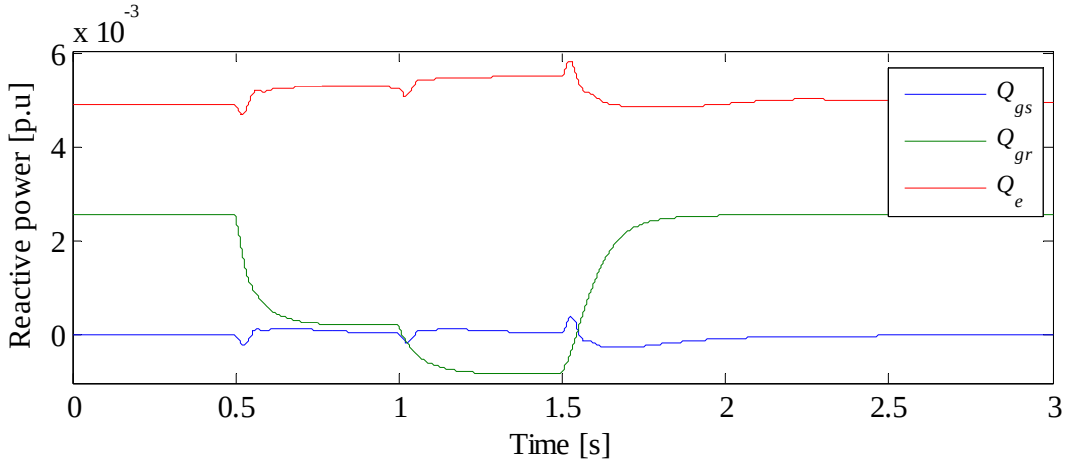

Figure 5.11: Stator reactive power, rotor reactive power and total reactive power.

At the beginning the wind generator is operating at 12 m/s which corresponds to T_m = -0.82964 p.u and ω_m = 1.23483 p.u; once the wind speed has been decreased first to 10 m/s and then to 8 m/s, it is expected a reduction in both, the torque magnitude and in the mechanical speed, as shown in Figure 5.12 and Figure 5.13, respectively. This dynamics are also reflected in the electromotive forces shown in Figure 5.14, E'_d and E'_q, which are related with the magnetic fluxes in the rotor. This obliges the DFIG to find different optimal operating points according to the new wind speed conditions, regulating the rotor voltages in a very effective manner so as to rapidly damp out the existing oscillations, as can be seen in Figure 5.15. Note that at the end of the simulation, the computed variables return approximately to their initial values given that the last simulated event was to assume that the wind speed also returns to its original value.

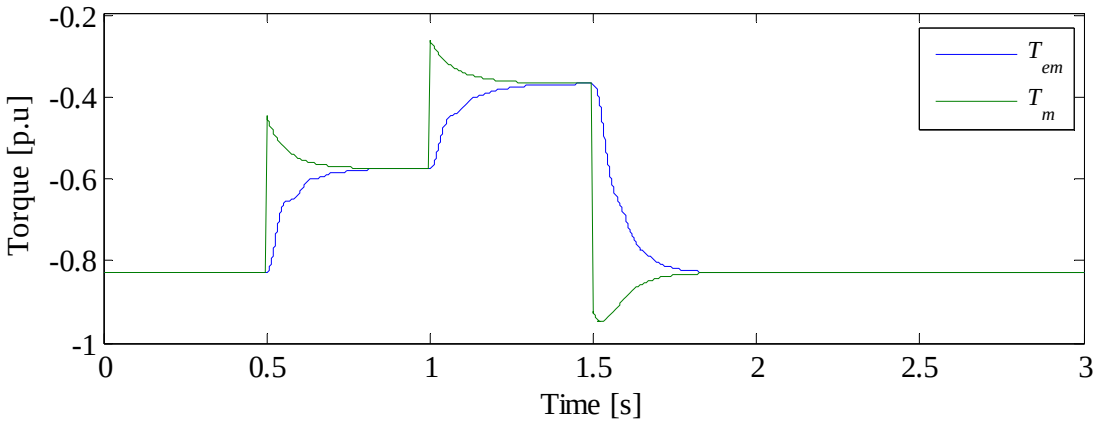

Figure 5.12: Electromagnetic and mechanical torque of the DFIG.

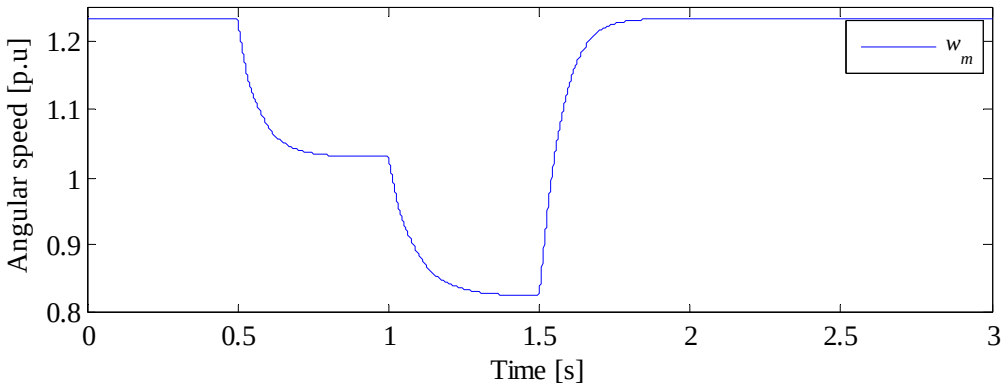

Figure 5.13: Mechanical speed of the DFIG.

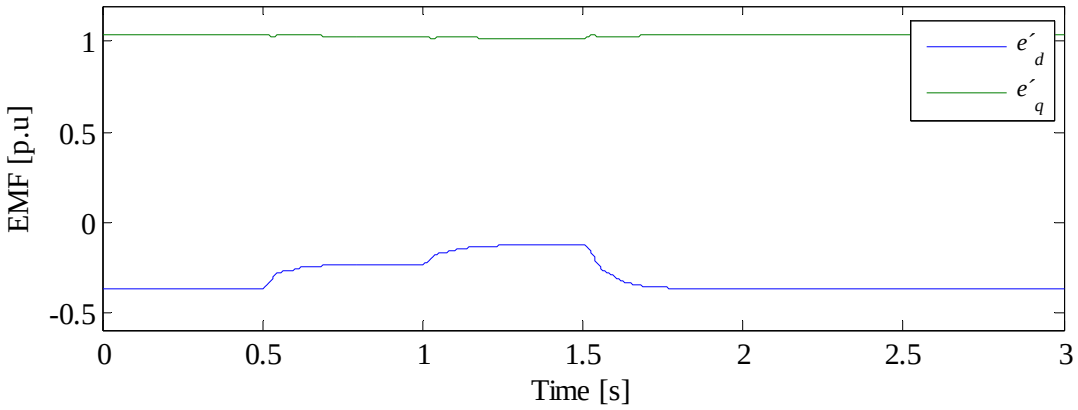

Figure 5.14: E.M.F of the DFIG.

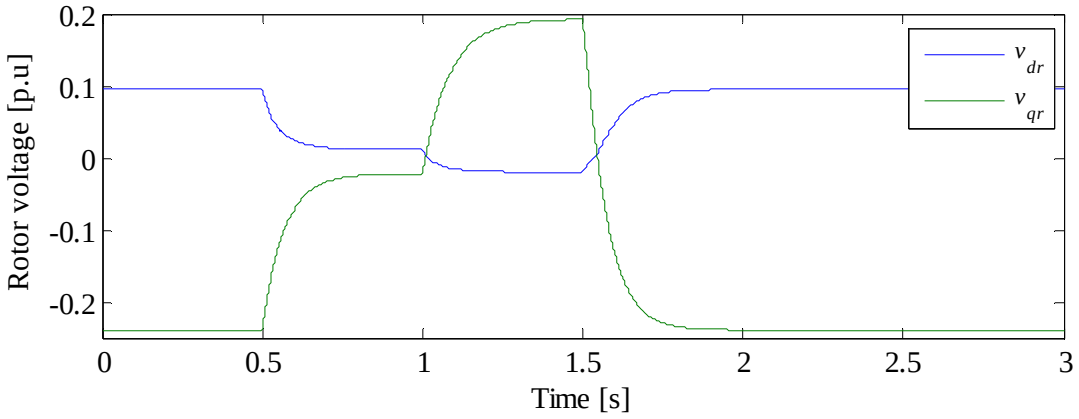

Figure 5.15: Rotor voltages of the DFIG.

When the rotor powers start to vary, the equilibrium of power in the DC link is broken, resulting in oscillations of the voltage at the DC side of the B-B converter depicted in Figure 5.16. One has to bear in mind that this voltage is being controlled by means of a dynamic controller that acts over the dc current flowing through the DC link. Such controller operates very effectively since the voltage oscillations are damped out after a few milliseconds of applying each disturbance.

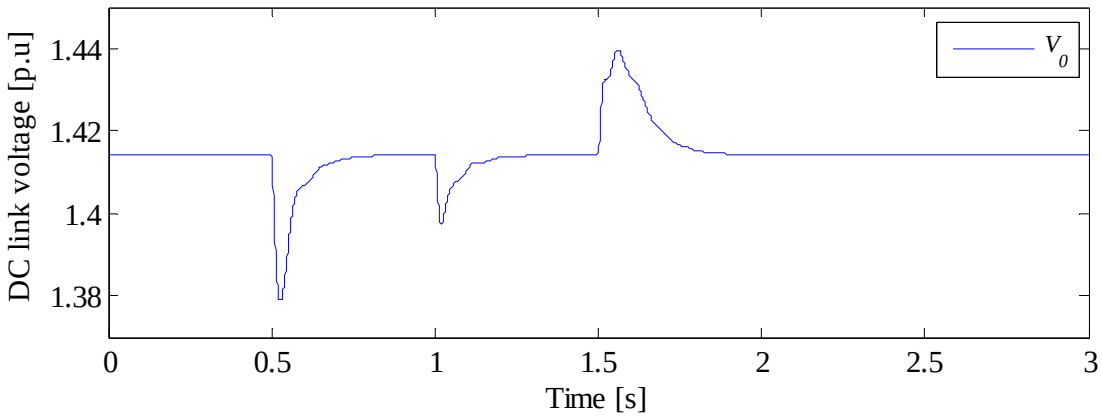

Figure 5.16: Voltage performance at the DC link of the B-B converter.

From Figure 5.17 and Figure 5.18 it is seen that the modulation index m_{ar} along with the phase-shifting angle ϕ_r suffer drastic variations so as to provide the proper rotor voltage values with which the wind generator will arrive at the optimum operating point dictated by the MPT curve. On the other hand, since the GSC is responsible for maintaining the DC

voltage and, at the same, to deal with voltage variations at the system's bus, the modulation index m_{ag} and the phase-shifting angle ϕ_g are dynamically adjusted, as shown in Figure 5.19 and Figure 5.20, to help keep the network's voltage at the specified value and to permit the flow of active power coming from the DC link (for supersynchronous operation) to the grid. Note how different is the dynamic performance of the phase-shifting angles for both the GSC and RSC; the former follows the same trend as the nodal voltage angle of the network shown in Figure 5.9, whereas the latter is purely adjusted to create the necessary rotor voltages.

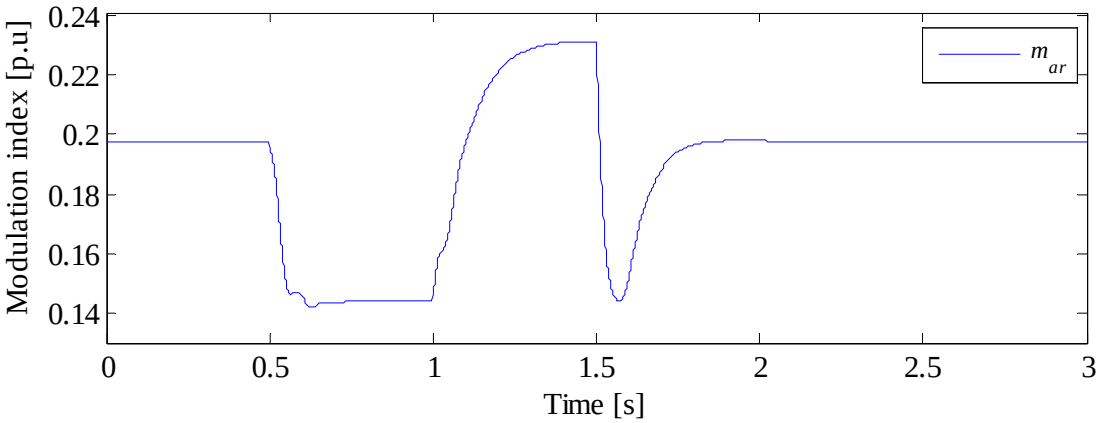

Figure 5.17: Modulation index of the RSC.

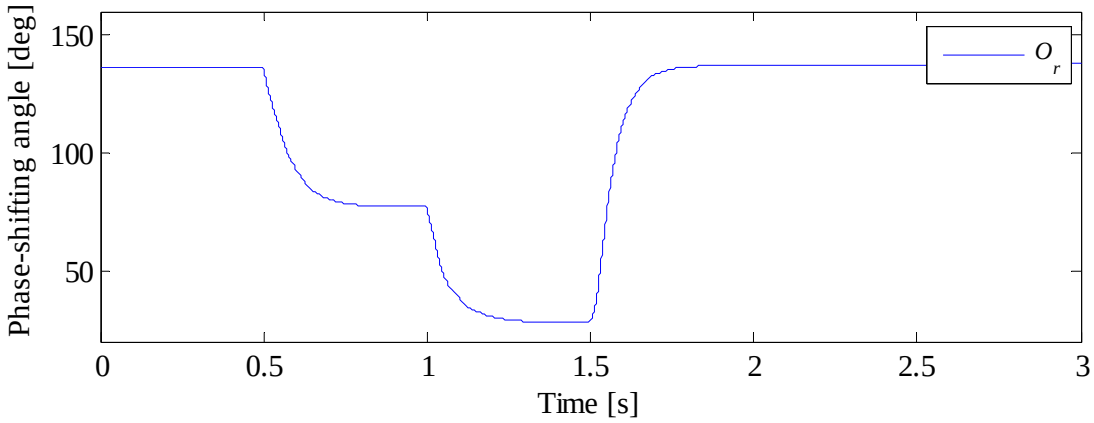

Figure 5.18: Phase-shifting angle of the RSC.

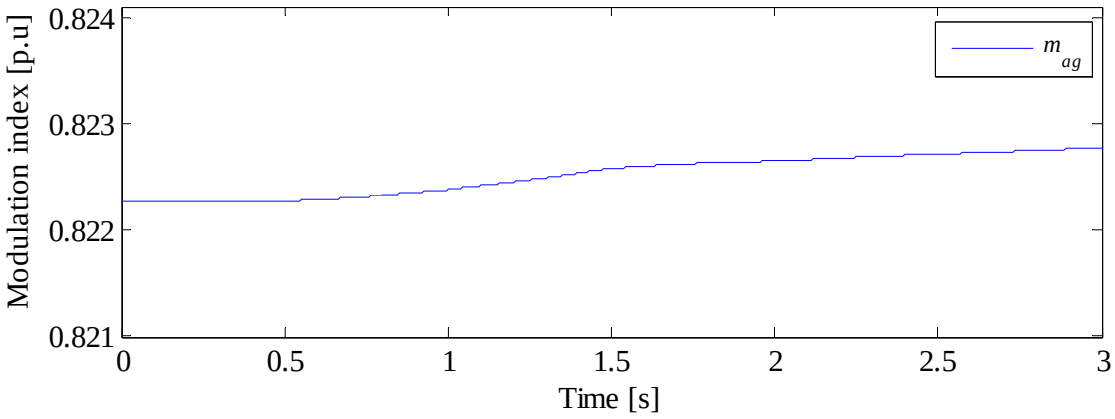

Figure 5.19: Modulation index of the GSC.

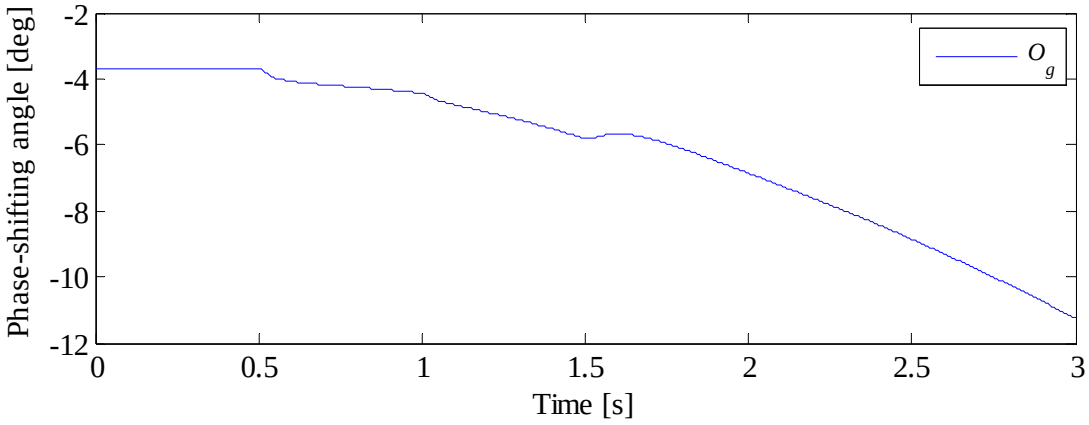

Figure 5.20: Phase-shifting angle of the GSC.

5.4.2 IEEE 30-bus network, 5 DFIGs

The new DFIG model has been tested in the IEEE-30 bus network. In this case, five wind generators are distributed in the grid operating at their nominal wind speed V_w = 12 m/s. The scheduled voltage for the wind generators connected at buses 23, 24 and 26 is 1.025p.u, whereas those embedded at nodes 29 and 30 are exerting voltage control at 1.0p.u. The reference value of reactive power for every machine's stator is assumed to be $Q_{gs,ref}$ = 0, which corresponds to $cos(\varphi)$ = 1.

The relevant outcomes as given by the power flow solution are presented in Table 5.12; V_k and V_r stand for the voltage magnitude at network's terminals and rotor's terminals, respectively; $P_{loss,rsc}$ and $P_{loss,gsc}$ represent the power losses incurred in the RSC and GSC, respectively.

Table 5.12: Results obtained for the steady-state regime for the various DFIGs

Bus	V_k (p.u)	m_{ag}	V_r (p.u)	m_{ar}	P_e (MW)	Q_e (MVAr)	$P_{loss,rsc}$ (MW)	$P_{loss,gsc}$ (MW)
23	1.025	0.83560	0.26213	0.19866	1.99294	-0.11919	0.00595	0.00078
24	1.025	0.83737	0.26213	0.19866	1.99301	0.03589	0.00595	0.00071
26	1.025	0.84246	0.26213	0.19866	1.99172	0.48331	0.00595	0.00200
29	1.000	0.81269	0.25736	0.19736	1.98973	-0.33122	0.00623	0.00138
30	1.000	0.81669	0.25736	0.19736	1.99037	0.01272	0.00623	0.00074

Observe that the power losses computed for the RSC are the same for those wind generators operating at the same voltage level. The marginal affectation of the terminal voltage on the $P_{loss,rsc}$ relies on the different magnetization current that is needed to operate the stator at the required reactive power setpoint. On the other hand, the power losses incurred in the GSC vary from one wind generator to another without any evident pattern since the total apparent power injected to the grid via this converter varies in accordance with the necessary reactive power requirements Q_e to uphold the target voltage value V_k.

As shown in Figure 5.21, the wind generators have been located in a highly loaded area from which the synchronous generators are relatively far, electrically speaking. By this token, a simultaneous disconnection of the transmission line connecting buses 22-24 and the transformer connected between buses 27-28 leave the wind generators embedded to the grid via a radial system. This leads to changes in voltages and powers all over the network. Such disturbance occurs at t = 0.5s, the simulation runs for 3s and the tolerance used is 10^{-6}. The relevant system data is presented in the Appendix D. Note that this type of perturbation differs from the one employed in the first test case where a mechanical perturbation was applied to the wind generators by modifying the wind speed, that is, the mechanical torque; in this occasion the objective is to study the performance of the DFIGs in view of disturbances in their electrical variables such as variations in their terminal voltage magnitude and angle.

Owing to the tripping of the two transmission lines, the voltages in the load area begin to decrease. Such voltage drops are seen differently at each node where the DFIGs are connected; leading the DFIG controllers to cope with the perturbation by adjusting the network's voltages, the rotor voltages and the DC link voltages so as to maintain them operating stably, as can be seen in Figure 5.22 to Figure 5.24, respectively. At the steady-state operating regime, all the DFIGs were able to uphold their corresponding target voltage value. However, in the dynamic regime the situation was different for all the DFIGs except for the one connected at bus 23 since their reactive power reserve were depleted and consequently were driven to operate at the offended limit.

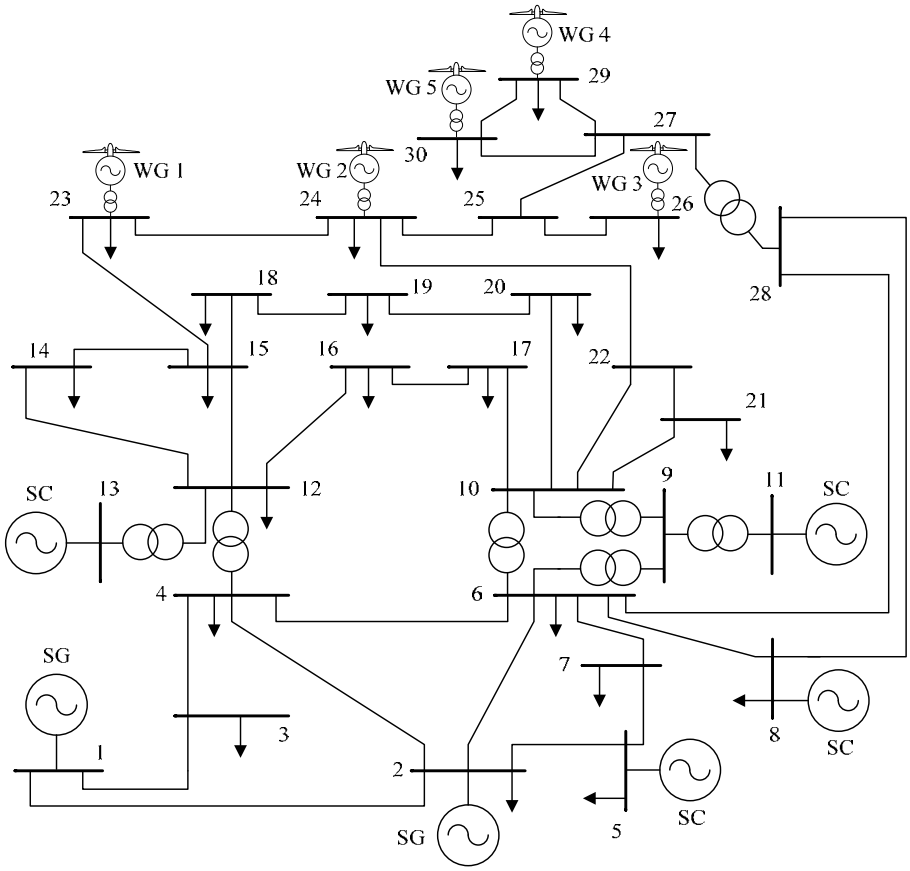

Figure 5.21: Modified IEEE 30-bus network to integrate five DFIGs.

It is worth recalling that the limit is checked based on the current magnitude and not on the reactive power injection. This has more practical value given that the main limiting factor in VSCs is the current flowing through the electronic switches.

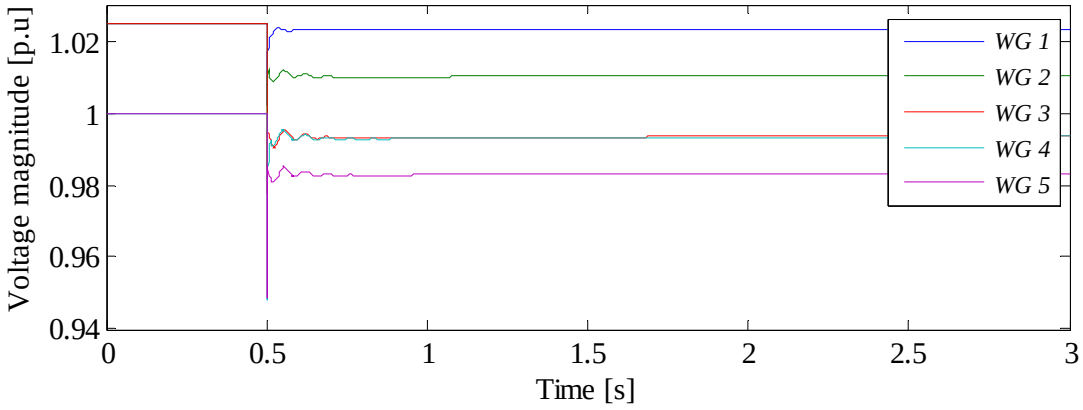

Figure 5.22: Voltage performance DFIGs' network connection.

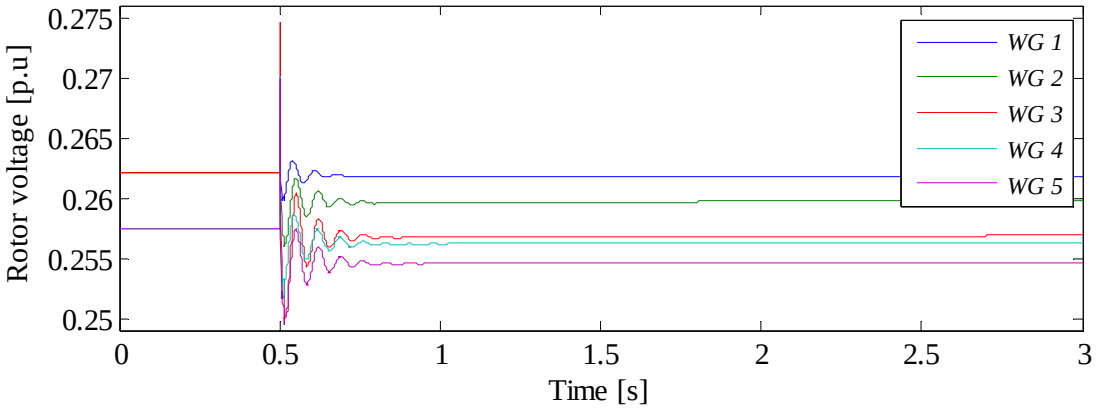

Figure 5.23: Voltage performance at the rotor side of the DFIGs.

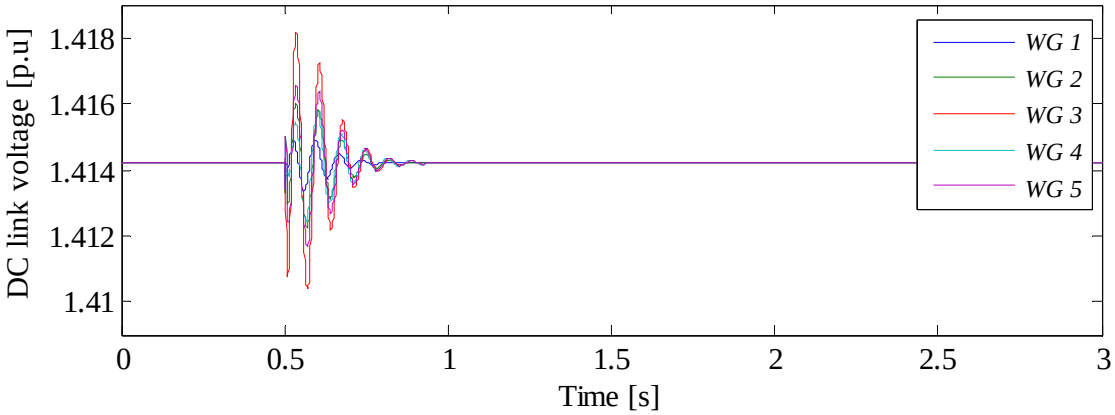

Figure 5.24: DC voltage performance of the DFIGs.

Note that the nature of the voltage dynamics at the various points of the DFIGs is different. To begin with, the voltage dynamics at the AC network side is determined not only by the controllers of the DFIG working for providing reactive power support to the grid, but also it depends on the rest of the synchronous generators and their controllers taking part in the grid's disturbance. Generally speaking, the voltage recovery at the AC side differs compared to those of the DC link and rotor circuit owing to the time constants of the dynamic controllers for the DC link and RSC. The very fast dynamics of the RSC are also reflected in the modulation index m_{ar}; the reactive current control loop for the GSC shown in Figure 4.11 is responsible for controlling the terminal voltage and the modulation index m_{ag} controller only brings additional support. This explains, to a greater or lesser extent, the difference between the dynamic performances for both modulation indices presented in Figure 5.25 and Figure 5.26. Arguably, the dynamic controllers associated with both converters may be seen

as current controllers, where the RSC controllers act over the rotor currents of the induction machine and the GSC's regulate the active and reactive currents being fed to the grid.

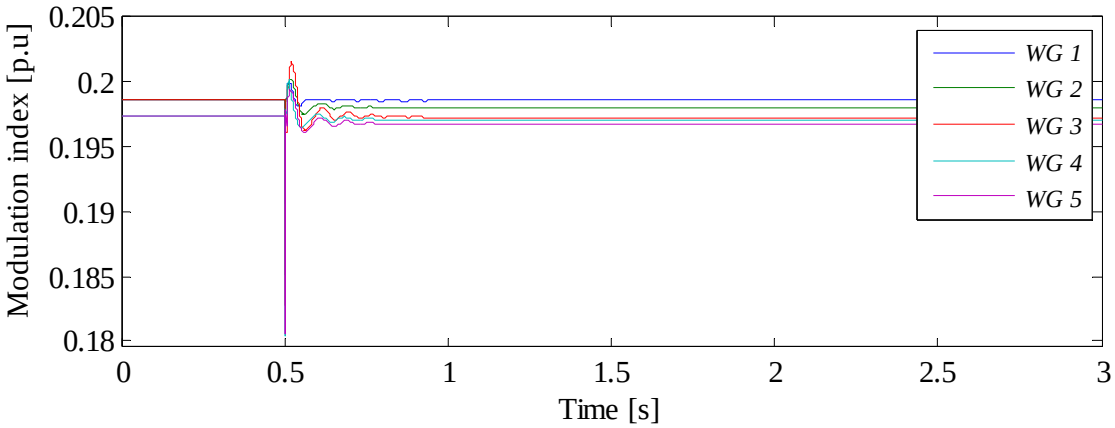

Figure 5.25: Modulation index of the RSC.

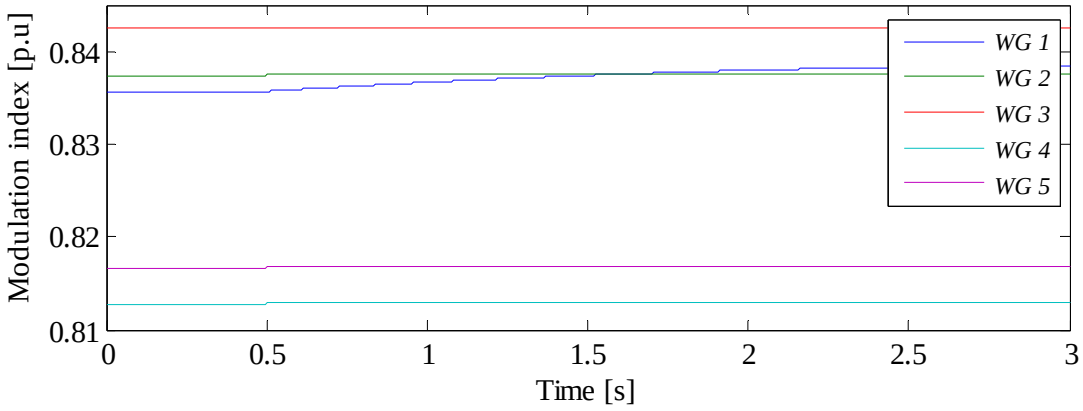

Figure 5.26: Modulation index of the GSC.

The active and reactive powers injected to the network are of interest when performing time domain simulations of power networks. The total generated active and reactive powers as well as the total power losses incurred in the B-B converter are shown in Figure 5.27 to Figure 5.29, respectively. Note how fast the oscillations of the active power are damped out. Likewise, the reactive power at each DFIG is rapidly adjusted so as to provide voltage support. It should be brought to attention that the reactive powers of the wind generators two to five, Q_{e2} - Q_{e5}, were kept at a fixed value after a short time of the occurrence of the disturbance since their maximum current magnitude were exceeded. The remaining DFIGs kept on regulating their reactive power injection so as to comply with its initial voltage setpoint.

When the disturbance is applied in the network and the voltage drops at the DFIG's terminals, the rotor controllers start to act in order to bring the machine back to its initial operating state. Hence, the rotor currents begin to deviate from their steady-state values causing also variations in the power losses in the converters. As mentioned previously in Chapter 4, the mathematical formulation of the DFIG aids to determine the power losses of the B-B converter. From Table 5.12, it can be seen that the wind generator that presents more losses is the number three, whereas the number two has the smallest power losses for the steady state. In Figure 5.29 we can observe that the power loss peak reached by the wind generator number three surpasses the rest of the wind generators. This is somehow consistent with the rest of the plots presented in this case study since this wind generator suffers the strongest oscillations.

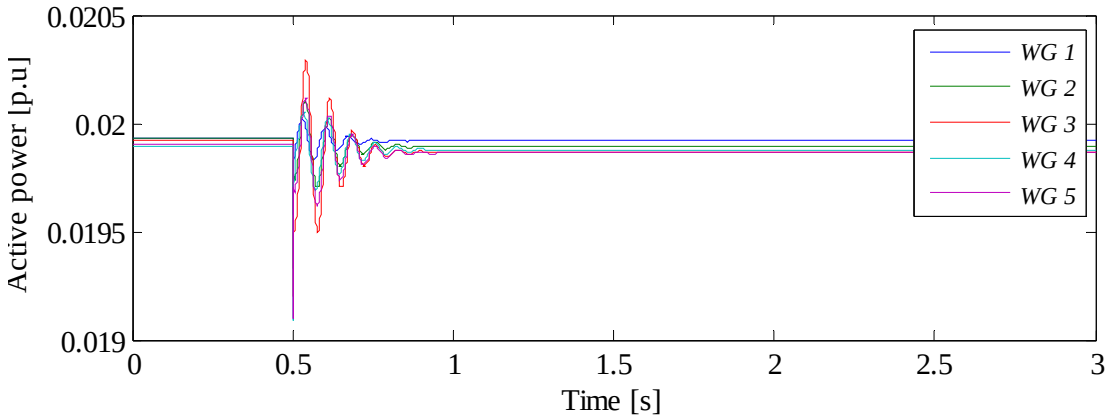

Figure 5.27: Active power generated by the DFIGs.

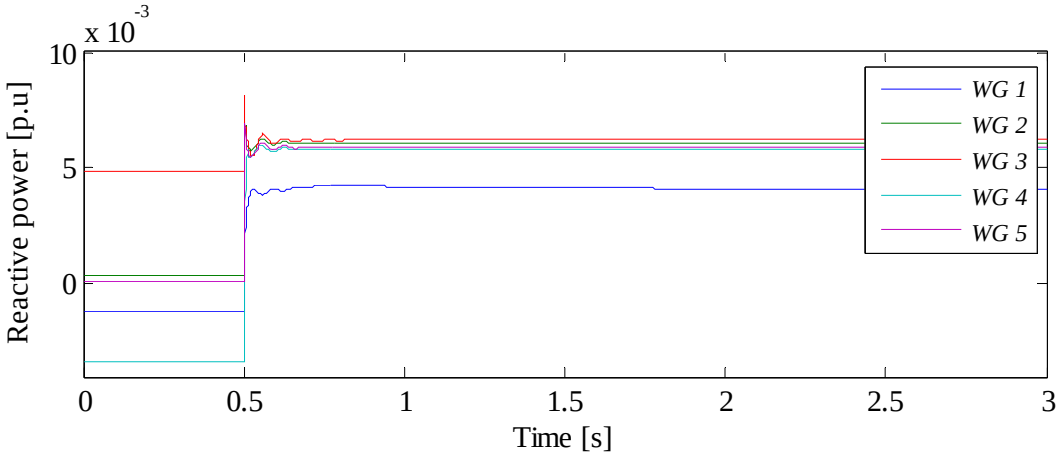

Figure 5.28: Reactive power generated by the DFIGs.

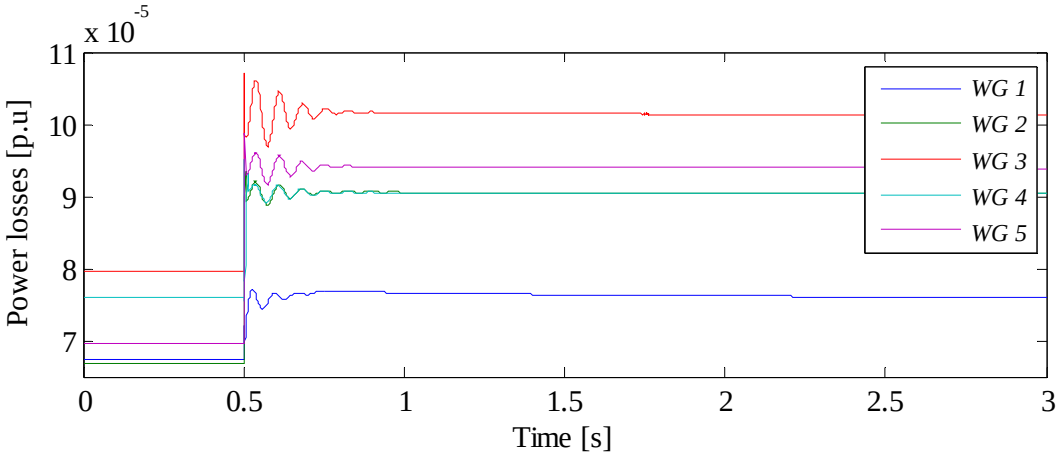

Figure 5.29: Total power losses incurred in the back-to-back converter.

5.5 Conclusions

In this Chapter, the proposed wind generator models have been put through their paces in order to demonstrate their suitability when solving power networks containing wind power generation. These models have been developed in such a way that they combine on well with the model of the power network, including the models of synchronous generators. The simulation results show that the VSWG wind farms do contribute to the system's frequency support in the presence of load/generation disturbances, a conclusion that was possible to arrive at with the use of the newly implemented PFALFC algorithm, within the context of wind power generation. The new DFIG model for steady-state and dynamic simulations has brought about unrivalled modelling flexibility, furnishes information on values of key states variables such the amplitude modulation indexes and the calculations of power losses during both steady-state and operating regimes. It should be remarked that the steady-state model serves also the purpose of deriving initial conditions for the dynamic simulations. The DFIG model has been proven to be reliable for the purpose of reactive power support and for controlling the rotor voltages which are responsible for machine stabilization.

Chapter 6

GENERAL CONCLUSIONS AND FUTURE RESEARCH WORK

6.1 General conclusions

This research work has addressed the timely issue of wind parks modelling and simulation, with particular reference to the modelling of wind power generators for the purpose of steady-state and dynamic operating regimes. From the outset, mathematical models for the most popular types of wind power generators were developed for the purpose of solving fundamental frequency, positive-sequence power networks containing wind turbines. In order to encapsulate their most fundamental characteristics, very few assumptions have been made, resulting in both wind generator and entire wind farm models with a great degree of detail. These detailed models permit to assess not only the impact of the wind farm on the network, but also the inner behaviour of the wind farm itself could be evaluated if desired.

Three types of directly grid-connected wind generators are addressed in this thesis. The main characteristics of design and operability, as function of their construction and control methods for energy capture, are reflected in the derived mathematical models, namely, the fixed-pitch, pitch-regulated and semi-variable speed wind turbines. The three-phase induction machine is the most widely-used rotating machine in wind power industry. The nature of its asynchronous operation coming from the slip between its mechanical speed and the stator's electromagnetic field is determined using a comprehensive steady-state model of the asynchronous generator for the sake of obtaining accurate results. Hence, the active and reactive powers injected to the grid are functions of the machine's slip. On the other hand, two types of variable-speed wind generators have recently received considerable research attention, namely, the DFIG and the PMSG. Following this line of research, these generators are formulated in a rather simple manner, taking advantage of their enhanced power control capability brought about by the power converters that play a crucial role in the wind turbine response. From the power flow algorithm standpoint, these models are regarded

as conventional *PQ* or *PV* models depending upon their reactive power capabilities. The applicability of all the developed wind generator models in practical power networks has been thoroughly investigated with electrical networks of different size.

The need of knowing in advance how the new electrical equipment will impact the power system when embedded in the network motivates researchers to develop upgraded models for different power system tools. A case in point is this thesis where the development of wind generator mathematical models for the power flow with automatic load/frequency control devices has been given attention. Although this tool has not been fully exploited during the past years, this work has shown that it is indeed very useful in the context of renewable generation-improved power networks. The wind generator models aimed at conventional power flows were suitably modified in order to be responsive to the phenomena of frequency changes in the power grid. FSWGs were re-formulated to incorporate the natural response that they exhibit to frequency variations whereas VSWGs were endowed with frequency support capabilities (assuming a prior de-loading of the wind turbine) and such characteristics have also been incorporated into its formulation. These models were proven to be valuable when the interest lies on determining the role that wind parks play when power networks face power imbalances. On one hand, since the FSWGs are formulated based on the equivalent circuit of the induction machine, the estimation of the final operating points of wind generators, following the action of the primary frequency regulation carried out by synchronous generators or VSWGs is possible. Likewise, the contribution of VSWGs to frequency regulation can be assessed through these enhanced variable-speed wind turbines considering the prior deloading of their wind turbines; the proper techniques to achieve the desired deloading of wind turbines have been investigated.

A new model for DFIG-based wind generators has been put forward for the purpose of carrying out steady-state and dynamic simulations studies. It comprises a rather comprehensive model of a back-to-back VSC-HVDC link which combines seamlessly with the model of a WRIG, resulting in a DFIG model of unrivalled control flexibility, for the purpose of fundamental frequency, positive-sequence studies. The full control capability of the back-to-back converter is exploited so as to control the rotor voltage and network voltage via the RSC and GSC, respectively, which are connected to a common DC bus. The very well-known stator flux oriented control has been successfully applied to dynamically regulate the torque and reactive power of the machine's stator in a decoupled manner. It was observed that despite of the very different way of modelling the VSCs, the implementation of the dynamic controllers was very straightforward. Furthermore, it is noteworthy that the

innovative representation of each individual converter permits the simultaneous assessment of their key parameters as well as the utilization of the DC bus in an explicit fashion, resulting in a new model of the DFIG with superior modeling flexibility.

The non-linear equations of the various kinds of wind power generators models and the power network model are linearized around a base operating point and solved by iteration using the Newton-Raphson algorithm. Unified iterative solution of the state variables of the wind power generators and the state variables of the power grid, have been put forward for both steady-state and dynamic operating regimes, with the former standing as a power systems application on its own right or as an initializing option for dynamic simulations. The availability of these wind turbine models with which to carry out network-wide studies, are very timely owing to current and future power systems developments worldwide where the accelerated increase of wind penetration seems unabated. These models enable to assess the impact of wind parks on the daily operation of wind power-upgraded power systems in terms of active power controllability, reactive power control and frequency support. The effectiveness of these new models has been thoroughly assessed using a wide range of standard test networks of various sizes and degrees of operational complexity.

6.2 Future research work

The wind power generator models put forward in this thesis have demonstrated their worth and it makes sense to apply these models in different power system applications, such as optimal power flow, state estimation, steady-state voltage stability, small-signal stability and three-phase steady-state and dynamic applications. The modularity in which these models have been formulated should enable their almost direct incorporation in those power system analysis tools. There is a window of opportunities, nevertheless, that ought to be explored in future research work concerning extending the applicability of these models. For instance:

- More often than not, the electric energy generating systems that prevail in existing power networks are hydro and thermal power plants. The wind power penetration around the world is growing, however, due to its almost non-existent costs associated with the wind energy production. In a context of power networks with high levels of wind penetration, it is necessary to investigate how to simultaneously operate in a secure and economic manner the conventional power plants and wind farms in what it could be thought of as hydro-eolic or thermo-eolic coordination.

- Digital tools are necessary for the power system operators and analysts to plan ahead how to deal with problems of diverse nature which appear in the daily operation of power networks. In order to streamline the tasks associated with the network analyses, an adequate ranking of critical contingencies is mandatory. It is envisage that the developed tool of PFALFC including various wind generator mathematical models may be used to discriminate more efficiently which power imbalances endanger, or otherwise, the network's stability.

- The power system operation has as primary objective to guarantee the system's security and profit maximization lies on the background. In an energy market environment, however, is very important to count on suitable tools to ascertain the optimal spinning reserve distribution in electrical networks with distributed wind farms. To this end, the proposed PFALFC is a pertinent tool that could be used.

- There exist relatively small electric systems that are designed to operate in an isolated way. In this regard, the active power generation and its controllability is an important issue that requires a great deal of attention. Since the newly developed DFIG model facilitates the utilization of the DC bus in a straightforward way, upgrading this model to create a hybrid scheme of a DFIG with a battery energy storage system seems to be pertinent for isolated power system applications.

- The participation of wind generators in ancillary services is a matter of current interest. The new DFIG model for dynamic simulations could be easily upgraded to provide frequency support in terms of inertial response, primary and secondary frequency regulation. To accomplish this, it might be necessary to make some modifications to the model in order to be able to respond appropriately in the presence of frequency swells or drops.

- An extension of the DFIG model would be the incorporation of the PFALFC algorithm into this model taking advantage of the fact that this model calculates explicitly the speed of the induction machine which is affected by system frequency deviations.

- It has to be pointed out that the proposed back-to-back converter model comprised in the DFIG could be also used in wind generators that make use of fully-rated converters.

BIBLIOGRAPHY

[Acha et al., 2005]

E. Acha, C.R. Fuerte-Esquivel, H. Ambriz-Perez and C. Angeles-Camacho, "FACTS modeling and simulation in power networks", John Wiley & Sons, 2005.

[Acha and Kazemtabrizi, 2013]

E. Acha and B. Kazemtabrizi, "A new STATCOM model for power flows using the Newton-Raphson method", *IEEE Trans. on Power Systems*, vol. 28, no. 3, pp. 2455-2465, August 2013.

[Ackerman, 2005]

T. Ackerman, "Wind Power in Power Systems", first ed., John Wiley & Sons, England, 2005.

[Akhmatov, 2003]

V. Akhmatov, "Analysis of dynamic behaviour of electric power systems with large amount of wind power," Ph.D. Thesis, Electric Power Engineering, Orsted-DTU, Technical University of Denmark, April 2003.

[Anaya-Lara et al., 2009]

O. Anaya-Lara, N. Jenkins, J. Ekanayake, P. Cartwright and M. Hughes, "Wind energy generation: modelling and control", Wiley, August 2009.

[Barrios-Martinez et al., 2009]

E. Barrios-Martinez, C. Angeles-Camacho, E. Acha and M.A. olguin-Becerril, "Dynamic Phase-domain Modelling and Simulation of STATCOM in Large-scale Power Systems", *IEEE Power Tech Conference 2009*, pp. 1-9, Bucharest 2009.

[Bianchi et al., 2006]

F. D. Bianchi, H. De Battista and R. J. Mantz, "Wind Turbine Control Systems - Principles, Modelling and Gain Scheduling Design", first ed., Springer, Germany, 2006.

[Burnham et al., 2009]

D.J. Burnham, S. Santoso, E. Muljadi, "Variable Rotor-Resistance Control of Wind Turbine Generators", *IEEE PES Gen. Meet.*, pp. 1-6, July 2009.

[Cañizares, 2000]

C. A. Cañizares, “Power flow and transient stability models of FACTS controllers for voltage and angle stability studies”, *IEEE PES Winter Meeting 2000,* vol. 2, pp. 1447-1454, 2000

[Cate and Gelopulos, 1984]

E. G. Cate and D. P. Gelopulos, “Time frame notion and time response of the models in transient, mid-term and long-term stability programs”, *IEEE Transactions on Power Apparatus and Systems*, vol. PAS-103, no. 1, January 1984.

[Challoo and Nemmers, 2009]

S. Li, R. Challoo and M. J. Nemmers, “Comparative Study of DFIG Power Control Using Stator-Voltage and Stator-Flux Oriented Frames”, *IEEE PES Gen. Meet.,* pp. 1-8, July 2009.

[Chowdhury et al., 2008]

B. H. Chowdhury, H. T. Ma, “Frequency regulation with wind power plants,” in *Proc. 2008 IEEE Power Eng. Soc. General Meeting*, pp. 1-5.

[Christiansen and Johnsen, 2006]

W. Christiansen and D. T. Johnsen, “Analysis of Requirements in Selected Grid Codes”, Technical University of Denmark (DTU), www.frontwind.com/Analysis%20of%20the %20requirements%20in%20selected%20Grid%20Codes.pdf, January 2006.

[Conroy and Watson, 2008]

J. F. Conroy and R. Watson, “Frequency response capability of full converter wind turbine generators in comparison to conventional generation,” *IEEE Transactions on Power Systems*, vol. 23, no. 2, pp. 649-656, May 2008.

[de Almeida and Peças Lopes, 2007]

R. G. de Almeida and J. A. Peças Lopes, “Participation of doubly fed induction wind generators in system frequency regulation,” *IEEE Transactions on Power Systems*, vol. 22, no. 3, pp. 944-950, Aug. 2007.

[de Almeida et al., 2006]

R. G. de Almeida, E. D. Castronuovo, and J. A. Peças Lopes, “Optimum generation control in wind parks when carrying out system operator requests”, *IEEE Transactions on Power Systems*, vol. 21, no. 2, pp. 718-725, May 2006.

[de Oliveira, 2000]

M. M. de Oliveira, “Power electronics for mitigation of voltage sags and improved control of AC power systems”, Doctoral Dissertation, Royal Institute of Technology (KTH), Sotckholm 2000.

[Divya and Rao, 2006]

K.C. Divya and P.S. Nagendra Rao**,** “Models for wind turbine generating systems and their application in load flow studies”, *Electr. Power Syst. Res*., vol. 76, pp. 844–856, 2006.

[Dommel and Sato, 1972]

H.W. Dommel and N. Sato, “Fast transient stability solutions”, *IEEE Transactions on Power Apparatus and Systems,* vol. PAS-91, pp. 1643-1650, 1972.

[Erlich and Bachmann, 2005]

I. Erlich, U. Bachmann, “Grid Code Requirements Concerning Connection and Operation of Wind Turbines in Germany”, *IEEE PES Gen. Meet.*, vol. 2, pp. 1253-1257, June 2005.

[EWEA, 2013]

Wind in power: 2012 European Statistics, http://www.ewea.org/fileadmin/files/library/publications/statistics/Wind_in_power_annual_statistics_2012.pdf, The European Wind Energy Association EWEA, February 2013.

[Fagan et al., 2005]

E. Fagan, S. Grimes, J. McArdle, P. Smith and M. Stronge, “Grid Code Provisions for Wind Generators in Ireland”, *IEEE PES Gen. Meet.*, vol. 2, pp. 1241- 1247, June 2005.

[Faisal et al., 2007]

S.F. Faisal, A.H.M.A. Rahim and J.M. Bakhashwain, “A Robust STATCOM Controller for a Multi-Machine Power System Using Particle Swarm Optimization and Loop-Shaping”, International Journal of Elec. Com. and Sys. Eng., pp.64-70, 2007.

[Feijóo, 2009]

A. E. Feijóo, “On PQ Models for Asynchronous Wind Turbines”, *IEEE Trans. Power Syst.*, vol. 24, pp.1890-1891, November 2009.

[Feijóo and Cidrás, 2000]

A. E. Feijóo and J. Cidrás, “Modeling of wind farms in the load flow analysis”, *IEEE Trans. Power Syst.*, vol. 15, pp. 110-115, February 2000.

[Fitzgerald et al., 2003]

A. E. Fitzgerald, C. Kingsley Jr., S. D. Umans, “Electric Machinery”, sixth ed., McGraw-Hill, New York, 2003.

[Fuerte-Esquivel et al., 1997]

C.R. Fuerte-Esquivel and E. Acha,"A Newton-type algorithm for the control of power flow in electrical power networks", *IEEE Trans. Power. Syst.*, vol.12, pp. 1474–1480, November 1997.

[Fuerte-Esquivel et al., 2001]

C.R. Fuerte-Esquivel, J. H. Tovar-Hernández, G. Gutiérrez-Alcaraz, F. Cisneros-Torres, Discussion of modeling of wind farms in the load flow analysis, *IEEE Trans. Power. Syst.*, vol. 16, November 2001.

[Hingorani and Gyugyi, 1999]

N. G. Hingorani and L. Gyugyi, "Understanding FACTS: Concepts and Technology of Flexible AC Transmission Systems", Wiley-IEEE Press, 1999.

[Hong-Woo et al., 2010]

K. Hong-Woo, K. Sung-Soo, K. Hee-Sang. "Modeling and control of PMSG-based variable-speed wind turbine", *Electric Power Systems Research*, vol. 80, pp. 46-52, 2010.

[Hwang et al., 2008]

P.I. Hwang, S. J. Ahn and S. I. Moon, "Modeling of the Fixed Speed Wind Turbine Generator System for DTS", *IEEE PES Gen. Meet.*, pp. 1-7, July 2008.

[IEEE, 1968]

IEEE Committee Report, "Computer representation of excitation systems", *IEEE Transactions on Power Apparatus and Systems*, vol. PAS-87, pp. 1460-1464, 1968.

[Jabbari et al., 2011]

M. Jabbari, G. Shahgholian, M. Mahdavian, E. Attarpour and A. Leilaeyoun, "Modeling and Dynamic Analysis of a STATCOM for System Damping Enhancement", *IEEE International Symposium on Industrial Electronics*, pp. 1087-1092, 2011.

[Krause et al., 2002]

P. C. Krause, O. Wasynczuk and S. D. Sudhoff, "Analysis of Electric Machinery and Drive Systems", New York: IEEE Press, 2002.

[Kundur, 1994]

P. Kundur, "Power System Stability and Control", McGraw-Hill, 1994.

[Lei et al., 2006]

Y. Lei, A. Mullane, G. Lightbody and R. Yacamini, "Modeling of the Wind Turbine With a Doubly Fed Induction Generator for Grid Integration Studies", *IEEE Transactions on Energy Conversion*, Vol. 21, No. 1, March 2006.

[Li and Chen, 2008]

H. Li and Z. Chen, “Overview of different wind generator systems and their comparisons”, *IET Renew. Power Gener.*, Vol. 2, No. 2, pp. 123-138, 2008.

[Li and Haskew, 2009]

S. Li and T. A. Haskew, “Energy Capture, Conversion, and Control Study of DFIG Wind Turbine under Weibull Wind Distribution”, *IEEE PES Gen. Meet.*, pp. 1-9, July 2009.

[Liu et al., 2008]

Y. Liu, W. Wang, L. Xu1, P. Ni and L. Wang, “Research on Power Flow Algorithm for Power System Including Wind Farm”, *IEEE Intern. Conf. on Electrical Machines and Syst. ICEMS*, pp. 2551-255, October 2008.

[Mahdavian et al., 2011]

M. Mahdavian and G. Shahgholian, “Effect of STATCOM on Enhancing Power System Dynamic Stability”, *IEEE International Conference on Elect. Eng., Comp., Telec., And Inf. Tech (ECTI)*, pp. 780-783, 2011.

[Merabet et al., 2011]

A. Merabet, J. Thongman and J. Gu, “Torque and pitch angle control for variable speed wind turbines in all operating regimes”, *IEEE International Conference on Env. And Elect. Eng. (EEEIC)*, pp. 1-5, May 2011.

[Morren et al., 2006]

J. Morren, J. Pierik, S. W.H. de Haan, “Inertial response of variable speed wind turbines,” *Electric Power Systems Research*, vol. 76, no.11, pp. 980–987, July 2006.

[Moutis et al., 2009]

P. Moutis, E. Loukarakis, S. Papathanasiou, and N. D. Hatziargyriou, “Primary load-frequency control from pitch-controlled wind turbines,” in *Proc. 2009 IEEE PowerTech, Bucharest*, pp. 1-7.

[Muljadi et al., 1998]

E. Muljadi, K. Pierce and P. Migliore, “Control Strategy for Variable-speed, Stall-regulated Wind Turbines”, National Renewable Energy Laboratory NREL, *American Controls Conference*, Philadelphia, PA, June 1998.

[Okamura et al., 1975]

W. Okamura, Y. Oumar, S. Hayashi, K. Vemura and F. Ishiguro, “A new power flow model and solution method,” *IEEE Transactions on Power Systems*, PAS-94, pp. 1042–1050, May 1975.

[Ortega and Rheinboldt, 2000]

J. M. Ortega, W. C. Rheinboldt,“Iterative Solutions of Nonlinear Equations in Several Variables”, SIAM, Philadelphia, 2000.

[Pena et al., 1996]

R. Pena, J.C. Clare, G.M. Asher, “Doubly Fed Induction Generator Using Back-to-Back PWM Converters and its Application to Variable-Speed Wind-Energy Generation”, *IEE Proc. Electr. Power Appl.*, Vol. 143, No 3, May 1996.

[Price and Sanchez-Gasca, 2006]

W. W. Price, J. J. Sanchez-Gasca, “Simplified Wind Turbine Generator Aerodynamic Models for Transient Stability Studies”, *IEEE Power Systems Conference and Exposition PSCE*, pp. 986-992, 2006.

[Rafian et al., 1987]

M. Rafian, M.J.H. Sterling and M.R. Irving, “Real-time power system simulation”, *IEE Proceedings Generation, Transmission and Distribution*, vol. 134, pp. 206–223, May 1987.

[Ramtharan et al., 2007]

G. Ramtharan, J.B. Ekanayake and N. Jenkins, “Frequency support from doubly fed induction generator wind turbines”, *IET Renewable Power Generation*, vol. 1, no 1, pp. 3-9, March 2007.

[SENER, 2012]

Department of Energy SENER, http://www.sener.gob.mx/portal/Default.aspx?id=2332, Renewable energy potential in Mexico, November 2012.

[SENER, 2013]

National Electric Sector, http://sie.energia.gob.mx/, Energy Information System - Department of Energy SENER 2013, Mexico.

[Shahgholian et al., 2011]

G. Shahgholian, M. Mahdavian, A. Etesami, S. Moalem and M. Jabbari “Improvement of Dynamic Behavior and System Stability by Using STATCOM”, *IEEE International Symposium on Industrial Electronics*, pp. 1057-1062, 2011.

[Slootweg et al., 2003]

J. G. Slootweg, H. Polinder, and W. L. Kling, “Representing wind turbine electrical generating systems in fundamental frequency simulations,” *IEEE Transactions on Energy Conversion*, vol. 18, no. 4, pp. 516-524, Dec. 2003.

[Smed et al., 1991]

T. Smed, G. Andersson, G.B. Sheble and L.L. Grigsby, “A new approach to AC/DC power flow”, *IEEE Trans. Power. Syst.*, vol. 6, pp. 1238–1244, August 1991.

[Teninge et al., 2009]

A. Teninge, C. Jecu, D. Roye, S. Bacha, J. Duval, R. Belhomme, “Contribution to frequency control through wind turbine inertial energy storage,” *IET Renewable Power Generation*, vol. 3, no 3, pp. 358–370, March 2009.

[Traub, 1964]

J. F. Traub,“Iterative Methods for the Solution of Equations”, Prentice Hall, New Jersey, 1964.

[Ugalde-Loo et al., 2013]

C.E. Ugalde-Loo, J.B. Ekanayake and N. Jenkins, “State-Space Modeling of Wind Turbine Generators for Power System Studies”, *IEEE Transactions on Industry Applications*, vol. 49, pp. 223-232, 2013.

[Wang and Crow, 2011]

K. Wang and M.L. Crow, “Power System Voltage Regulation via STATCOM Internal Nonlinear Control” ”, *IEEE Transactions on Power Systems*, vol. 26, pp. 1252-1262, 2011.

[WWEC, 2013]

World Wind Energy Report 2012, http://www.wwindea.org/webimages/WorldWind EnergyReport2012_final.pdf, XII World Wind Energy Conference & Renewable Energy Exhibition WWEC 2013, Havana, Cuba, June 2013.

[Zavadil and Smith, 2005]

R.M. Zavadil and J.C. Smith, “Status of Wind-Related US National and Regional Grid Code Activities”, *IEEE PES Gen. Meet.*, vol. 2, pp. 1258- 1261, June 2005.

[Zou et al., 2011]

Y. Zou, M. Elbuluk and Y. Sozer, “Stability Analysis of Maximum Power Point Tracking (MPPT) Method in Wind Power Systems”, *IEEE Industry Applications Society Annual Meeting (IAS)*, October 2011.

Appendix A

Convergence characteristics of the Newton-Raphson method

A.1 Newton-Raphson method

The Newton-Raphson algorithm is a powerful technique for numerically solving a set of algebraic nonlinear equations. Local quadratic convergence toward the solution is achieved if the initial guess x_0 lies in the basin of attraction of the solution point and the nonlinear functions are sufficiently smooth, as shown in Figure A.1(a) for the case of a single monovariable nonlinear function. This method derives from the Taylor series expansion of a function $f(x)$ around a base point, as seen in (A.1).

$$f(x+h) \approx f(x) + f'(x) \cdot h + \frac{f''(x)}{2} \cdot h^2 + \ldots \tag{A.1}$$

This method iteratively looks for the solution $f(x+h)=0$ by approximating $f(x)$ by its first-order Taylor approximation and calculating h as: $h \approx -f(x) / f'(x)$. The improved values of the state variable are then given by $x_{i+1} \approx x_i - f(x_i) / f'(x_i)$.

This method possesses some peculiarities that need to be carefully considered in order to ensure its successful application: (i) the derivative of the function must exist, (ii) it is heavily dependent on the initial guess, and (iii) it has poor global convergence characteristics; as illustrated in Figure A.1(b).

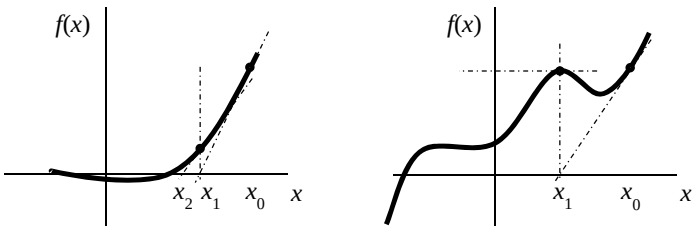

Figure A.1: Non-linear functions: (a) NR finding the root, (b) NR finding a local maxima and then shooting off into negative infinite.

Appendix B

Fixed-speed and semi-variable speed wind generator models

B.1 FSWG model

Based on the steady-state equivalent machine of the induction machine shown in Figure 2.1(b), the equivalent impedance seen from the generators' terminals is $\mathbf{Z}_{eq} = \mathbf{Z}_a + R_1 + jX_1$, where $\mathbf{Z}_a$ corresponds to the equivalent impedance between the rotor and the magnetizing branch and is given by

$$\mathbf{Z}_a = \frac{jX_m\left(R_2/s + jX_2\right)}{R_2/s + j\left(X_2 + X_m\right)} \tag{B.1}$$

$$\mathbf{Z}_{eq} = \frac{R_1\left(R_2/s\right) - X_m X_2 - X_1\left(X_2 + X_m\right) + j\left[\left(R_2/s\right)\left(X_1 + X_m\right) + R_1\left(X_2 + X_m\right)\right]}{R_2/s + j\left(X_2 + X_m\right)}. \tag{B.2}$$

The stator current is then determined as

$$\boldsymbol{I}_1 = \frac{\boldsymbol{V}}{\mathbf{Z}_{eq}} = \frac{\left[R_2/s + j\left(X_2 + X_m\right)\right]\boldsymbol{V}}{R_1\left(R_2/s\right) - X_m X_2 - X_1\left(X_2 + X_m\right) + j\left[\left(R_2/s\right)\left(X_1 + X_m\right) + R_1\left(X_2 + X_m\right)\right]} \tag{B.3}$$

which is squared and shown in rearranged form after some algebraic manipulations in (2.9). Similarly, the rotor current of the induction machine can be found by applying Kirchhoff's current law and is given by

$$\boldsymbol{I}_2 = \frac{jX_m \boldsymbol{V}}{R_1\left(R_2/s\right) - X_m X_2 - X_1\left(X_2 + X_m\right) + j\left[\left(R_2/s\right)\left(X_1 + X_m\right) + R_1\left(X_2 + X_m\right)\right]} \tag{B.4}$$

which is squared and presented in (2.10).

Having defined the stator current, we can now proceed to calculate the active and reactive powers generated by the induction generator as $Q_g = -\operatorname{Im}\left\{\boldsymbol{V}\boldsymbol{I}_1^*\right\}$ and $P_g = -\operatorname{Re}\left\{\boldsymbol{V}\boldsymbol{I}_1^*\right\}$. The resulting expressions of powers are shown in (2.7) and (2.8), respectively.

In addition, the equations (2.7) to (2.10) are presented using the next constants:

$A = R_2^2\left(X_1 + X_m\right)$, $B = \left(X_2 + X_m\right)\left[X_2 X_m + X_1\left(X_2 + X_m\right)\right]$, $C = R_1 R_2$,

$D = X_2 X_m + X_1\left(X_2 + X_m\right)$, $E = R_2\left(X_1 + X_m\right)$, $F = R_1\left(X_2 + X_m\right)$, $H = R_2 X_m^2$, $K = R_1 R_2^2$,

$L = R_1\left(X_2 + X_m\right)^2$, $M = X_m R_2\left(X_1 + X_m\right)$, $N = X_m R_1\left(X_2 + X_m\right)$, $T = R_1 R_2 X_m$,

$W = X_m\left[X_2 X_m + X_1\left(X_2 + X_m\right)\right]$.

B.2 SSWG model

Similarly to the case of the FSWGs, the total equivalent impedance seen from the generators' terminals can be obtained as $\mathbf{Z}_{eq} = \mathbf{Z}_a + R_1 + jX_1$. Yet, in this case we assume that $R_x = R_2/s$, which leads to

$$\mathbf{Z}_a = \frac{jX_m\left(R_x + jX_2\right)}{R_x + j\left(X_2 + X_m\right)} \tag{B.5}$$

$$\mathbf{Z}_{eq} = \frac{R_1 R_x - X_m X_2 - X_1\left(X_2 + X_m\right) + j\left[R_x\left(X_1 + X_m\right) + R_1\left(X_2 + X_m\right)\right]}{R_x + j\left(X_2 + X_m\right)} \tag{B.6}$$

Thus, the stator and rotor currents are determined as

$$\boldsymbol{I}_{1,ss} = \frac{\left[R_x + j\left(X_2 + X_m\right)\right]\boldsymbol{V}}{R_1 R_x - X_m X_2 - X_1\left(X_2 + X_m\right) + j\left[R_x\left(X_1 + X_m\right) + R_1\left(X_2 + X_m\right)\right]} \tag{B.7}$$

$$\boldsymbol{I}_{2,ss} = \frac{jX_m \boldsymbol{V}}{R_1 R_x - X_m X_2 - X_1\left(X_2 + X_m\right) + j\left[R_x\left(X_1 + X_m\right) + R_1\left(X_2 + X_m\right)\right]} \tag{B.8}$$

Both currents are squared and presented in (2.24) and (2.25) after some algebraic manipulation. Additionally, after calculating $Q_{g,ss} = -\mathrm{Im}\left\{\boldsymbol{VI}_{1,ss}^{*}\right\}$ and $P_{g,ss} = -\mathrm{Re}\left\{\boldsymbol{VI}_{1,ss}^{*}\right\}$, the resulting expressions for the reactive and active powers are shown in (2.22) and (2.23), respectively, using the next constants:

$A' = \left(X_1 + X_m\right)$, $C' = R_1$, $E' = \left(X_1 + X_m\right)$, $H' = X_m^2$, $K' = R_1$, $M' = X_m\left(X_1 + X_m\right)$, $T' = R_1 X_m$.

Appendix C

DFIG model for dynamic power system simulations

C.1 Derivation of the WRIG model

The WRIG mathematical model used in this thesis is derived from the fundamental voltage and flux linkage equations of the stator and rotor presented in (4.11) to (4.18). Based on the assumptions stated in Section 4.4, the stator and rotor voltage equations are rearranged as follows:

$$v_{ds} = R_s i_{ds} - \omega_s \psi_{qs} \tag{C.1}$$

$$v_{qs} = R_s i_{qs} + \omega_s \psi_{ds} \tag{C.2}$$

$$\frac{1}{\omega_b}\frac{d\psi_{dr}}{dt} = R_r i_{dr} - (\omega_s - \omega_m)\psi_{qr} - v_{dr} \tag{C.3}$$

$$\frac{1}{\omega_b}\frac{d\psi_{qr}}{dt} = R_r i_{qr} + (\omega_s - \omega_m)\psi_{dr} - v_{qr} \tag{C.4}$$

By solving equations (4.17) and (4.18) for i_{dr} and i_{qr}, respectively, we have

$$i_{dr} = \frac{\psi_{dr} - L_m i_{ds}}{L_{rr}} \tag{C.5}$$

$$i_{qr} = \frac{\psi_{qr} - L_m i_{qs}}{L_{rr}} \tag{C.6}$$

Substituting the above equations for the equations related the fluxes and currents in the stator, namely, (4.15) and (4.16), yields

$$\psi_{ds} = \frac{L_m}{L_r}\psi_{dr} + \left(L_{ss} - \frac{L_m^2}{L_r} \right) i_{ds} \tag{C.7}$$

$$\psi_{qs} = \frac{L_m}{L_r}\psi_{qr} + \left(L_{ss} - \frac{L_m^2}{L_r} \right) i_{qs} \quad . \tag{C.8}$$

Defining $X' = \left(L_{ss} - \frac{L_m^2}{L_r} \right)\omega_s$, $e'_d = -\frac{\omega_s L_m}{L_r}\psi_{qr}$ and $e'_q = \frac{\omega_s L_m}{L_r}\psi_{dr}$, equations (C.7) and (C.8) are redefined as

$$\psi_{ds} = \frac{1}{\omega_s}\left(e'_q + X' i_{ds} \right) \tag{C.9}$$

$$\psi_{qs} = \frac{1}{\omega_s}\left(-e'_d + X' i_{qs} \right) \ . \tag{C.10}$$

By substituting (C.9) and (C.10) into the stator voltage equations, (C.1) and (C.2), we obtain

$$v_{ds} = R_s i_{ds} + e'_d - X' i_{qs} \tag{C.11}$$

$$v_{qs} = R_s i_{qs} + e'_q + X' i_{ds} \tag{C.12}$$

where such equations are solved for i_{ds} and i_{qs} as follows:

$$i_{ds} = \frac{R_s \left(v_{ds} - e'_d \right) + X' \left(v_{qs} - e'_q \right)}{R_s{}^2 + X'^2} \tag{C.13}$$

$$i_{qs} = \frac{R_s \left(v_{qs} - E'_q \right) - X' \left(v_{ds} - E'_d \right)}{R_s{}^2 + X'^2} . \tag{C.14}$$

Also, by substituting (C.13) and (C.14) into (C.5) and (C.6), the expressions for the rotor currents are found in terms of meaningful variables as

$$i_{dr} = \frac{e'_q}{\omega_s L_m} - \frac{L_m}{L_r}\left[\frac{R_s \left(v_{ds} - e'_d \right) + X' \left(v_{qs} - e'_q \right)}{R_s{}^2 + X'^2} \right] \tag{C.15}$$

$$i_{qr} = -\frac{e'_d}{\omega_s L_m} - \frac{L_m}{L_r}\left[\frac{R_s\left(v_{qs} - e'_q\right) - X'\left(v_{ds} - e'_d\right)}{R_s{}^2 + X'^2}\right]. \tag{C.16}$$

Similarly, from the definitions of X', e'_d and e'_q, the equations (C.3) and (C.4) are rewritten as follows,

$$T'_0\frac{de'_d}{dt} = \omega_s L_m i_{qr} + \frac{\left(\omega_s - \omega_m\right)L_r}{R_r}e'_q - \frac{\omega_s L_m}{R_r}v_{qr} \tag{C.17}$$

$$T'_0\frac{de'_q}{dt} = -\omega_s L_m i_{dr} - \frac{\left(\omega_s - \omega_m\right)L_r}{R_r}e'_d + \frac{\omega_s L_m}{R_r}v_{dr}\ , \tag{C.18}$$

which are presented in (4.26) and (4.27), respectively, with $T'_0 = \frac{L_r}{\omega_b R_r}$.

In addition, having found the stator and rotor currents for the induction machine, expressing the stator and rotor powers as well as the electromagnetic torque, (4.19) to (4.22) and (4.25), respectively, in terms of meaningful variables is reasonably simple,

$$P_{gs} = \frac{R_s\left(v_{ds}{}^2 + v_{qs}{}^2 - v_{ds}e'_d - v_{qs}e'_q\right) + X'\left(e'_d v_{qs} - e'_q v_{ds}\right)}{R_s{}^2 + X'^2} \tag{C.19}$$

$$Q_{gs} = \frac{-R_s\left(e'_d v_{qs} - e'_q v_{ds}\right) + X'\left(v_{ds}{}^2 + v_{qs}{}^2 - v_{ds}e'_d - v_{qs}e'_q\right)}{R_s{}^2 + X'^2} \tag{C.20}$$

$$\begin{aligned} P_{gr} = -v_{qr}&\left\{\frac{e'_d}{\omega_s L_m} - \frac{L_m}{L_r}\left[\frac{R_s\left(e'_q - v_{qs}\right) - X'\left(e'_d - v_{ds}\right)}{\left(R_s{}^2 + X'^2\right)}\right]\right\} + \\ &v_{dr}\left\{\frac{e'_q}{\omega_s L_m} + \frac{L_m}{L_r}\left[\frac{R_s\left(e'_d - v_{ds}\right) + X'\left(e'_q - v_{qs}\right)}{\left(R_s{}^2 + X'^2\right)}\right]\right\} \end{aligned} \tag{C.21}$$

$$\begin{aligned} Q_{gr} = v_{dr}&\left\{\frac{e'_d}{\omega_s L_m} - \frac{L_m}{L_r}\left[\frac{R_s\left(e'_q - v_{qs}\right) - X'\left(e'_d - v_{ds}\right)}{\left(R_s{}^2 + X'^2\right)}\right]\right\} + \\ &v_{qr}\left\{\frac{e'_q}{\omega_s L_m} + \frac{L_m}{L_r}\left[\frac{R_s\left(e'_d - v_{ds}\right) + X'\left(e'_q - v_{qs}\right)}{\left(R_s{}^2 + X'^2\right)}\right]\right\} \end{aligned} \tag{C.22}$$

$$T_e = \frac{-R_s\left(e'_d{}^2 + e'_q{}^2 - v_{ds}e'_d - v_{qs}e'_q\right) + X'\left(e'_d v_{qs} - e'_q v_{ds}\right)}{\omega_s\left(R_s{}^2 + X'^2\right)}\ . \tag{C.23}$$

These last equations are presented in (4.29)-(4.33) by expressing the *dq*-stator voltages as function of variables of the network's reference frame: voltage magnitude V_k and angle θ_k [Krause et al., 2002]

$$v_{qs} = V_k \cos\left(\theta_k - \theta_e\right) \tag{C.24}$$

$$v_{ds} = -V_k \sin\left(\theta_k - \theta_e\right) , \tag{C.25}$$

where θ_e corresponds to the angular position of the synchronously rotating reference frame.

C.2 Nodal equations for the VSC model

In connection with Figure 4.5, the voltage and current relationships in the ideal tap-changing transformer are

$$\frac{\mathbf{V}_1}{\mathrm{V}_0} = \frac{m_a' \angle \phi}{1} \text{ and } \frac{m_a' \angle -\phi}{1} = \frac{\mathbf{I}_2}{\mathbf{I}_1} . \tag{C.19}$$

The current through the impedance connected between *k* and 1 is

$$\mathbf{I}'_1 = \mathbf{Y}_1\left(\mathbf{V}_k - \mathbf{V}_1\right) = \mathbf{Y}_1\mathbf{V}_k - m_a' \angle \phi \mathbf{Y}_1 \mathrm{V}_0 = \mathbf{I}_k \tag{C.20}$$

where $\mathbf{Y}_1 = 1/(R_{1v} + \mathrm{j}X_{1v})$. At node 0, the next relationship holds

$$\mathbf{I}_0 = -\mathbf{I}_2 + G_{sw}\,\mathrm{V}_0 = -m_a' \angle -\phi \mathbf{Y}_1 \mathbf{V}_k + m_a'^2 \mathbf{Y}_1\,\mathrm{V}_0 + jB_{eq} m_a'^2\,\mathrm{V}_0 + G_{sw}\,\mathrm{V}_0 \tag{C.21}$$

Rearranging equations (C.20) and (C.21) yields

$$\begin{pmatrix} \mathbf{I}_k \\ \mathbf{I}_0 \end{pmatrix} = \begin{pmatrix} \mathbf{Y}_1 & -m_a' \angle \phi \cdot \mathbf{Y}_1 \\ -m_a' \angle -\phi \cdot \mathbf{Y}_1 & m_a'^2\left(\mathbf{Y}_1 + \mathrm{j}B_{eq}\right) + G_{sw} \end{pmatrix} \begin{pmatrix} \mathbf{V}_k \\ \mathrm{V}_0 \end{pmatrix}. \tag{C.22}$$

Lastly, equation (C.22) is used to find the nodal power injections computed as (C.23), which is presented in an expanded form in (4.31)

$$\begin{pmatrix}\mathbf{S}_k\\ \mathbf{S}_0\end{pmatrix}=\begin{pmatrix}\mathbf{V}_k & 0\\ 0 & \mathbf{V}_0\end{pmatrix}\begin{pmatrix}\mathbf{I}_k\\ \mathbf{I}_0\end{pmatrix}^{*}. \tag{C.23}$$

C.3 Implicit trapezoidal method

As a first step, the implicit trapezoidal method calls for algebraizing the set of differential equations (4.2) by means of expressing the step-by-step solution of $\dot{y}$ as an integral form,

$$\dot{y}(t)-F(X(t),Y(t))=0 \tag{C.24}$$

$$\int_{t-\Delta t}^{t} dy-\int_{t-\Delta t}^{t} F(X(t),Y(t))dt=0 \tag{C.25}$$

$$Y(t)-Y(t-\Delta t)-\int_{t-\Delta t}^{t} F(X(t),Y(t))dt=0\,. \tag{C.26}$$

Assuming that all functions $F(\cdot)$ vary linearly over the time interval [t-Δt, t], the area under the integral can be approximated by a trapezoid; therefore (C.26) is expressed as

$$Y(t)-Y(t-\Delta t)-\frac{\Delta t}{2}[\underbrace{F(X(t-\Delta t),Y(t-\Delta t))}_{\dot{Y}_{t-\Delta t}}+\underbrace{F(X(t),Y(t))}_{\dot{Y}_t}]=0\,. \tag{C.27}$$

This last equation is used to discretize any function. The differential algebraic equation given in the form of a mismatch equation is then

$$F_Y=Y_{t-\Delta t}+\frac{\Delta t}{2}\dot{Y}_{t-\Delta t}-\left(Y_t-\frac{\Delta t}{2}\dot{Y}_t\right)=0 \tag{C.28}$$

Appendix D

Electric power system data

D.1 Conventional power flows

- FP-FSWG [Hwang et al., 2008]: Generator data: R_1 = 0.0027Ω, X_1 = 0.025Ω, R_2 = 0.0022Ω, X_2 = 0.046Ω, X_m = 1.38Ω, V = 690 V; wind turbine data: P_{nom} = 900 kW, R = 57 m,n_{gb} = 65.27; ρ = 1.225 kg/m^3, c_1 = 0.5, c_2 = 116, c_3 = 0.4, c_4 = 0.0, c_5 = 0, c_6 = 5, c_7 = 21, c_8 = 0.08, c_9 = 0.035, β = 0.

- PR-FSWG [Liu et al., 2008]: Generator data: R_1 = 0.0Ω, X_1 = 0.09985Ω, R_2 = 0.00373Ω, X_2 = 0.10906Ω, X_m = 3.54708Ω, V = 690 V; wind turbine data: P_{nom} = 600 kW. The wind generator power curve is shown in Table D.1.

Table D.1: Power curve for the PR-FSWG.

Wind speed (m/s)	Active power (kW)
5	37.5
7	116.4
9	269.4
11	450.0
13	570.3
15	625.4
17	635.0

- SSWG [Divya and Rao, 2006]: Generator data: R_1 = 0.00269Ω, X_1 = 0.072605Ω, R_2 = 0.002199Ω, X_2 = 0.04599Ω, X_m = 1.37997Ω, V = 690 V; wind turbine data: P_{nom} = 1000 kW. The wind generator power curve is shown in Figure D.1.

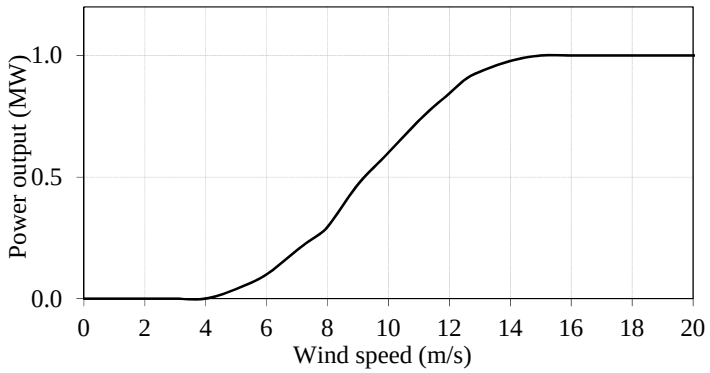

Figure D.1: SSWG power curve.

- DFIG: Generator data [Challoo and Nemmers, 2009]: R_1 = 0.0010236Ω, X_1 = 0.02073415Ω, R_2 = 0.0011426Ω, X_2 = 0.0192582Ω, X_m = 0.82341495Ω, V = 690 V; wind turbine data: P_{nom} = 2000 kW. The wind generator power curve [Li and Haskew, 2009] is shown in Figure D.2.

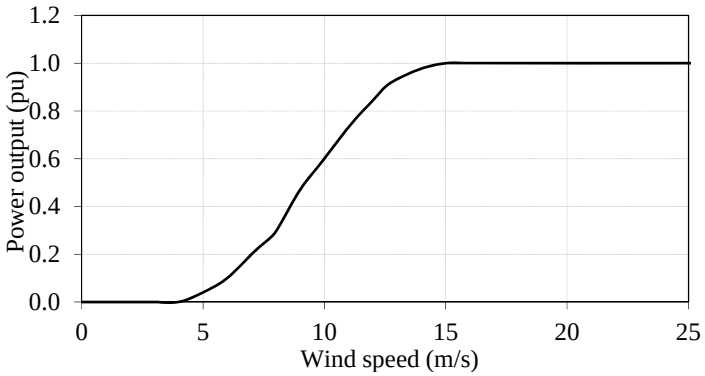

Figure D.2: DFIG power curve.

D.2 Power flows with automatic load-frequency devices

- FP-FSWG: Generator data [Akhmatov, 2003]: R_1 = 0.048 p.u, X_1 = 0.075 p.u, R_2 = 0.018, X_2 = 0.12 p.u, X_m =3.8 p.u, P_{nom} = 2 MW, V = 690 V, 50 Hz, 2 pole pairs. Fixed capacitor of 0.6 MVAr. Wind turbine data [Li and Haskew, 2009]: R = 35 m, n_{gb} = 80, ρ = 1.2041 kg/m^3; c_1 = 0.44, c_2 = 125, c_3 = 0.0, c_4 = 0.0, c_5 = 0.0, c_6 = 6.94, c_7 = 16.5, c_8 = 0.0, c_9 = -0.002, β = 0.

- PR-FSWG: Generator data: the same as the FP-FSWG. Fixed capacitor of 0.6 MVAr. Wind turbine data [Slootweg et al., 2003]: R = 37.5 m, n_{gb} = 89, ρ = 1.2041 kg/m^3, c_1 = 0.73, c_2 = 151, c_3 = 0.58, c_4 = 0.002, c_5 = 2.14, c_6 = 13.2, c_7 = 18.4, c_8 = -0.02, c_9 = -0.003, β = 0.

- Example 5.3.1 and 5.3.2: the coefficients for reactive power generation of the generator regulator are: a_Q = 1 and b_Q = 1; Q_{Gmax} = 0.5, Q_{Gmin} = -0.5.

- Example 5.3.3: additional parameters of the modified IEEE-14 bus test system on a base power of 100 MVA. Step-up transformer of wind farm I and II: Z = j0.06 p.u. Individual wind generator transformer for each FP-FSWG and DFIG: Z = j0.45 p.u. The governor droop characteristic of each DFIG is R = 0.05. The DFIG power curve is shown in Figure D.2. The coefficients for reactive power generation of the generator regulators are (see also Table D.2) a_Q = 1 and b_Q = 1. The loads connected at nodes 4, 9, 13 and 14 are constant. The loads connected at nodes 5, 10, 11 and 12 are dependent on frequency and voltage with the following parameters: K_p = 0.04, K_q = 0.0, p_p = 0.2, p_c = 0.3, p_z = 0.5, q_p = 0.2, q_c = 0.3 and q_z = 0.5.

Table D.2: Synchronous generators' characteristics and deloading of the DFIG-based wind farm

Bus	Voltage (p.u)	R (p.u)	$P_{G\ set}$ (p.u)		$Q_{G\ set}$ (p.u)	
			η =5%	η =10%	η = 5%	η = 10%
1	1.050	0.04	1.34819	1.38537	0.21743	0.21051
2	1.025	0.06	0.4	0.4	0.06280	0.06942
3	0.995	---	0.0	0.0	---	---
6	1.030	---	0.0	0.0	---	---
8	1.020	---	0.0	0.0	---	---

- Example 5.3.4: additional parameters of the modified IEEE-14 bus test system on a base power of 100 MVA. Step-up transformer impedance for each wind farm: Z = j0.06 p.u. The transformer impedance for each wind generator is Z = j0.45 p.u. The governor droop characteristic for each DFIG and PMSG is R = 0.05 p.u. The DFIG and PMSG power curve is shown in Figure D.2. The coefficients for reactive power generation of the generator regulators are (see also Table D.3) a_Q = 1 and b_Q = 1. The loads connected at nodes 5, 10, 11 and 12 are dependent on frequency and voltage

with the following parameters: K_p=0.04, K_q=0.0, p_p=0.2, p_c=0.3, p_z=0.5, q_p=0.2, q_c=0.3 and q_z=0.5, whereas the rest are constant.

Table D.3: Synchronous generators' characteristics and deloading of the VSWG-based wind farms

Bus	Voltage (p.u)	R (p.u)	$P_{G\ set}$ (p.u)		$Q_{G\ set}$ (p.u)	
			η =5%	η =10%	η = 5%	η = 10%
1	1.00	0.04	1.52208	1.55286	-0.35416	-0.35908
2	1.00	0.06	0.4	0.4	0.37690	0.38342
3	1.00	---	0.0	0.0	---	---
6	1.00	---	0.0	0.0	---	---
8	1.00	---	0.0	0.0	---	---

D.3 Time-domain simulations with DFIGs

The parameters for the DFIG and synchronous generators are:

- DFIG: wind turbine data: P_{nom} = 2.0 MW, H = 3.0 s, R = 37.5m, n_{gb} = 115, ρ = 1.225 kg/m^3, c_1 = 0.22, c_2 = 116, c_3 = 0.4, c_4 = 0.0, c_5 = 0, c_6 = 5, c_7 = 12.5, c_8 = 0.08, c_9 = 0.035, β = 0. Wound-rotor induction generator data: R_s = 0.0175 p.u, L_s = 0.2571 p.u, R_r = 0.0190 p.u, L_r = 0.2950 p.u, L_m = 6.921 p.u, n_{ps} = 4. Pitch-angle controller data: K_{pb} = 30, K_{ib} = 3, K_β = 5.0, T_β = 10. Back-to-back converter data: S_{nom} = 0.35*P_{nom}, H_c = 2.652 ms, V_0 = $\sqrt{2}$ p.u, G_{0r} = G_{0g} = 2e-3 p.u, R_{1r} = R_{1g} = 1e-4 p.u, X_{1r} = X_{1g} = 0.01 p.u. Rotor-side converter controller data: K_{pidr} = 0.5, K_{iidr} = 8.0, K_{pvdr} = 0.05, K_{ivdr} = 10.0, K_{pvqr} = 0.05, K_{ivqr} = 10.0. DC link controller: K_{pdc} = 0.008, K_{idc} = 1.0. Grid-side converter controller: K_{acg} = 2.5, T_{acg} = 0.05, K_{acm} = 5, T_{acm} = 1, K_{qm} = 0.005, K_{vm} = 2.

- Example 5.4.1:

Table D.4: 8-bus network's synchronous generators data

Bus	X_d (p.u)	X_q (p.u)	X'_d (p.u)	X'_q (p.u)	T'_{d0} (s)	T'_{q0} (s)	H (s)	D (p.u)
1	0.1460	0.0969	0.0608	0.0969	8.960	0.310	23.64	0.01
3	0.8958	0.8645	0.1198	0.1969	6.00	0.535	6.40	0.01

Table D.5: 8-bus network's automatic voltage regulator data

Bus	T_A	K_A	T_F	K_F	T_E
1	0.20	20.0	0.35	0.063	0.314
3	0.20	20.0	0.35	0.063	0.314

Table D.6: 8-bus network's hydroturbine-governor data

Bus	T_W	T_C	K
1	0.50	0.30	0.06
3	0.50	0.30	0.06

The parameters for all the loads are: $K_p = K_q = 0$; $p_p = 0.4$; $p_c = 0.3$; $p_z = 0.3$; $q_p = 0.4$; $q_c = 0.3$; $q_z = 0.3$.

- Example 5.4.2:

Table D.7: IEEE 30-bus network's synchronous generators data

Bus	X_d (p.u)	X_q (p.u)	X'_d (p.u)	X'_q (p.u)	T'_{d0} (s)	T'_{q0} (s)	H (s)	D (p.u)
1	0.1460	0.0969	0.0608	0.0969	8.960	0.310	23.64	0.01
2	0.8958	0.8645	0.1198	0.1969	6.00	0.535	6.400	0.01
5	1.3125	1.2578	0.1813	0.2500	5.890	0.600	3.010	0.01
8	1.3125	1.2578	0.1813	0.2500	5.890	0.600	3.010	0.01
11	1.3125	1.2578	0.1813	0.2500	5.890	0.600	3.010	0.01
13	1.3125	1.2578	0.1813	0.2500	5.890	0.600	3.010	0.01

Table D.8: IEEE 30-bus network's automatic voltage regulator data

Bus	T_A	K_A	T_F	K_F	T_E
1	0.20	20.0	0.35	0.063	0.314
2	0.20	20.0	0.35	0.063	0.314
5	0.20	20.0	0.35	0.063	0.314
8	0.20	20.0	0.35	0.063	0.314
11	0.20	20.0	0.35	0.063	0.314
13	0.20	20.0	0.35	0.063	0.314

Table D.9: IEEE 30-bus network's hydroturbine-governor data

Bus	T_W	T_C	K
1	0.50	0.30	0.06
2	0.50	0.30	0.06
5	0.50	0.30	0.06
8	0.50	0.30	0.06
11	0.50	0.30	0.06
13	0.50	0.30	0.06

The parameters for all the loads are: $K_p = K_q = 0$; $p_p = 0.4$; $p_c = 0.3$; $p_z = 0.3$; $q_p = 0.4$; $q_c = 0.3$; $q_z = 0.3$.

D.4 8-bus system data

Table D.10: 8-bus network's transmission line parameters

Buses		R (p.u)	X (p.u)	$B/2$ (p.u)
2	4	0.005	0.050	0.15
2	5	0.005	0.050	0.15
4	5	0.005	0.050	0.15
6	7	0.025	0.023	0.000

Table D.11: 8-bus network's transformer parameters

Buses		R (p.u)	X (p.u)	*Tap*
1	2	0.00	0.04	1.0
3	4	0.00	0.04	1.0
5	6	0.00	0.06	1.0
7	8	0.00	0.25	1.0

Table D.12: 8-bus network's generator parameters

Bus	P_g (p.u)	V_{sp} (p.u)
1	Slack	1.0
2	1.0	1.0

Table D.13: 8-bus network's load parameters

Bus	P_d (p.u)	Q_d (p.u)
4	1.20	0.40
5	0.90	0.35

D.5 14-bus system data

Table D.14: IEEE 14-bus network's transmission line parameters

Buses		R (p.u)	X (p.u)	$B/2$ (p.u)	Buses		R (p.u)	X (p.u)	$B/2$ (p.u)
1	2	0.01938	0.05917	0.0264	6	12	0.12291	0.25581	0.0000
1	5	0.05403	0.22304	0.0246	6	13	0.06615	0.13027	0.0000
2	3	0.04699	0.19797	0.0219	9	10	0.03181	0.0845	0.0000
2	4	0.05811	0.17632	0.0187	9	14	0.12711	0.27038	0.0000
2	5	0.05695	0.17388	0.0170	10	11	0.08205	0.19207	0.0000
3	4	0.06701	0.17103	0.0173	12	13	0.22092	0.19988	0.0000
4	5	0.01335	0.04211	0.0064	13	14	0.17093	0.34802	0.0000
6	11	0.09498	0.1989	0.0000					

Table D.15: IEEE 14-bus network's transformer parameters

Buses		R (p.u)	X (p.u)	*Tap*
4	7	0.00	0.20912	0.978
4	9	0.00	0.55618	0.969
5	6	0.00	0.25202	0.932
7	8	0.00	0.17615	1.00
7	9	0.00	0.11001	1.00

Table D.16: IEEE 14-bus network's generator parameters

Bus	P_g (p.u)	V_{sp} (p.u)
1	Slack	1.050
2	0.40	1.025
3	0.00	0.995
6	0.00	1.030
8	0.00	1.020

Table D.17: IEEE 14-bus network's load parameters

Bus	P_d (p.u)	Q_d (p.u)
2	0.217	0.127
3	0.942	0.19
4	0.478	-0.039
5	0.076	0.016
6	0.112	0.075
9	0.295	0.166
10	0.09	0.058
11	0.035	0.018
12	0.061	0.016
13	0.135	0.058
14	0.149	0.05

D.6 30-bus system data

Table D.18: IEEE 30-bus network's transmission line parameters

Buses		R (p.u)	X (p.u)	B/2 (p.u)	Bus		R (p.u)	X (p.u)	B/2 (p.u)
1	2	0.0192	0.0575	0.0264	15	18	0.1073	0.2185	0.000
1	3	0.0452	0.1852	0.0204	18	19	0.0639	0.1292	0.000
2	4	0.0570	0.1737	0.0184	19	20	0.0340	0.0680	0.000
3	4	0.0132	0.0379	0.0042	10	20	0.0936	0.2090	0.000
2	5	0.0472	0.1983	0.0209	10	17	0.0324	0.0845	0.000
2	6	0.0581	0.1763	0.0187	10	21	0.0348	0.0749	0.000
4	6	0.0119	0.0414	0.0045	10	22	0.0727	0.1499	0.000
5	7	0.0460	0.1160	0.0102	21	22	0.0116	0.0236	0.000
6	7	0.0267	0.0820	0.0085	15	23	0.1000	0.2020	0.000
6	8	0.0120	0.0420	0.000	22	24	0.1150	0.1790	0.000
8	28	0.0636	0.2000	0.0214	23	24	0.1320	0.2700	0.000
6	28	0.0169	0.0599	0.0065	24	25	0.1885	0.3292	0.000
12	14	0.1231	0.2559	0.000	25	26	0.2544	0.3800	0.000
12	15	0.0662	0.1304	0.000	25	27	0.1093	0.2087	0.000
12	16	0.0945	0.1987	0.000	27	29	0.2198	0.4153	0.000
14	16	0.2210	0.1997	0.000	27	30	0.3202	0.6027	0.000
16	17	0.0824	0.1923	0.000	29	30	0.2399	0.4533	0.000

Table D.19: IEEE 30-bus network's transformer parameters

Buses		R (p.u)	X (p.u)	*Tap*
6	9	0.00	0.208	0.978
6	10	0.00	0.556	0.969
4	12	0.00	0.256	0.932
9	11	0.00	0.208	1
9	10	0.00	0.11	1
12	13	0.00	0.14	1
27	28	0.00	0.396	0.968

Table D.20: IEEE 30-bus network's generator parameters

Bus	P_g (p.u)	V_{sp} (p.u)
1	Slack	1.060
2	0.40	1.045
5	0.00	1.010
8	0.00	1.010
11	0.00	1.082
13	0.00	1.071

Table D.21: IEEE 30-bus network's load parameters

Bus	P_d (p.u)	Q_d (p.u)	Bus	P_d (p.u)	Q_d (p.u)
2	0.217	0.127	17	0.090	0.058
3	0.024	0.012	18	0.032	0.009
4	0.076	0.016	19	0.095	0.034
5	0.942	0.190	20	0.022	0.007
7	0.228	0.109	21	0.175	0.112
8	0.300	0.300	23	0.032	0.016
10	0.058	0.020	24	0.087	0.067
12	0.112	0.075	26	0.035	0.023
14	0.062	0.016	29	0.024	0.009
15	0.082	0.025	30	0.106	0.019
16	0.035	0.018			

D.7 118-bus system data

Table D.22: IEEE 118-bus network's transmission line parameters

Buses		*R* (p.u)	*X* (p.u)	*B*/2 (p.u)	Buses		*R* (p.u)	*X* (p.u)	*B*/2 (p.u)
1	2	0.03030	0.09990	0.01270	38	65	0.00901	0.09860	0.52300
1	3	0.01290	0.04240	0.00541	64	65	0.00269	0.03020	0.19000
4	5	0.00176	0.00798	0.00105	49	66	0.01800	0.09190	0.01240
3	5	0.02410	0.10800	0.01420	49	66	0.01800	0.09190	0.01240
5	6	0.01190	0.05400	0.00713	62	66	0.04820	0.21800	0.02890
6	7	0.00459	0.02080	0.00275	62	67	0.02580	0.11700	0.01550
8	9	0.00244	0.03050	0.58100	66	67	0.02240	0.10150	0.01341
9	10	0.00258	0.03220	0.61500	65	68	0.00138	0.01600	0.31900
4	11	0.02090	0.06880	0.00874	47	69	0.08440	0.27780	0.03546
5	11	0.02030	0.06820	0.00869	49	69	0.09850	0.32400	0.04140
11	12	0.00595	0.01960	0.00251	69	70	0.03000	0.12700	0.06100
2	12	0.01870	0.06160	0.00786	24	70	0.00221	0.41150	0.05099
3	12	0.04840	0.16000	0.02030	70	71	0.00882	0.03550	0.00439
7	12	0.00862	0.03400	0.00437	24	72	0.04880	0.19600	0.02440
11	13	0.02225	0.07310	0.00938	71	72	0.04460	0.18000	0.02222
12	14	0.02150	0.07070	0.00908	71	73	0.00866	0.04540	0.00589
13	15	0.07440	0.24440	0.03134	70	74	0.04010	0.13230	0.01684
14	15	0.05950	0.19500	0.02510	70	75	0.04280	0.14100	0.01800
12	16	0.02120	0.08340	0.01070	69	75	0.04050	0.12200	0.06200
15	17	0.01320	0.04370	0.02220	74	75	0.01230	0.04060	0.00517
16	17	0.04540	0.18010	0.02330	76	77	0.04440	0.14800	0.01840
17	18	0.01230	0.05050	0.00649	69	77	0.03090	0.10100	0.05190
18	19	0.01119	0.04930	0.00571	75	77	0.06010	0.19990	0.02489
19	20	0.02520	0.11700	0.01490	77	78	0.00376	0.01240	0.00632
15	19	0.01200	0.03940	0.00505	78	79	0.00546	0.02440	0.00324
20	21	0.01830	0.08490	0.01080	77	80	0.01700	0.04850	0.02360
21	22	0.02090	0.09700	0.01230	77	80	0.02940	0.10500	0.01140
22	23	0.03420	0.15900	0.02020	79	80	0.01560	0.07040	0.00935
23	24	0.01350	0.04920	0.02490	68	81	0.00175	0.02020	0.40400
23	25	0.01560	0.08000	0.04320	77	82	0.02980	0.08530	0.04087
25	27	0.03180	0.16300	0.08820	82	83	0.01120	0.03665	0.01898
27	28	0.01913	0.08550	0.01080	83	84	0.06250	0.13200	0.01290
28	29	0.02370	0.09430	0.01190	83	85	0.04300	0.14800	0.01740
8	30	0.00431	0.05040	0.25700	84	85	0.03020	0.06410	0.00617
26	30	0.00799	0.08600	0.45400	85	86	0.03500	0.12300	0.01380
17	31	0.04740	0.15630	0.01995	86	87	0.02828	0.20740	0.02225
29	31	0.01080	0.03310	0.00415	85	88	0.02000	0.10200	0.01380
23	32	0.03170	0.11530	0.05865	85	89	0.02390	0.17300	0.02350

Table D.23: IEEE 118-bus network's transmission line parameters (cont.)

Buses		*R* (p.u)	*X* (p.u)	*B*/2 (p.u)	Buses		*R* (p.u)	*X* (p.u)	*B*/2 (p.u)
31	32	0.02980	0.09850	0.01255	88	89	0.01390	0.07120	0.00967
27	32	0.02290	0.07550	0.00963	89	90	0.05180	0.18800	0.02640
15	33	0.03800	0.12440	0.01597	89	90	0.02380	0.09970	0.05300
19	34	0.07520	0.24700	0.03160	90	91	0.02540	0.08360	0.01070
35	36	0.00224	0.01020	0.00134	89	92	0.00990	0.05050	0.02740
35	37	0.01100	0.04970	0.00659	89	92	0.03930	0.15810	0.02070
33	37	0.04150	0.14200	0.01830	91	92	0.03870	0.12720	0.01634
34	36	0.00871	0.02680	0.00284	92	93	0.02580	0.08480	0.01090
34	37	0.00256	0.00940	0.00492	92	94	0.04810	0.15800	0.02030
37	39	0.03210	0.10600	0.01350	93	94	0.02230	0.07320	0.00938
37	40	0.05930	0.16800	0.02100	94	95	0.01320	0.04340	0.00555
30	38	0.00464	0.05400	0.21100	80	96	0.03560	0.18200	0.02470
39	40	0.01840	0.06050	0.00776	82	96	0.01620	0.05300	0.02720
40	41	0.01450	0.04870	0.00611	94	96	0.02690	0.08690	0.01150
40	42	0.05550	0.18300	0.02330	80	97	0.01830	0.09340	0.01270
41	42	0.04100	0.13500	0.01720	80	98	0.02380	0.10800	0.01430
43	44	0.06080	0.24540	0.03034	80	99	0.04540	0.20600	0.02730
34	43	0.04130	0.16810	0.02113	92	100	0.06480	0.29500	0.02360
44	45	0.02240	0.09010	0.01120	94	100	0.01780	0.05800	0.03020
45	46	0.04000	0.13560	0.01660	95	96	0.01710	0.05470	0.00737
46	47	0.03800	0.12700	0.01580	96	97	0.01730	0.08850	0.01200
46	48	0.06010	0.18900	0.02360	98	100	0.03970	0.17900	0.02380
47	49	0.01910	0.06250	0.00802	99	100	0.01800	0.08130	0.01080
42	49	0.07150	0.32300	0.04300	100	101	0.02770	0.12620	0.01640
42	49	0.07150	0.32300	0.04300	92	102	0.01230	0.05590	0.00732
45	49	0.06840	0.18600	0.02220	101	102	0.02460	0.11200	0.01470
48	49	0.01790	0.05050	0.00629	100	103	0.01600	0.05250	0.02680
49	50	0.02670	0.07520	0.00937	100	104	0.04510	0.20400	0.02705
49	51	0.04860	0.13700	0.01710	103	104	0.04660	0.15840	0.02035
51	52	0.02030	0.05880	0.00698	103	105	0.05350	0.16250	0.02040
52	53	0.04050	0.16350	0.02029	100	106	0.06050	0.22900	0.03100
53	54	0.02630	0.12200	0.01550	104	105	0.00994	0.03780	0.00493
49	54	0.07300	0.28900	0.03690	105	106	0.01400	0.05470	0.00717
49	54	0.08690	0.29100	0.03650	105	107	0.05300	0.18300	0.02360
54	55	0.01690	0.07070	0.01010	105	108	0.02610	0.07030	0.00922
54	56	0.00275	0.00955	0.00366	106	107	0.05300	0.18300	0.02360
55	56	0.00488	0.01510	0.00187	108	109	0.01050	0.02880	0.00380
56	57	0.03430	0.09660	0.01210	103	110	0.03906	0.18130	0.02305
50	57	0.04740	0.13400	0.01660	109	110	0.02780	0.07620	0.01010
56	58	0.03430	0.09660	0.01210	110	111	0.02200	0.07550	0.01000
51	58	0.02550	0.07190	0.00894	110	112	0.02470	0.06400	0.03100

Table D.24: IEEE 118-bus network's transmission line parameters (cont.)

Buses		R (p.u)	X (p.u)	$B/2$ (p.u)	Buses		R (p.u)	X (p.u)	$B/2$ (p.u)
54	59	0.05030	0.22930	0.02990	17	113	0.00913	0.03010	0.00384
56	59	0.08250	0.25100	0.02845	32	113	0.06150	0.20300	0.02590
56	59	0.08030	0.23900	0.02680	32	114	0.01350	0.06120	0.00814
55	59	0.04739	0.21580	0.02823	27	115	0.01640	0.07410	0.00986
59	60	0.03170	0.14500	0.01880	114	115	0.00230	0.01040	0.00138
59	61	0.03280	0.15000	0.01940	68	116	0.00034	0.00405	0.08200
60	61	0.00264	0.01350	0.00728	12	117	0.03290	0.14000	0.01790
60	62	0.01230	0.05610	0.00734	75	118	0.01450	0.04810	0.00599
61	62	0.00824	0.03760	0.00490	76	118	0.01640	0.05440	0.00678
63	64	0.00172	0.02000	0.10800					

Table D.25: IEEE 118-bus network's transformer parameters

Buses		R (p.u)	X (p.u)	*Tap*	Buses		R (p.u)	X (p.u)	*Tap*
8	5	0.00	0.0267	0.985	64	61	0.00	0.0268	0.985
26	25	0.00	0.0382	0.96	65	66	0.00	0.037	0.935
30	17	0.00	0.0388	0.96	68	69	0.00	0.037	0.935
38	37	0.00	0.0375	0.935	81	80	0.00	0.037	0.935
63	59	0.00	0.0386	0.96					

Table D.26: IEEE 118-bus network's generator parameters

Bus	P_g (p.u)	V_{sp} (p.u)	Bus	P_g (p.u)	V_{sp} (p.u)	Bus	P_g (p.u)	V_{sp} (p.u)
1	0.000	0.955	42	-0.590	0.985	80	4.770	1.040
4	-0.090	0.998	46	0.190	1.005	85	0.000	0.985
6	0.000	0.990	49	2.040	1.025	87	0.040	1.015
8	-0.280	1.015	54	0.480	0.955	89	6.070	1.005
10	4.500	1.050	55	0.000	0.952	90	-0.850	0.985
12	0.850	0.990	56	0.000	0.954	91	-0.100	0.980
15	0.000	0.970	59	1.550	0.985	92	0.000	0.990
18	0.000	0.973	61	1.600	0.995	99	-0.420	1.010
19	0.000	0.962	62	0.000	0.998	100	2.520	1.017
24	-0.130	0.992	65	3.910	1.005	103	0.400	1.010
25	2.200	1.050	66	3.920	1.050	104	0.000	0.971
26	3.140	1.015	69	Slack	1.035	105	0.000	0.965
27	-0.090	0.968	70	0.000	0.984	107	-0.220	0.952
31	0.070	0.967	72	-0.120	0.980	110	0.000	0.973
32	0.000	0.963	73	-0.060	0.991	111	0.360	0.980
34	0.000	0.984	74	0.000	0.958	112	-0.430	0.975
36	0.000	0.980	76	0.000	0.943	113	-0.060	0.993
40	-0.460	0.970	77	0.000	1.006	116	-1.840	1.005

Table D.27: IEEE 118-bus network's load parameters

Bus	P_d (p.u)	Q_d (p.u)	Bus	P_d (p.u)	Q_d (p.u)	Bus	P_d (p.u)	Q_d (p.u)
1	0.51	0.27	42	0.37	0.23	82	0.54	0.27
2	0.20	0.09	43	0.18	0.07	83	0.20	0.10
3	0.39	0.10	44	0.16	0.08	84	0.11	0.07
4	0.30	0.12	45	0.53	0.22	85	0.24	0.15
6	0.52	0.22	46	0.28	0.10	86	0.21	0.10
7	0.19	0.02	47	0.34	0.00	88	0.48	0.10
11	0.70	0.23	48	0.20	0.11	90	0.78	0.42
12	0.47	0.10	49	0.87	0.30	92	0.65	0.10
13	0.34	0.16	50	0.17	0.04	93	0.12	0.07
14	0.14	0.01	51	0.17	0.08	94	0.30	0.16
15	0.90	0.30	52	0.18	0.05	95	0.42	0.31
16	0.25	0.10	53	0.23	0.11	96	0.38	0.15
17	0.11	0.03	54	1.13	0.32	97	0.15	0.09
18	0.60	0.34	55	0.63	0.22	98	0.34	0.08
19	0.45	0.25	56	0.84	0.18	100	0.37	0.18
20	0.18	0.03	57	0.12	0.03	101	0.22	0.15
21	0.14	0.08	58	0.12	0.03	102	0.05	0.03
22	0.10	0.05	59	2.77	1.13	103	0.23	0.16
23	0.07	0.03	60	0.78	0.03	104	0.38	0.25
27	0.62	0.13	62	0.77	0.14	105	0.31	0.26
28	0.17	0.07	66	0.39	0.18	106	0.43	0.16
29	0.24	0.04	67	0.28	0.07	107	0.28	0.12
31	0.43	0.27	70	0.66	0.20	108	0.02	0.01
32	0.59	0.23	74	0.68	0.27	109	0.08	0.03
33	0.23	0.09	75	0.47	0.11	110	0.39	0.30
34	0.59	0.26	76	0.68	0.36	112	0.25	0.13
35	0.33	0.09	77	0.61	0.28	114	0.08	0.03
36	0.31	0.17	78	0.71	0.26	115	0.22	0.07
39	0.27	0.11	79	0.39	0.32	117	0.20	0.08
40	0.20	0.23	80	1.30	0.26	118	0.33	0.15
41	0.37	0.10						